UNIVERSITÀ DEGLI STUDI DI MILANO

Scuola di Dottorato in Fisica, Astrofisica e Fisica Applicata

Dipartimento di Fisica

Corso di Dottorato in Fisica, Astrofisica e Fisica Applicata

Ciclo XXIII

Deep Nuclear Resonant Tunneling Thermal Rate Constant Calculations

Settore Scientifico Disciplinare FIS/02

Supervisore: Professor Sergio Caracciolo

Co-Supervisore: Professor Michele Ceotto

Coordinatore: Professor Marco BERSANELLI

Tesi di Dottorato di:

Salvatore Mandrà

Anno Accademico 2012/2013

Commission of the final examination:

External Referee:
M. Persico, *Prof.* (Dep. of Chemistry and Industrial Chemistry, Università di Pisa, Italy)

External Member:
J. Vanicek, *Prof.* (Lab. of Th. Phys. Chemistry, EPFL, Switzerland)

Internal Member:
M. Ceotto, *Ass. Prof.* (Dep. of Chemistry, Università degli Studi di Milano, Italy)

Final examination:

Date: 19/03/2013

Università degli Studi di Milano, Dipartimento di Fisica, Milano, Italy

Una ricerca comincia sempre con la "Fortuna del Principiante".
E finisce sempre con la "Prova del Conquistatore".
*(*L'Alchimista*, P. Coelho)*

PACS:

73.40.Gk (Resonant Tunneling)

03.65.Xp (Quantum Mechanics of Tunneling)

31.15.A- (Ab Initio Calculations)

85.30.Mn (Resonance Tunneling Devices)

28.60.+s (Isotope Separation and Enrichment)

32.10.Bi (Isotopes)

31.30.Gs (Isotope Effects for Atoms and Molecules)

03.67.Lx (Quantum Computation)

Keywords: Resonant Tunneling, Thermal Rate Constant, Resonant Rate Constant, Transmission Probability, Isotope Effects, Isotope Separation and Enrichment, Quantum Computation.

Contents

Introduction

Motivation

The thermal rate constant $k(T)$ is an essential observable for the quantitative description of chemical dynamics and its study offers a common playground of comparison between innovative experimental techniques, new theories and computational tools. Since the formulation of the transition state theory [1–4], many efforts have been devoted to the development of an exact and computationally feasible approach to the thermal rate constant calculation. In this thesis, we focus on the calculation of $k(T)$ for double barrier passages in the presence of several quasi-bound (resonant) states. The importance of studying $k(T)$ in the presence of quasi-bound states is related to the occurrence of resonant tunneling, which considerably increases the transmission probability at the resonance energy. Specifically, resonant tunneling occurs when an incident wave-packet has an energy which is comparable to one of the quasi-bound state energies: in this case, the tunneling probability is greatly enhanced and the wave-packet can cross the potential without an effective reduction of its amplitude. Pioneering experimental observations of resonant tunneling lead to what is presently known as Ramsauer's effect (or negative resistance). In particular, such effect manifested itself in the form of electrons crossing double-barrier structures having a thin GaAs film sandwiched between two GaAlAs barriers [5,6]. The resonance was observed from peaks in the tunneling current, when the voltage was set near the quasi-stationary energy states of the potential well. Beyond semiconductors [7,8], resonant tunneling is relevant to describe several experimental systems such as quantum dots [9], the Fabry-Perot interferometer [10] and molecular reactions [11–14]. Another example of molecular resonant scattering is the reaction $H + O_2$ [13,14], where the resonances are induced by the presence of an intermediate well. In this case, full dimensional accurate quantum results are available [15,16].

Although many analytical results can be obtained for single barrier potentials (e.g. the rectangular barrier or Eckart barrier [17]), little is known about resonant tunneling for potentials with two or more barriers beyond the simple case of double rectangular potentials [18–21]. This is due to the intensive numerical effort required to compute $k\left(T\right)$ exactly, even in the one dimensional case. Moreover, these calculations are much more challenging than evaluating the transmission probability for systems where resonances are induced by the presence of an intermediate well [16] (with fixed total angular momentum) or for single barrier potentials in the presence of wells. [22]

Calculations of $k\left(T\right)$ can be done using either a time-dependent or time-independent method. In the time-dependent approach, a non-negligible amount of computational time is required when long-lived resonance states are present. Further, a large spatial width wave-packet is needed in order to observe resonances which are costly to obtain in terms of grid methods. The corresponding momentum is well-defined and it has a small energy spread. From this point of view, double barrier potentials can also be used as an energy filter to get those wave-packet components whose momenta distribution width is comparable with the resonance width. Inspired by this consideration, Moyesev and co-workers have developed a non-Hermitian representation of quasi-bound states decay and solved the time-dependent Schrödinger equation with outgoing boundary conditions [23–27]. They were able to calculate the tunneling transmission probability for two Gaussian barriers supporting up to five resonances.

Major advances in the time-dependent picture have been obtained by Miller and coworkers [28, 29], who developed a method in which a time integration of the flux auto-correlation function is used to compute $k(T)$ directly. Although this method has been widely used [29], it is practically limited to potentials with one single barrier or two very close and narrow barriers [30]. Indeed, when many quasi-bound states are present, the numerical effort required to compute the long-time dynamics for the thermal rate constant increases greatly. In this direction, Peskin et al. [31–34] developed a more stable variant of the flux auto-correlation method to compute $k(T)$ even in the presence of resonances, the so called Flux Averaging method (FAM). Although this last method partially solves the issue of the long-time dynamics imposed by the flux auto-correlation approach, the computational time required to reach convergence still dramatically increases in the deep resonant regime.

Main results

To overcome these limitations, in this thesis we present a novel time-independent approach to compute $k(T)$ for any arbitrary multi-barrier potential (even for first-derivative

discontinuous potentials), in the presence of many quasi-bound states. The method consists in a fast and robust procedure for calculating $k(T)$ as the thermal average of the transmission probability $T(E)$, namely the probability of a quantum particle to cross the scattering potential, by directly solving the Schrödinger equation as an ordinary differential equation (ODE) with the energy as a parameter. This, avoids having to solve the related eigenvalue problem. We stress that even though the thermal rate constant has been computed for potentials with few resonant peaks [30, 32], to the best of our knowledge $k(T)$ has not been evaluated in the presence of two clearly separated barriers with several quasi-bound states. In the following, we resume the most important results we obtained:

- The first part of this thesis is dedicated to the calculation of the thermal rate constant at very low temperatures for arbitrary potentials. In particular, we focused our attention on double barrier potentials where the effects of the resonant tunneling are not negligible. Part of these results has been recently published on International Journal of Quantum Chemistry [35].

- Using the potential profile of a nanoporous graphene double-layer obtained by an *ab initio* calculation, we show how resonant tunneling can be used to select species with different masses. In particular, we considered the selection of Helium isotopes. Part of the results discussed in this thesis will be published in collaboration with A. M. Brockway (Dep. of Chemistry, Haverford College, Haverford (PA), USA) and J. Schrier (Dep. of Chemistry, Haverford College, Haverford (PA), USA) [36]. This is an example of quantum mechanical sieve for isotope enrichment.

- Resonant tunneling plays a fundamental role in the "Inverse Kinetic Isotope Effect", i.e. the effect for which heaviest isotopes have a larger thermal rate constant respect to lightest isotopes. For shedding light on this direction, we extensively studied the thermal rate constant by varying the distance Δ between two potential barriers. A paper including these results is in preparation [37].

- The last part of this thesis has been dedicated to outline a quantum protocol for the calculation of the thermal rate constant on a quantum computer. In particular, we take advantage of our time-independent ODE method for devising a quantum algorithm with an exponential speed-up with respect to any equivalent classical algorithm.

Organization

This thesis is organized as follows: in the first Chapter, we introduced the concept of "Thermal Rate Constant", including the state-of-art of the theory. The second Chapter

is dedicated to the comparison between the two main method for the computation of the thermal rate constant: the "Time-Dependent" approach and the "Time-Independent" approach. In particular, in Chap. 3 we will show how the time-dependent approach fails in extreme resonant conditions. Chap. 4 presents the principal methods for the numerical integration of Schrödinger equations that will be used in the time-independent approach. In Chap. 5, 6, and 7 we will present the main results of this thesis. Finally, in Future Perspectives, we will outline a quantum ODE algorithm for the computation of the thermal rate constant on quantum computers.

CHAPTER 1

Thermal Rate Constants

The thermal rate constant, or "speed of reaction" either for a reactant or a product during a given reaction, can intuitively be considered as a measure of how fast or slow a reaction takes place. For example, the oxidative rusting of iron under the atmosphere is a slow reaction that can take place within many years, while the combustion of cellulose is a reaction which occurs in fractions of a second. The first part of this Chapter will be dedicated to the derivation of the classical expression of the thermal rate constant. In the second part, we will introduce the Transition State Theory (TST), as an approximation of the classical the thermal rate constant expression. Finally, we will introduce the general quantum theory for thermal rate constant calculations.

1.1 Classical Thermal Rate Constants

1.1.1 Collinear reaction

Consider a collinear reaction of the form $A + BC \mapsto AB + C$, where the molecule B is transferred from the molecule C to the molecule A. Starting from here, we will call "reactants" and "products" respectively all the molecules on the l.h.s. and r.h.s. of the collinear reaction. For a given initial condition $(\mathbf{p}_0,\, \mathbf{q}_0)$ of the system, where $\mathbf{p}_0$ and $\mathbf{q}_0$ are respectively the generalized moments and coordinates of the reaction space, the transition rate for that initial phase space configuration $k\left(\mathbf{p}_0,\, \mathbf{q}_0\right)$ can be expressed as

$$k\left(\mathbf{p}_0,\, \mathbf{q}_0\right) = \Phi\left(\mathbf{p}_0,\, \mathbf{q}_0; f\left(\mathbf{q}\right)\right) P_{react}\left(\mathbf{p}_0,\, \mathbf{q}_0\right) \tag{1.1.1}$$

where $\Phi\left(\mathbf{p}_0,\, \mathbf{q}_0\right)$ is the reaction flux across a surface $f\left(\mathbf{q}\right) = 0$ dividing reactants from products, i.e. the amount of reactants turning into products by crossing the surface $f\left(\mathbf{q}\right) = 0$ per unit of time. $P_{react}\left(\mathbf{p}_0,\, \mathbf{q}_0\right)$ is the reaction probability, i.e. the probability that the collinear reaction actually takes place. In other words, $P_{react}\left(\mathbf{p}_0,\, \mathbf{q}_0\right)$ will count

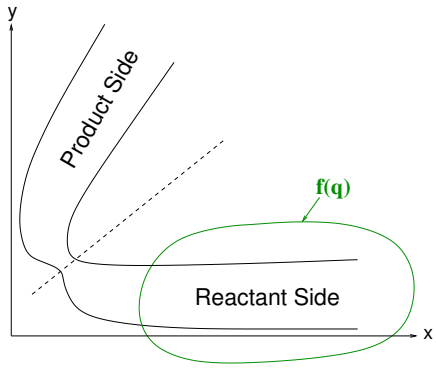

Figure 1.1.1: Example of a closed surface $f(\mathbf{q})$ around reactant space for collinear reaction.

the reactants that cross the dividing surface and are indefinitely turned into products. Hence, the classical thermal rate constant can be expressed as the phase space average

$$\begin{aligned} k(T) &= \langle k(\mathbf{p}_0, \mathbf{q}_0)\rangle_T \\ &= \frac{1}{\mathcal{Q}_{react}(T)} \int \frac{d\mathbf{p}_0\, d\mathbf{q}_0}{(2\pi\hbar)^F} e^{-\beta\mathcal{H}(\mathbf{p}_0,\,\mathbf{q}_0)} \Phi(\mathbf{p}_0,\,\mathbf{q}_0)\, P_{react}(\mathbf{p}_0,\,\mathbf{q}_0), \end{aligned} \tag{1.1.2}$$

where F is the number of degrees of freedom and $\beta = \frac{1}{k_B T}$ is the inverse temperature. In Eq. (1.1.2), the average is over the usual Boltzmann-Maxwell distribution with the classical Hamiltonian $\mathcal{H}(\mathbf{p}_0,\,\mathbf{q}_0) = K(\mathbf{p}_0) + V(\mathbf{q}_0)$, where $K(\mathbf{p}_0)$ is the kinetic energy and $V(\mathbf{q}_0)$ is the surface reaction potential, and $\mathcal{Q}_{react}(T) = \int \frac{d\mathbf{p}_0\, d\mathbf{q}_0}{(2\pi\hbar)^F} e^{-\beta\mathcal{H}(\mathbf{p}_0,\,\mathbf{q}_0)}$ is the partition function. Considering that the collinear reaction $A + BC \mapsto AB + C$ takes place when the system crosses the dividing surface $f(\mathbf{q}) = 0$, which divides reactants ($f(\mathbf{q}) < 0$) from products ($f(\mathbf{q}) > 0$) (see Fig. (1.1.1)), the reaction flux can be easily expressed as

$$\Phi(\mathbf{p}_0,\,\mathbf{q}_0) = \frac{d\theta(f(\mathbf{q}_0))}{dt} = \delta(f(\mathbf{q}_0))\, \vec{\nabla}_{\mathbf{q}} f(\mathbf{q}) \cdot \frac{\mathbf{p}_0}{\mu}, \tag{1.1.3}$$

where $\mu = \frac{m_A(m_B+m_C)}{m_A+m_B+m_C}$ is the reduced mass of the reaction. Similarly, the reaction probability can be expressed as

$$P_{react}(\mathbf{p}_0,\,\mathbf{q}_0) = \lim_{t\to\infty} \theta\left[f(\mathbf{q}_t(\mathbf{p}_0,\,\mathbf{q}_0))\right], \tag{1.1.4}$$

i.e. the collinear reaction takes place only if, for a given initial condition, the system can reach the "product side" from the "reaction side" and remains permanently in the

"reaction side". Hence, the thermal rate constant assumes the form

$$
\begin{aligned}
k(T) = & \frac{1}{\mathcal{Q}_{react}(T)} \int \frac{d\mathbf{p}_0\, d\mathbf{q}_0}{(2\pi\hbar)^F} \cdot \\
& e^{-\beta\mathcal{H}(\mathbf{p}_0,\,\mathbf{q}_0)} \delta\left(f(\mathbf{q}_0)\right) \vec{\nabla}_{\mathbf{q}} f(\mathbf{q}) \cdot \frac{\mathbf{p}_0}{\mu} \left[\lim_{t\to\infty} \theta\left[f\left(\mathbf{q}_t\left(\mathbf{p}_0,\,\mathbf{q}_0\right)\right)\right]\right] \\
= & \frac{1}{\mathcal{Q}_{react}(T)} \int_{\mathbf{q}_0 \in f^{-1}(0)} \int \frac{d\mathbf{q}_0\, d\mathbf{p}_0}{(2\pi\hbar)^F} \cdot \\
& \frac{\hat{\sigma}\cdot\mathbf{p}}{\mu} e^{-\beta\mathcal{H}(\mathbf{p}_0,\,\mathbf{q}_0)} \left[\lim_{t\to\infty} \theta\left[f\left(\mathbf{q}_t\left(\mathbf{p}_0,\,\mathbf{q}_0\right)\right)\right]\right], \qquad (1.1.5)
\end{aligned}
$$

where $\hat{\sigma} = \frac{\vec{\nabla}_{\mathbf{q}} f(\mathbf{q})}{\left|\vec{\nabla}_{\mathbf{q}} f(\mathbf{q})\right|}$ is the versor orthogonal to the dividing surface. This integral can be evaluated using classical Monte Carlo with a constrained sampling of classical trajectories at the dividing surface. Observe that the definition of thermal rate constant $k(T)$ given in Eq. (1.1.5) is independent of the choice of the dividing surface, since for any given initial sampling, i.e. dividing surface location, the Monte Carlo classical trajectories time evolution will adjust the value of the $\lim_{t\to\infty} \theta\left[f\left(\mathbf{q}_t\left(\mathbf{p}_0,\,\mathbf{q}_0\right)\right)\right]$.

1.2 Transition State Theory (TST)

The calculation of the thermal rate constant from Eq. (1.1.5) requires a Monte Carlo calculation or in general propagation of many phase space trajectories. To avoid this integration or propagation, in the sixties Eyring [1, 2], Evans and Polanyi [3] devised an approximation of Eq. (1.1.5), the transition state theory (TST). They found that the thermal rate constant is directly proportional to the concentration of these reactants multiplied by the frequency at which they are converted into products. The transition state is the geometry of the system at the maximum along the minimum energy path going from reactants to products and it is often called the "activated complex". The main assumptions for the validity of the TST are:

- Reactants are distributed following the usual Boltzmann-Maxwell distribution.
- It is not possible for the molecules to return to the reactant side after they cross the transition state. This means that any classical trajectory can cross the transition state only one time.
- At the transition state, the reaction coordinate s along to the minimum energy path of the collinear reaction potential can be separated from the other coordinates (see Fig. (1.2.1)).
- At the transition state, the motion along s can be treated as a classical translational motion.

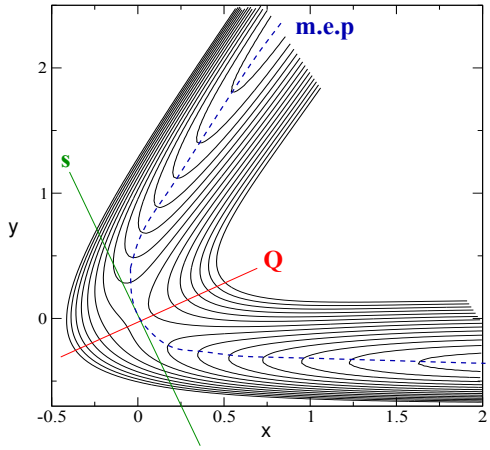

Figure 1.2.1: Example of potential energy level map for the collinear reaction $\mathrm{H} + \mathrm{H}_2 \rightarrow \mathrm{H}_2 + \mathrm{H}$. The blue-dotted curve is the minimum energy path (m.e.p.) and $(s,\ \mathbf{Q})$ represent respectively the reaction coordinate and its orthogonal coordinate.

In the rest of this Section we will provide a derivation of the TST and we will present all the limitation of the theory.

1.2.1 Derivation of the TST

For a generic reaction potential we can always identify a minimum energy path (see Fig. (1.2.1)). Let s the reaction coordinate along to the minimum energy path and $\mathbf{Q}$ its orthogonal direction: in this sense, s can be seen as the preferred low energy trajectory for the collinear reaction while $\mathbf{Q}$ represents small perturbations along such path. We expect to find a saddle-point $(s^*,\ \mathbf{Q}^*)$ which satisfies the conditions

$$\left.\frac{\partial^2 V}{\partial s^2}\right|_{s=s^*} < 0, \tag{1.2.1a}$$

$$\left|H_{\mathbf{Q}}\left(V\right)\right|_{\mathbf{Q}=\mathbf{Q}^*} > 0, \tag{1.2.1b}$$

where $H_{\mathbf{Q}}\left(V\right)$ is the Hessian of the surface reaction potential with respect to the generalized coordinates $\mathbf{Q}$. At this point, reactants are in quasi-equilibrium with the activated complex: if the reactant energy is larger than the activation energy $V_{sp} = V\left(s^*,\ \mathbf{Q}^*\right)$, reactants can form the activated complex which will transform into the products.

Without loss of generality, we will fix $s^* = 0$, where we will place the dividing surface.

By a canonical transformation $(\mathbf{p}_0,\, \mathbf{q}_0) \rightarrow (p_s,\, \mathbf{P},\, ,s,\, \mathbf{Q})$, Eq. (1.1.5) can be rewritten as

$$\begin{aligned} k\left(T\right) &= \frac{1}{\mathcal{Q}_{react}\left(T\right)} \int \frac{d\mathbf{P}\, d\mathbf{Q}\, dp_s\, ds}{\left(2\pi\hbar\right)^F} e^{-\beta\left(\frac{\mathbf{P}^2}{2M}+\frac{p_s^2}{2\mu}+V(s,\,\mathbf{Q})\right)} \delta\left(s\right) \frac{p_s}{\mu} P_{react}\left(p_s,\, \mathbf{P},\, s,\, \mathbf{Q}\right) \\ &= \frac{1}{\mathcal{Q}_{react}\left(T\right)} \int \frac{d\mathbf{P}\, d\mathbf{Q}\, dp_s}{\left(2\pi\hbar\right)^F} e^{-\beta\left(\frac{\mathbf{P}^2}{2M}+\frac{p_s^2}{2\mu}+V(0,\,\mathbf{Q})\right)} \frac{p_s}{\mu} P_{react}\left(p_s,\, \mathbf{P},\, 0,\, \mathbf{Q}\right), \end{aligned} \tag{1.2.2}$$

where $M = \frac{m_A m_B m_C}{m_A+m_B+m_C}$ is the reduced mass. Because of Eq. (1.2.1a) and of the orthogonality of s and $\mathbf{Q}$ at the transition point $(s^*,\, \mathbf{Q}^*)$, in the TST the reaction probability in Eq. (1.1.4) is approximated to

$$P_{react}\left(p_s,\, \mathbf{P},\, 0,\, \mathbf{Q}\right) \approx \theta\left(p_s\right). \tag{1.2.3}$$

The interpretation of this assumption is straightforward: the reaction will take place only if $p_s > 0$, i.e. if the classical trajectory is pointing from reactants to products. In this approximation, Eq. (1.2.2) assumes the form

$$\begin{aligned} k\left(T\right) &= \frac{1}{\mathcal{Q}_{react}\left(T\right)} \int \frac{d\mathbf{P}\, d\mathbf{Q}\, dp_s}{\left(2\pi\hbar\right)^F} e^{-\beta\left(\frac{\mathbf{P}^2}{2M}+\frac{p_s^2}{2\mu}+V(0,\,\mathbf{Q})\right)} \frac{p_s}{\mu} \theta\left(p_s\right) \\ &= \frac{e^{-\beta\, V_{sp}}}{2\pi\hbar} \int \frac{d\mathbf{P}\, d\mathbf{Q}}{\left(2\pi\hbar\right)^{F-1}} e^{-\beta\left(\frac{\mathbf{P}^2}{2M}+V(0,\,\mathbf{Q})-V_{sp}\right)} \int_0^\infty dp_s \frac{p_s}{\mu} e^{-\beta\frac{p_s^2}{2\mu}} \\ &= \frac{k_B T}{2\pi\hbar} e^{-\beta\, V_{sp}} \frac{\mathcal{Q}^\ddagger\left(T\right)}{\mathcal{Q}_{react}\left(T\right)}, \end{aligned} \tag{1.2.4}$$

where

$$\mathcal{Q}^\ddagger\left(T\right) = \int \frac{d\mathbf{P}\, d\mathbf{Q}}{\left(2\pi\hbar\right)^{F-1}} e^{-\beta\left(\frac{\mathbf{P}^2}{2M}+V(0,\,\mathbf{Q})-V_{sp}\right)} \tag{1.2.5}$$

is the partition function at the transition state geometry of the non-reactive degrees of freedom. The approximation in Eq. (1.2.4) is not taking into account the possibility that the classical trajectory will get back into the reactants basin in a finite amount of time. Therefore, using the TST, we reduced the multi-dimensional integration in Eq. (1.1.5) to the calculation of $\mathcal{Q}_{react}\left(T\right)$ and $\mathcal{Q}^\ddagger\left(T\right)$, which is much more amenable to Monte Carlo integrations. For collinear reactions at low temperature, the major contribution to $\mathcal{Q}_{react}\left(T\right)$ is given by vibrational motions around the minimal energy path. In particular, for 1-dimensional systems, $\mathcal{Q}^\ddagger = 1$ and $\mathcal{Q}_{react}\left(T\right)$ can be approximated to the partition function of a quantum oscillator $\mathcal{Q}_{react}\left(T\right) \approx \mathcal{Q}^O_{QM}\left(T\right) = \frac{1}{2\sinh\left(\frac{\beta\hbar\omega}{2}\right)}$, where ω is the characteristic frequency of the vibrational motion [38].

1.2.2 Correction to the TST

Even though the TST is widely applicable, it does have some limitations:

- TST fails when applied to fast multi-step reactions: in fact, TST assumes that each intermediate state is long-lived enough to reach the Boltzmann-Maxwell distribution of energies before continuing the next step. Otherwise, the momentum of the reaction trajectory between intermediate steps can carry forward to affect product selectivity.
- TST is also a classical theory for which collinear reactions does not occur unless molecules collide with enough energy to cross the reaction barrier.
- TST assumes a single passage through the transition state from reactants to products. However, it has been experimentally observed multiple passages through the transition states (re-crossing).
- TST is inaccurate at high temperature. In fact, the theory assumes the reaction system will pass over the lowest energy saddle point on the potential energy surface. While this description is consistent for reactions occurring at relatively low temperatures, at high temperatures, molecules populate higher energy vibrational modes; their motion becomes more complex and collisions may lead to transition states far away from the lowest energy saddle point.
- Finally, according to quantum mechanics, for any barrier with a finite amount of energy, there is a possibility that particles can still tunnel across the barrier, in particular at low temperature. With respect to chemical reactions this means that there is a chance that molecules will react even if they do not collide with enough energy to traverse the energy barrier.

Hence, a quantum approach of the thermal rate constant results fundamental for properly describe chemical reactions by including re-crossing (high temperatures) and tunneling (low temperatures).

1.3 Quantum Thermal Rate Constants

As described in the previous Section, classical approaches to the thermal rate constant do not correctly describe chemical reaction either in the re-crossing regime (high temperature) or in the tunneling regime (low temperature). To overcome this limitation, in 1983 Miller, Swartz and Tromp formulated [28] a method based on the quantum theory of density matrices to describe chemical reactions beyond the TST. In particular, they found

that quantum correlation functions can be used to compute the quantum thermal rate constant in the linear response theory regime.

Consider a system of reactants which is described at $t = 0$ by the canonical distribution density matrix $\hat{\rho}(0) = e^{-\beta\hat{\mathcal{H}}}\hat{\Theta}_r$, where the projection operator projects onto the reactant side $\hat{\Theta}_r$ and ensures that no products are present at the beginning. The probability $\mathcal{P}(t)$ to find a product at the time t can be expressed as

$$\mathcal{P}(t) = \frac{1}{\mathcal{Q}_{react}(T)} \mathrm{Tr}\left[\hat{\rho}(t)\,\hat{\Theta}_p\right], \tag{1.3.1}$$

where $\mathcal{Q}_{react} = \mathrm{Tr}\left[\hat{\rho}(0)\right] = \mathrm{Tr}\left[e^{-\beta\hat{\mathcal{H}}}\hat{\Theta}_r\right]$ is the partition function of the reactants, $\hat{\Theta}_p = 1 - \hat{\Theta}_r$ is the projector operator onto the product side of the Hilbert space and $\hat{\rho}(t) = e^{\frac{i}{\hbar}\hat{\mathcal{H}}t}\hat{\rho}(0)\,e^{-\frac{i}{\hbar}\hat{\mathcal{H}}t}$ is the density matrix in the Heisenberg representation. Recalling the definition of the $\hat{\rho}(0)$, Eq. (1.3.1) becomes

$$\mathcal{P}(t) = \frac{1}{\mathcal{Q}_{react}(T)} \mathrm{Tr}\left[e^{-\beta\hat{\mathcal{H}}}\hat{\Theta}_r e^{\frac{i}{\hbar}\hat{\mathcal{H}}t}\hat{\Theta}_p e^{-\frac{i}{\hbar}\hat{\mathcal{H}}t}\right]. \tag{1.3.2}$$

Since $\left[\hat{\mathcal{H}},\,\hat{\Theta}_r\right] \neq 0$,[1] the probability $\mathcal{P}(t)$ is not real quantity. However, only the real part has a physical meaning and it is related to the transition probability (the imaginary part becomes relevant only if adsorbing potentials are present). Therefore, it is possible to use an equivalent symmetric definition of $\mathcal{P}(t)$ defined as [29]

$$\mathcal{P}(t) = \frac{1}{\mathcal{Q}_{react}(T)} \mathrm{Tr}\left[e^{-\frac{\beta}{2}\hat{\mathcal{H}}}\hat{\Theta}_r e^{-\frac{\beta}{2}\hat{\mathcal{H}}} e^{\frac{i}{\hbar}\hat{\mathcal{H}}t}\hat{\Theta}_p e^{-\frac{i}{\hbar}\hat{\mathcal{H}}t}\right], \tag{1.3.3}$$

where the imaginary part is identically zero.

1.3.1 The Flux-Side and the Flux-Flux Correlation Function

In general, chemical reactions are non-linear and irreversible processes. However, in the approximation of quasi-equilibrium dynamics, the theory of linear response can be applied [39].

Given these considerations, we obtain from the definition of the thermal rate that

$$k(T) = -\dot{\mathcal{P}}(t).$$

[1] Suppose that $\left[\hat{\mathcal{H}},\,\hat{\Theta}_r\right] = 0$. Recalling that $\hat{\Theta}_p = 1 - \hat{\Theta}_r$, the probability to find a product $\mathcal{P}(t)$ in Eq. (1.3.2) becomes

$$\mathcal{P}(t) = \frac{1}{\mathcal{Q}_{react}(T)} \mathrm{Tr}\left[e^{-\beta\hat{\mathcal{H}}}\hat{\Theta}_r\hat{\Theta}_p\right],$$

which is identically zero because a state cannot be at the same time both a reactant and a product.

Using the definition of $\mathcal{P}(t)$ in Eq. (1.3.3) and recalling that

$$\frac{d\hat{\Theta}_r(t)}{dt} = -\frac{d\hat{\Theta}_p(t)}{dt} = -\frac{i}{\hbar}\left[\hat{\mathcal{H}},\, \hat{\Theta}_p(t)\right] = -e^{\frac{i}{\hbar}\hat{\mathcal{H}}t}\hat{\mathcal{F}}e^{-\frac{i}{\hbar}\hat{\mathcal{H}}t}, \tag{1.3.4}$$

where $\hat{\mathcal{F}}$ is the flux operator, we finally find

$$k(T) = \frac{1}{\mathcal{Q}_{react}(T)} \lim_{t\to+\infty} C_{fs}(t, T), \tag{1.3.5}$$

where we defined the flux-side correlation function as

$$C_{fs}(t, T) = -\dot{\mathcal{P}}(t) = \mathrm{Tr}\left[e^{-\frac{\beta}{2}\hat{\mathcal{H}}}\hat{\mathcal{F}}e^{-\frac{\beta}{2}\hat{\mathcal{H}}}e^{\frac{i}{\hbar}\hat{\mathcal{H}}t}\hat{\Theta}_p e^{-\frac{i}{\hbar}\hat{\mathcal{H}}t}\right]. \tag{1.3.6}$$

Intuitively, the flux-side correlation function "counts" the rate at which reactants become products and it correctly has the dimensions of $\left[t^{-1}\right]$. Equivalently, it is possible to substitute the limit with an integral using the identity

$$C_{fs}(t, T) = \int_0^t dt'\, C_{ff}(t', T) \tag{1.3.7}$$

where

$$C_{ff}(t, T) = \mathrm{Tr}\left[e^{-\frac{\beta}{2}\hat{\mathcal{H}}}\hat{\mathcal{F}}e^{-\frac{\beta}{2}\hat{\mathcal{H}}}e^{\frac{i}{\hbar}\hat{\mathcal{H}}t}\hat{\mathcal{F}}e^{-\frac{i}{\hbar}\hat{\mathcal{H}}t}\right] \tag{1.3.8}$$

is the flux-flux correlation function. Finally, the quantum thermal rate constant assumes the form

$$k(T) = \frac{1}{\mathcal{Q}_{react}(T)} \int_0^{+\infty} dt\, C_{ff}(t, T). \tag{1.3.9}$$

1.3.2 The flux-averaging method (FAM)

For the case of resonant tunneling simulations as in the present PhD thesis, Eq. (1.3.9) does not converge in a feasible amount of time. Resonant metastable states stretch the simulation time to becoming almost exponential with the number of quasi-bound states between the barrier. For this reasons, a variant of the Miller, Swartz and Tromp's formula, Eq. (1.3.9), has been put forward by Peskin et al. [31]. Such variant is called the "flux averaging" method (FAM) and it allows the calculation of the thermal rate constants for double barrier potentials. The method takes advantage of the fact that, after a certain amount of time, the ratio of the fluxes in entrance to fluxes in exit channels is roughly constant. Once the ratio is defined, one can obtain the asymptotic-time limit of the flux auto-correlation function. More specifically, two dividing surfaces are employed and

placed at the top of each barrier and two correlation functions are introduced: $C_{RR}(t)$ when both dividing surfaces are located at the top of the first barrier (the reactants side) and $C_{RP}(t)$ when the dividing surfaces are located at each barrier top (reactant and product side respectively). Since Eq. (1.3.9) is exact, each correlation function gives the exact thermal rate as well as any weighted linear combination. Peskin [32] found that a suitable combination is

$$k(T)\,\mathcal{Q}_{react}(T) = \lim_{t\to+\infty}\left(\frac{|C_{RR}(t)|\int_0^t C_{RP}(t')\,dt'}{|C_{RP}(t)|+|C_{RR}(t)|} + \frac{|C_{RP}(t)|\int_0^t C_{RR}(t')\,dt'}{|C_{RP}(t)|+|C_{RR}(t)|}\right). \tag{1.3.10}$$

Although this approach is very powerful in many cases of interest [31–34], re-crossing phenomena can lead to a significant increase of the total computational time needed to reach convergence. Furthermore, this method usually employs imaginary absorbing potentials because the dynamics involves a long-time decay beyond the barrier region: the expression and location of such absorbing potentials is quite arbitrary and their presence can lead to fictitious effects. These shortcomings call for a better approach to tackle the calculation of the thermal rate constant. We will see some examples of the numerical challenge involved in using the FAM method to evaluate the rate constant in potentials with several resonances in Chap. 3. Further, we will present our approach to remedy this in Chap. 4.

CHAPTER 2

Time Dependent Methods vs. Time Independent Method.

As described in the previous Chapter, the thermal rate constant $k(T)$ can be expressed in terms of flux operators $\hat{\mathcal{F}} = \frac{d\hat{\Theta}_p(t)}{dt} = \frac{i}{\hbar}\left[\hat{\mathcal{H}}, \hat{\Theta}_p(t)\right]$, Eq. (1.3.9) by the expression:

$$k(T) = \frac{1}{\mathcal{Q}_{react}(T)} \lim_{t\to\infty} C_{fs}(t, T) \tag{2.0.1a}$$

$$= \frac{1}{\mathcal{Q}_{react}(T)} \int_0^{+\infty} dt\, C_{ff}(t, T), \tag{2.0.1b}$$

where

$$C_{fs}(t, T) = \mathrm{Tr}\left[e^{-\frac{\beta}{2}\hat{\mathcal{H}}}\hat{\mathcal{F}}e^{-\frac{\beta}{2}\hat{\mathcal{H}}}e^{\frac{i}{\hbar}\hat{\mathcal{H}}t}\hat{\Theta}_p e^{-\frac{i}{\hbar}\hat{\mathcal{H}}t}\right], \tag{2.0.2a}$$

$$C_{ff}(t, T) = \mathrm{Tr}\left[e^{-\frac{\beta}{2}\hat{\mathcal{H}}}\hat{\mathcal{F}}e^{-\frac{\beta}{2}\hat{\mathcal{H}}}e^{\frac{i}{\hbar}\hat{\mathcal{H}}t}\hat{\mathcal{F}}e^{-\frac{i}{\hbar}\hat{\mathcal{H}}t}\right]. \tag{2.0.2b}$$

are respectively the flux-side and the flux-flux correlation functions. In this Chapter we will provide the derivation of a time-dependent and a time-independent approach in a representation suitable to the numerical calculation of the thermal rate constant. In particular, we will discuss the reason why the time-independent approach is preferable than the time-dependent approach for resonant tunneling.simulations.

2.1 The Time-Dependent Approach

Given a system described by the time independent Hamiltonian $\hat{\mathcal{H}} = -\frac{\hbar^2}{2m}\nabla^2 + V(x)$ and its set of eigenstates $|n\rangle$ and eigenvalues ϵ_n[1]

$$\hat{\mathcal{H}}|n\rangle = \epsilon_n |n\rangle, \tag{2.1.1}$$

[1] In general, we must consider both the discrete and continuous spectrum of the Hamiltonian. However, the explicit calculation of eigenstates requires a discretization of the Hilbert space, which inevitably leads to a discrete spectrum.

the flux-flux correlation function in Eq. (2.0.2b) can be expressed as

$$C_{ff}(t,\,T) = \sum_{m,\,n} e^{-\frac{\beta}{2}(\epsilon_n+\epsilon_m)} e^{-\frac{i}{\hbar}(\epsilon_n-\epsilon_m)t}\ |\mathcal{F}_{nm}|^2\,, \tag{2.1.2}$$

where $\mathcal{F}_{nm}$ is the matrix element of a Flux operator, defined as

$$\mathcal{F}_{nm} = \frac{i}{\hbar}\langle n|\left[\hat{\mathcal{H}},\,\hat{\Theta}_p\right]|m\rangle = \frac{i}{\hbar}(\epsilon_n-\epsilon_m)\langle n|\,\hat{\Theta}_p\,|n\rangle\,. \tag{2.1.3}$$

Here, $\hat{\Theta}_p$ is a Heaviside operator in momentum space. The expression in Eq. (2.1.3) can be further simplified by introducing the reaction coordinate $(s,\,\mathbf{Q})$, as described in Sec. 1.2, in fact we see that

$$\chi_{nm} \equiv \langle n|\,\hat{\Theta}_p\,|m\rangle = \int d\mathbf{Q},\,ds\,\theta(s-s^*)\,\psi_n(s,\,\mathbf{Q})\,\psi_m(s,\,\mathbf{Q})\,, \tag{2.1.4}$$

where s^* is the position of the transition state, located somewhere between reactants and products and $\theta(s-s^*)$ is the Heaviside function. Hence, the flux-flux correlation function can be rewritten as

$$C_{ff}(t,\,T) = \sum_{m,\,n} e^{-\frac{\tilde{\beta}}{2}(\omega_n+\omega_m)} e^{-i(\omega_n-\omega_m)t}\ (\omega_n-\omega_m)^2\,|\chi_{nm}|^2\,, \tag{2.1.5}$$

where we defined $\omega = \epsilon/\hbar$ and $\tilde{\beta} = \hbar\beta$. The thermal rate constant defined in Eq. (2.0.1) now assumes the form

$$\begin{aligned} k(T)\ \mathcal{Q}_{react}(T) &= \int_0^{+\infty} dt\, C_{ff}(t,\,T) \\ &= \Re\left[\sum_{m,\,n} e^{-\frac{\tilde{\beta}}{2}(\omega_n+\omega_m)}\ (\omega_n-\omega_m)^2\,|\chi_{nm}|^2 \int_0^{\infty} dt\, e^{-i(\omega_n-\omega_m)t}\right] \\ &= \lim_{t\to+\infty} C_{fs}(t,\,T)\,, \end{aligned} \tag{2.1.6}$$

where

$$\begin{aligned} C_{fs}(t,\,T) &= \sum_{m,\,n} e^{-\frac{\tilde{\beta}}{2}(\omega_n+\omega_m)}\ (\omega_n-\omega_m)^2\,|\chi_{nm}|^2\,t\,\mathrm{sinc}\left((\omega_n-\omega_m)\,t\right) \\ &= \sum_{m,\,n} e^{-\frac{\tilde{\beta}}{2}(\omega_n+\omega_m)}\ (\omega_n-\omega_m)\,|\chi_{nm}|^2\,\sin\left((\omega_n-\omega_m)\,t\right). \end{aligned} \tag{2.1.7}$$

In order to compute Eq. (2.1.7) numerically, a prescription for the discretization of

the Hilbert space given by the Hamiltonian in Eq. (2.1.1) is required. In our case, we considered the "Discrete Variable Representation" (or simply sinc-DVR) (see App. A for more details). In this approximation, the coordinate space $[-L,\, L]^d$, where d is the system's dimension, is divided in a $N = \left(\frac{L}{\Delta x}\right)^d$ cell of edge Δx. In the sinc-DVR approximation localized basis functions ϕ_n are introduced

$$\phi_n\left(x\right) = \frac{1}{\sqrt{\Delta x}} \frac{\sin\left(\frac{\pi\left(x-x_n\right)}{\Delta x}\right)}{\left(\frac{\pi\left(x-x_n\right)}{\Delta x}\right)} = \frac{1}{\sqrt{\Delta x}} \mathrm{sinc}\left(\frac{\pi\ \left(x-x_n\right)}{\Delta x}\right), \tag{2.1.8}$$

as set of orthonormal functions for the discretized Hilbert space. Here, x_j is defined as the coordinate of the center of the $j-th$ cell,. In this representation, the matrix element $H_{nm} = \langle\phi_n|\,\hat{\mathcal{H}}\,|\phi_m\rangle$ assumes the simple form

$$H_{nm} = T_{nm} + V_{nm}, \tag{2.1.9}$$

where

$$T_{nm} = \frac{\hbar^2\left(-1\right)^{n-m}}{2m\Delta x^2} \cdot \begin{cases} \frac{\pi^2}{3} & n = m \\ \frac{2}{(n-m)^2} & n \neq m \end{cases}, \tag{2.1.10}$$

and

$$V_{nm} = \delta_{nm}\, V(x_n). \tag{2.1.11}$$

Observe that H_{nm} is a *dense* matrix, in the sense that off-diagonal elements approach zero only as a power-law. Similar results would have been obtained if we had used the moment space representation for the Hilbert space of $\hat{\mathcal{H}}$.

Although the above "time-dependent" approach has been widely used for the explicit computation of thermal rate constants [40–42], it presents many numerical problems. In particular,

- Eq. (2.1.7) is not well defined for large t due to the presence of the quickly oscillating term $\sin\left(\left(\omega_n - \omega_m\right)t\right)$, which is peaked around $\omega_n \approx \omega_m$. However, the term $\left(\omega_n - \omega_m\right)$ in Eq. (2.1.6) tends to suppress the contribution of eigenstates with the same eigenvalue.

- Because Eq. (2.1.6) is exact in the limit of $t \to \infty$, we expect the existence of a plateau for the flux-side correlation function $C_{fs}\left(t,\, T\right)$ in correspondence with the value of the thermal rate constant. However, as shown in Fig. (2.1.1), due to finite size effects as well as numerical machine errors, the plateau strongly depends on the discretization and it loses its coherence for very large value of t. Hence, $C_{fs}\left(t,\, T\right)$

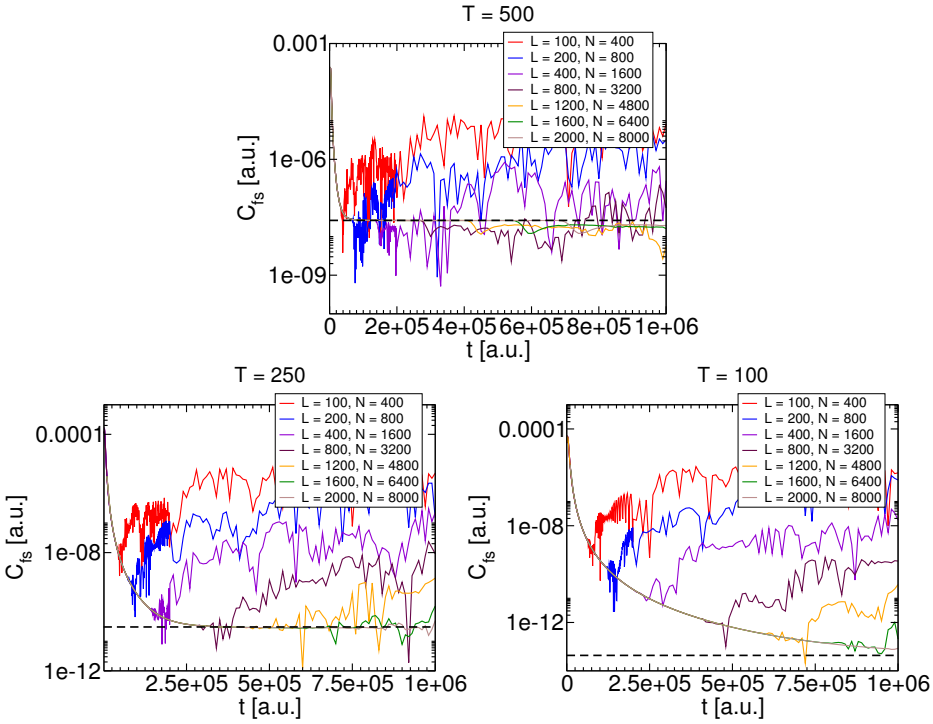

Figure 2.1.1: Flux-side correlation function as defined in Eq. (2.1.7), for a single Eckart barrier potential of the form $V(x) = \frac{V_0}{\cosh^2\left(\frac{\pi x}{\Delta}\right)}$, where $V_0 = 1.560 \times 10^{-2}$ a.u. and $\Delta = 2,30593$ a.u. As the temperature is reduced, the number of grid-points in the DVR approximation must be increased in order to correctly reach the asymptotic limit in Eq. (2.1.6).

must be computed for many distinct times in order to correctly find the plateau, and then the thermal rate constant.

- In order to compute Eq. (2.1.7), it is necessary to know both the eigenstates (through χ_{nm}) and eigenenergies (through ω_n) of the Hamiltonian in Eq. (2.1.1). In the sinc-DVR representation, the total number of eigenstates is $N = \left(\frac{L}{\Delta x}\right)^d$. Hence, the computation time required to compute the eigenproblem scales as $\mathcal{O}_{EP} = O\left(N^3\right)$, and the amount of memory scales as $\mathcal{M}_{EP} = O\left(N^2\right)$. Observe that the total amount of memory necessary for the computation of the eigenproblem becomes quickly unfeasible: indeed, for $N = 10^4$ the total amount of memory needed to store one of the operators is $\mathcal{M}_{EP} \approx 1.6$ Gb (using a `long double` representation of real number).

In Fig. (2.1.1), the results of an explicit calculation of $C_{fs}(t, T)$ for an one dimensional single barrier potential of the form $V(x) = \frac{V_0}{\cosh^2\left(\frac{\pi x}{\Delta}\right)}$, where $V_0 = 1.560 \times 10^{-2}$ a.u. and $\Delta = 2.30593$ a.u., are given. At high temperature, the flux-side correlation function

quickly converges to the thermal rate constant value. As expected, both the convergence time t and the number of necessary eigenstates N increases as the temperature T is decreased.

In conclusion, the time-dependent approach to the thermal rate constant $k\left(T\right)$ becomes quickly unfeasible for low temperature. As described in the Introduction, we are interested in studying resonant tunneling whose effects become relevant at very low temperature. Hence, a time-independent approach is fundamental in order to study systems at low energy quantum systems. We will elaborate further on this aspect in the next Chapter.

2.2 The Time-Independent Approach

As described in Sec. 2.1 and in Chap. 3, time-dependent approaches become computationally demanding at very low temperature, when resonant tunneling becomes relevant. Hence, a time-independent approach is preferred in this case for the calculation of the thermal rate constant $k\left(T\right)$. In order to switch from the time-domain to the energy-domain, it is necessary to integrate out the time dependence in Eq. (2.0.2b) [28]. After inserting the following identity in Eq. (2.0.2b)

$$e^{-\hat{H}(\beta/2+it/\hbar)}=\int_{-\infty}^{+\infty}e^{-E(\beta/2+it/\hbar)}\,\delta\Big(E-\hat{H}\Big)\,dE \tag{2.2.1}$$

and integrating over time, a time-independent expression for the thermal rate constant is obtained [28]

$$k\left(T\right)Q_{react}\left(T\right)=\frac{1}{2\pi\hbar}\int_{-\infty}^{+\infty}e^{-\beta E}N\left(E\right)dE, \tag{2.2.2}$$

where

$$N\left(E\right)=\frac{1}{2}\left(2\pi\hbar\right)^{2}\mathrm{Tr}\left[\hat{F}_{1}\,\delta\Big(E-\hat{H}\Big)\,\hat{F}_{2}\,\delta\Big(E-\hat{H}\Big)\right] \tag{2.2.3}$$

is the cumulative reaction probability evaluated between the dividing surface $f_{1}\left(\mathbf{s}\right)=0$ and $f_{2}\left(\mathbf{s}\right)=0$. Eqs. (2.2.2) and (2.2.3) have been successfully used in the past for several quantum rate calculations [14, 43–50]. In particular, Manthe et al. [51, 52] have been able to calculate the exact quantum rate for the hydrogen abstraction reaction from methane $\mathrm{H}+\mathrm{CH_{4}}\rightarrow\mathrm{H_{2}}+\mathrm{CH_{3}}$. Despite their apparent simplicity, Eqs. (2.2.2) and (2.2.3) can be solved analytically only for a limited number of problems and a numerical approach is necessary otherwise. Eq. (2.2.3) closely resembles the Landauer [53–56] formalism equations employed to calculate the electrical and heat current.

2.2.1 Cumulative reaction probability and probability current

In general, the numerical computation of Eq. (2.2.3) requires the study of the entire spectrum of the Hamiltonian, as in the time-dependent approach. To overcome this problem, in this Section we provide a useful expression for the cumulative reaction probability $N(E)$ in terms of probability currents. In particular, we take advantage of the fact that, in the asymptotic limit and for one dimensional scattering potentials, probability currents are related in a simple manner to eigenfunctions.

Consider a non-adsorbing potential $V(x)$ which is different from zero only in a closed region of the space $\mathcal{S} \subset [-L, L]^d$, with $L \gg 1$. Due to energy conservation, any eigenstate of the Hamiltonian $\hat{\mathcal{H}}$ will assume the form of a free particle far from the "scattering region" $\mathcal{S}$. Hence, eigenstates $|\psi_p\rangle$ can be classified by their momentum p assuming that we are far from the scattering interaction region $\mathcal{S}$. Therefore, after inserting the resolution of the identity $|\psi_p\rangle\langle\psi_p|$, Eq. (2.2.3) becomes

$$\begin{aligned} N(E) &= \frac{1}{2}(2\pi\hbar)^2 \iint dp\, dp'\, \delta(E(p) - E)\, \delta(E(p') - E) \\ &\times \langle\psi_p|\hat{F}_1|\psi_{p'}\rangle\langle\psi_{p'}|\hat{F}_2|\psi_p\rangle . \end{aligned} \tag{2.2.4}$$

where the integration over the momenta p and p' denotes the sum over all eigenfunctions [2]. Using the definition of the flux operators in Eq. (1.3.4), the flux matrix elements become

$$\langle\psi_p|\hat{F}_1|\psi_{p'}\rangle = \frac{d}{dt}\int_{-\infty}^{+\infty} d\mathbf{s}\, \psi_p^\star(\mathbf{s})\, \hat{h}(f_1(\mathbf{s}))\, \psi_{p'}(\mathbf{s}) \tag{2.2.5a}$$

$$= \int_{f_1(\mathbf{s})\geqslant 0} d\mathbf{s}\, \frac{d}{dt}\left(\psi_p^\star(\mathbf{s})\, \psi_{p'}(\mathbf{s})\right) \tag{2.2.5b}$$

where the integration in Eq. (2.2.5b) is limited to the regions where $f_1(\mathbf{s}) \geqslant 0$ (products region). Using the continuity equation

$$\frac{d}{dt}\left(\psi_p^\star(\mathbf{s})\, \psi_{p'}(\mathbf{s})\right) = \vec{\nabla}_{\mathbf{s}} \cdot \vec{j}_{pp'}(\mathbf{s}) , \tag{2.2.6}$$

where

$$\vec{j}_{pp'}(\mathbf{s}) = -\frac{i\hbar}{2m}\left[\psi_p^*(\mathbf{s})\vec{\nabla}_{\mathbf{s}}\psi_{p'}(\mathbf{s}) - \vec{\nabla}_{\mathbf{s}}\psi_p^\star(\mathbf{s})\psi_{p'}(\mathbf{s})\right] \tag{2.2.7}$$

is the probability current, and then, applying the "Divergence Theorem", the expression

[2] Here we prefer to adopt the integration at the place of the sum, since the spectrum is continuous far from the scattering interaction region

of the flux matrix elements becomes

$$\langle \psi_p | \, \hat{F}_1 \, | \psi_{p'} \rangle = \int_{f_1(\mathbf{s})=0} d\mathbf{s} \, \vec{j}_{pp'} \left(\mathbf{s} \right) \cdot \vec{\mathbf{n}}_1 \tag{2.2.8}$$

where $\vec{\mathbf{n}}_1$ is a unit vector normal to the dividing surface $f_1 \left(\mathbf{s} \right) = 0$. After substituting Eq. (2.2.8) into Eq. (2.2.4) for both flux operators, the expression of the cumulative reaction probability in terms of the probability current becomes

$$\begin{aligned} N \left(E \right) &= \frac{1}{2} (2\pi\hbar)^2 \iint dp \, dp' \, \delta(E \left(p \right) - E) \; \delta(E \left(p' \right) - E) \\ &\times \left(\int_{f_1(\mathbf{s})=0} d\mathbf{s} \, \vec{j}_{pp'} \left(\mathbf{s} \right) \cdot \vec{\mathbf{n}}_1 \right) \left(\int_{f_2(\mathbf{s}')=0} d\mathbf{s}' \, \vec{j}_{pp'} \left(\mathbf{s}' \right) \cdot \vec{\mathbf{n}}_2 \right)^{\star} . \end{aligned} \tag{2.2.9}$$

In this thesis, resonant rate calculations are carried out for arbitrary one dimensional scattering potentials $V(x)$, with the asymptotic condition $V(x) = 0$ for x far from the scattering region $\mathcal{S} = [-L_{\mathcal{S}}, \, L_{\mathcal{S}}]$. Therefore, we can assume that the dividing surface equation is of the form $f \left(x \right) = x - x_0 = 0$, where x_0 is the position of the dividing surface. As introduced in Sec. 2.1, a convenient choice of the flux operators has often been to place them one in the reactants and the other in the products side, in particular for resonant scattering. Here, we choose to place them in the same asymptotic location $f_1 \left(x \right) = f_2 \left(x \right) = x - x_0$. It is important to remember that the actual rate constant is independent of the location of the dividing surfaces, but appropriate choices of the dividing surfaces locations may reduce the computational effort required to evaluate the thermal rate constant. Given this choice, after integrating at the dividing surface point, Eq. (2.2.9) becomes

$$\begin{aligned} N \left(E \right) &= \frac{1}{2} (2\pi\hbar)^2 \iint dp \, dp' \, \delta(E \left(p \right) - E) \\ &\times \delta(E \left(p' \right) - E) \left| j_{pp'} \left(x_0 \right) \right|^2 , \end{aligned} \tag{2.2.10}$$

where the cumulative reaction probability can clearly be interpreted as a counter of the number of particles that cross the dividing surface.

In order to calculate $T \left(E \right)$ from asymptotic conditions, one needs the expression of the eigenfunctions $|\psi_p\rangle$ in these regions. When a wave is incoming (left to right), the eigenfunctions are

$$\psi_p^R(x) = \begin{cases} \frac{1}{\sqrt{2\pi\hbar}} \left(\mathrm{e}^{ipx/\hbar} + r \, \mathrm{e}^{-ipx/\hbar} \right) & x \ll -L_{\mathcal{S}} \\ \frac{1}{\sqrt{2\pi\hbar}} t \, \mathrm{e}^{ipx/\hbar} & x \gg +L_{\mathcal{S}} \end{cases} \tag{2.2.11a}$$

and when it is outgoing (right to left) they are

$$\psi_p^L(x) = \begin{cases} \frac{1}{\sqrt{2\pi\hbar}} t\, \mathrm{e}^{-ipx/\hbar} & x \ll -L_{\mathcal{S}} \\ \frac{1}{\sqrt{2\pi\hbar}} \left(\mathrm{e}^{-ipx/\hbar} - r\, \mathrm{e}^{ipx/\hbar}\right) & x \gg +L_{\mathcal{S}} \end{cases} \tag{2.2.11b}$$

where the energy for both eigenfunctions is set to $E = p^2/2m$ and no absorbing potential is employed. Depending of the choice of the dividing surface, one will use Eqs. (2.2.11) for the case of $x_0 \gg +L_{\mathcal{S}}$ or $x_0 \ll -L_{\mathcal{S}}$. Recalling that $T = |t|^2$ and $R = |r|^2$ represent respectively the transmission and reflection coefficients with $R + T = 1$, it can be shown that for both asymptotic choices of x_0, the values of the probability currents are

$$j_{pp}^{RR}(x_0) = \frac{T}{\pi\hbar}\sqrt{\frac{E}{2\,m}} \tag{2.2.12a}$$

$$j_{pp}^{LL}(x_0) = \frac{R-1}{\pi\hbar}\sqrt{\frac{E}{2\,m}} \tag{2.2.12b}$$

$$j_{pp}^{RL}(s_0) = j_{pp}^{LR}(x_0)^* = \frac{r\,t^*}{\pi\hbar}\sqrt{\frac{E}{2\,m}}, \tag{2.2.12c}$$

where the steady state flux conservation relation $t^* r + r^* t = 0$ is used to show that Eqs. (2.2.12) are the same for the case of $x_0 \gg +L_{\mathcal{S}}$ and $x_0 \ll -L_{\mathcal{S}}$. Taking into account the fact that the overall probability current is the sum over all possible probability currents (right to right, right to left, etc.) [57], Eq. (2.2.10) becomes

$$\begin{aligned} N(E) &= \frac{1}{2}(2\pi\hbar)^2 \rho(E)^2 \left(\left|j_{pp}^{RR}(s_0)\right|^2 + \left|j_{pp}^{LL}(s_0)\right|^2 + 2\left|j_{pp}^{LR}(s_0)\right|^2\right) \\ &= \frac{1}{2}(2\pi\hbar)^2 \rho(E)^2 \frac{E}{m\pi^2\hbar^2} T(E) \end{aligned} \tag{2.2.13}$$

where $\rho(E)$ is the density of states for $x_0 \gg +L_{\mathcal{S}}$ or $x_0 \ll -L_{\mathcal{S}}$ and where we explicitly indicate the energy dependence of the transmission coefficient $T(E)$. [53] For one dimensional systems, the free-particle density of states is $\rho(E) = \sqrt{m/2E}$ and then the cumulative reaction probability $N(E)$ results to be exactly the transmission probability $T(E)$. Finally, we can compute the thermal rate constant directly for arbitrary one-dimensional potential as

$$k(T)\, Q_{react}(T) = \frac{1}{2\pi\hbar}\int_{-\infty}^{+\infty} e^{-\beta E} T(E)\, dE. \tag{2.2.14}$$

CHAPTER 3

Limitations of the Time-Dependent Approach in Deep Resonant Tunneling Regime

In this Chapter we apply the time-dependent Flux-averaging method (FAM), as described in Sec. 1.3.2 to a series of double barrier potentials at different temperatures. FAM is currently the most accredited method for this kind of problems. In particular we will consider the three potentials represented in Fig. (3.0.1):

- The Lefebvre potential

$$V(x) = \frac{V_E}{\cosh^2(x)} - \frac{0.75\, V_I}{\cosh^2(2x)}, \tag{3.0.1a}$$

  where $V_E = 0.425$ eV and $V_I = 0.546$ eV.

- The Peskin potential

$$V(x) = V_0 \left(\frac{1}{\cosh^2(x)} - \frac{1}{\cosh^2(a\,x)} \right), \tag{3.0.1b}$$

  where $V_0 = 0.310$ eV.

- A well separated double barrier potential of the form

$$V(x) = V_0 \left(\frac{1}{\cosh^2(x-a)} + \frac{1}{\cosh^2(x+a)} - \frac{2}{\cosh^2(a)\cosh^2(x)} \right), \tag{3.0.1c}$$

  where $V_0 = 0.310$ eV and $a = 2$ a.u.

In all *cases*, we used a mass $m = 1.834 \times 10^3$ a.u. The first potential, indicated as the Peskin potential is the one used in ref. [32] to test the flux-averaging method, the second potential is the Lefebvre potential which was employed in ref. [30] as an example of a potential were resonances are present. The third potential, indicated as "Wider potential"

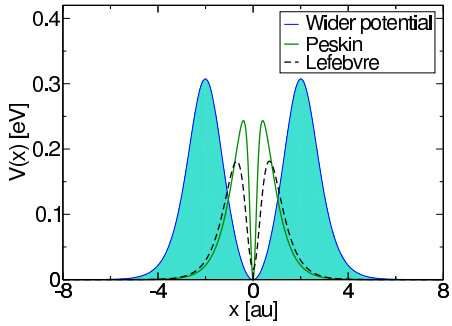

Figure 3.0.1: Plot of the three double well potentials considered in this Chapter.

in the caption is the potential employed in our present work, also used in Chap. 5 to test our new time-independent method. This last potential supports many more resonances than the first two and it is thus a much more severe potential in terms of convergence of the time-dependent methods. We will now proceed to test the FAM method for these potentials first at a high temperature $T = 500K$ and then at lower temperatures to show that when resonances become dominant the method fails to converge in a feasible amount of simulation time.

3.1 Benchmark case T=500K

As described in Sec. 1.3.2, the thermal rate constant can be evaluated as a "flux-average"

$$\mathcal{Q}_{react}(T)\, k(T) = \lim_{t\to+\infty} \left(\frac{|C_{RR}(t)| \int_0^t C_{RP}(t')\, dt'}{|C_{RP}(t)| + |C_{RR}(t)|} + \frac{|C_{RP}(t)| \int_0^t C_{RR}(t')\, dt'}{|C_{RP}(t)| + |C_{RR}(t)|} \right). \tag{3.1.1}$$

We begin by considering *the* case of $T = 500$ K which was used by Peskin et al. [32] to benchmark the FAM. We evaluated the time integrals $\int_0^t C_{RP}(t')\, dt'$, $\int_0^t C_{RR}(t')\, dt'$ and $\mathcal{Q}_{react}(T)\ k(T)$ at those temperatures as a function of time t using the DVR approach with the sync basis set (See Sec. 2.1 and App. A). We found that the converged (up to three significant figures at 80, 100 and 500K) grid density corresponds to take $\Delta x \leq 0.05$ a.u. For the first two potentials the grid was taken such that $x \in [-16 \text{ a.u.}, 16 \text{ a.u.}]$ with a number of DVR points $n = 701$ and for the third potential, which is wider, we used a grid of $x \in [-20 \text{ a.u.}, 20 \text{ a.u.}]$ with $n = 1001$.

As you can see in Fig. (3.1.1a), the FAM method works well only for the Peskin potential. In fact, within 6000 a.u. the $\mathcal{Q}_{react}(T)\, k(T)$ integral function converges to a

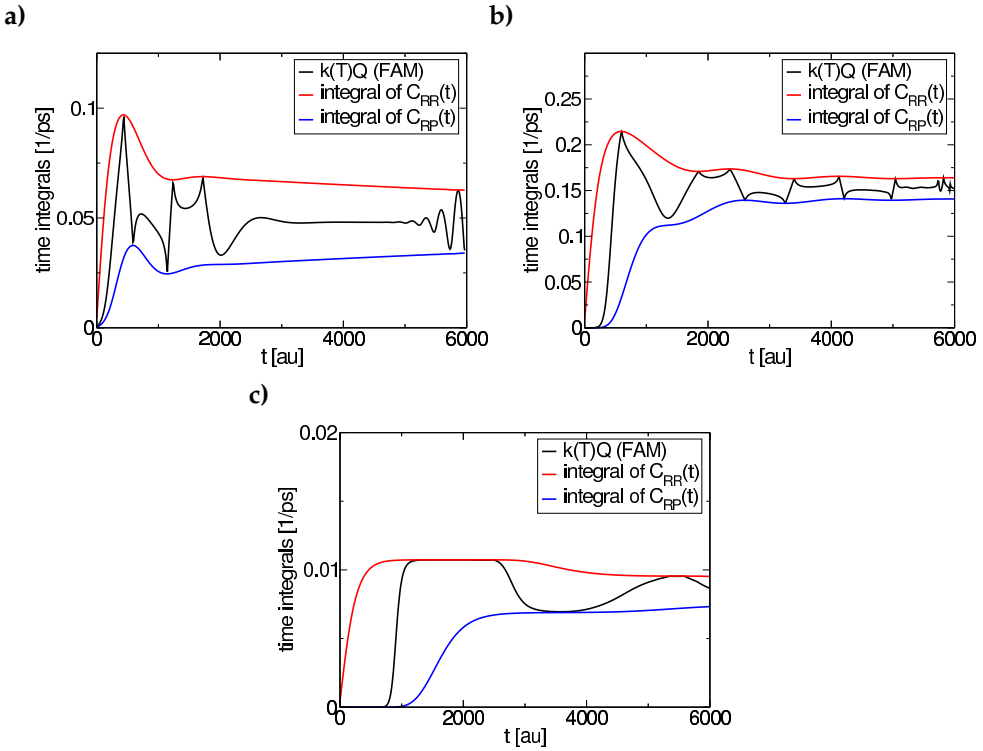

Figure 3.1.1: Plot of the time integrals $\int_0^t C_{RP}\,(t')\,dt'$, $\int_0^t C_{RR}\,(t')\,dt'$ and of the average value of thermal rate constant $\mathcal{Q}_{react}\,(T)\,k\,(T)$ in Eq. (3.1.1), for each of the three potentials in Eqs. (3.0.1), at $T = 500$ K . The DVR parameters are given in the text.

constant. The wiggly behavior which follows the constant interval (at about 6000 a.u.), is due to the finite size of the grid. We will see in the next Section however that as soon as one lowers the temperature the FAM method does not converge anymore within 6000 a.u. of time. In Fig. (3.1.1b), the method is applied to the Lefebvre potential at 500K. In this case, for this slightly wider potential, the method fails. In fact, the thermal rate constant $k\left(T\right)$ keeps oscillating and does not reach a constant value. Even within a longer time propagation of 10000 a.u. the function did not converge. One should keep in mind that because of the way the FAM method is expressed e.g Eq. (1.3.10) it is not possible to parallelize the time evolution and the simulation time scales linearly in time. One other problem to bear in mind is the fact that given more time, the edges of the grid may start to influence the result and one will need to use a larger grid, i.e. more grid points and thus more memory. In Fig. (3.1.1c) we apply the method to an even wider potential and here we see that the oscillatory behavior of the thermal rate constant $k\left(T\right)$ prevents one from getting any information of the correct value of the kinetic rate constant within the propagation time.

3.2 Lower temperatures

Already at 500 K we saw the limitations of the FAM *method*. The FAM convergence highly depends on the type of potential, even at that rather high temperatures. Now, we investigate on how the method converges in the low temperature regime where quantum effects become dominant. In this case we repeat the calculations, on both the Peskin and wider potentials with the same DVR parameters. A similar behavior is observed for the Lefebvre potential. The *results* are shown in Figs. (3.2.1). Temperatures for the first row, Figs. (3.2.1a, b), and second row, Figs. (3.2.1c, d), are respectively set to $T = 100$ K and $T = 80$ K. We see that for neither one of the potentials the thermal rate constant in Eq. (3.1.1) converges within the 6000 a.u. propagation interval and nor do the two integrals of $C_{RR}(t)$ and $C_{RP}(t)$. In the long time limit one should see that integrals of C_{RR} and C_{RP} slowly approach the same value. However, at these low temperatures, we are very far from this limit even after 6000 a.u. To obtain convergence one would need a much longer propagation time and a large grid interval. These calculations would require thousands of computational hours of simulation (for a one-dimensional system!).

In Fig. (3.2.2), we plot the flux-flux auto-correlation functions $C_{RR}(t)$ and $C_{RP}(t)$ as a function of time. The correlation functions almost fully decay over the considered time-interval at 500 K, as shown in Figs. (3.2.2a, b). This is no longer the case at the lower temperature of 80K, as shown in Figs. (3.2.2c, d). The differences between the two temperatures are due to the longer resonant oscillations of the correlation functions which are greater at low temperatures and by the presence of metastable states.From Fig. (3.2.2d),

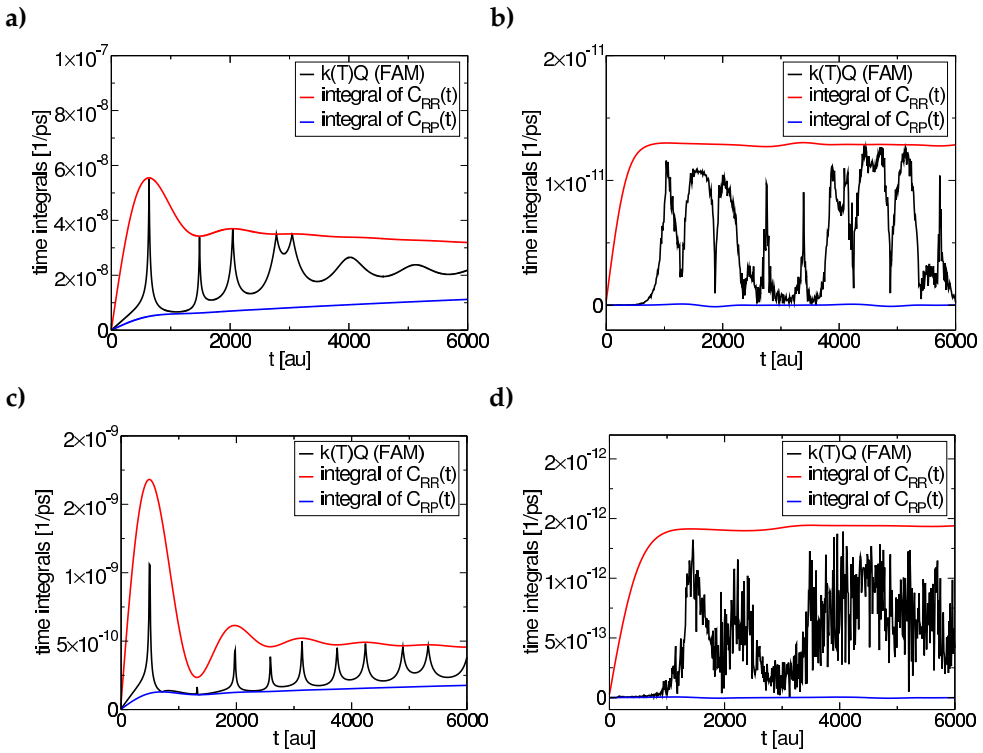

Figure 3.2.1: Plot of the time integrals $\int_0^t C_{RP}\,(t')\,dt'$, $\int_0^t C_{RR}\,(t')\,dt'$ and of the average value of thermal rate constant $\mathcal{Q}_{react}\,(T)\,k\,(T)$ in Eq. (3.1.1) as a function of time, for the Peskin (a, c) potential and the well separated double barrier potential (b, d). Temperatures for the top panel and bottom panel are respectively $T = 100$ K and $T = 80$ K. The DVR parameters are given in the text.

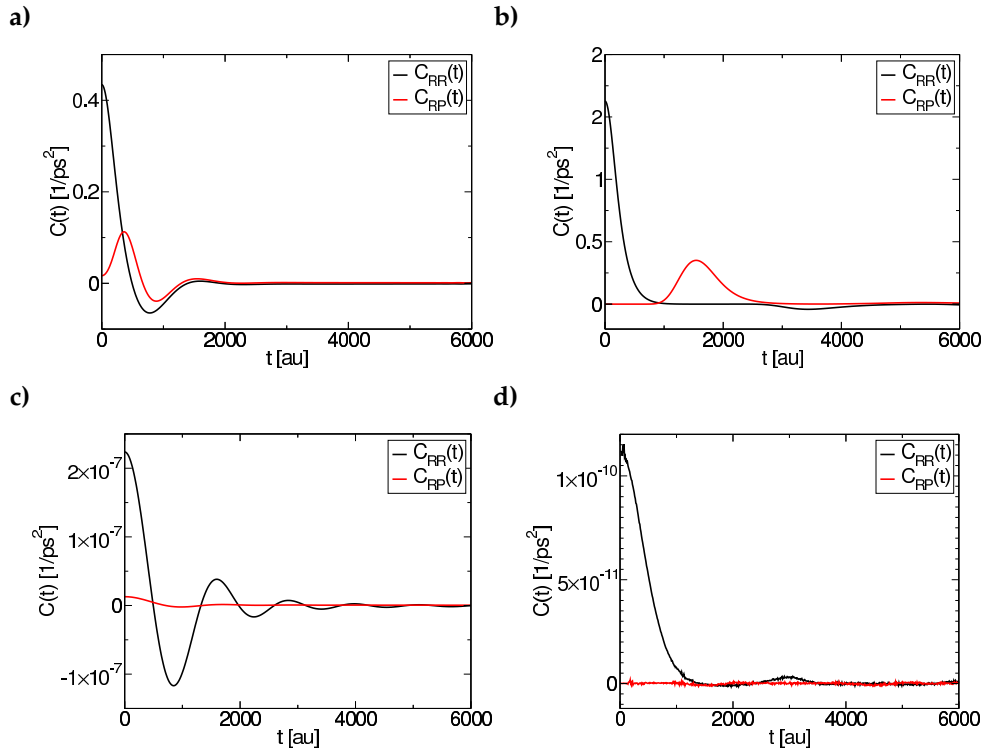

Figure 3.2.2: Plot of the flux-flux correlation functions $C_{RR}(t)$ and $C_{RP}(t)$ as a function of time, for the Peskin (a, c) potential and the well separated double barrier potential (b, d). Temperatures for the top panel and bottom panel are respectively $T = 500$ K and $T = 80$ K. The DVR parameters are given in the text.

it is evident that the flux-flux auto-correlation function time integration is not the same for the $C_{RR}$and the C_{RP} profile. This means that the total simulation time is not enough and that exponentially longer simulations should be performed. Then. it is also clear that as one goes to lower temperatures the calculations become very demanding from a computational point of view, requiring longer time propagation and larger memory to allocate the a larger grid. These problems which we have seen to arise in one dimensional potentials will get exponentially worse as one goes to higher dimensions. For these reasons, there has been a lot of interest in finding alternative methods to evaluate the rates. In the next Chapter we will describe switch from a time-dependent to a time-independent approach and we will develop a novel time-independent method.

CHAPTER 4

Numerical methods for the Time-Independent integration of the Schrödinger Equation

The main idea behind our calculations of the transmission probability $T(E)$ by numerical integration of the Schrödinger consists in finding asymptotic eigenfunctions $\psi_p(x)$ of the type

$$\hat{H}\psi_p(x) = \left[-\frac{\hbar^2}{2m}\frac{d^2}{dx^2} + V(x)\right]\psi_p(x) = E\psi_p(x) \tag{4.0.1}$$

using tools for solving ordinary differential equations (ODEs) at fixed eigenvalue E, with an appropriate choice of boundary conditions. [58, 59] When no information about the spectrum is known, pairs of eigenvalues and eigenfunctions of Eq. (4.0.1) must be computed at the same time using standard tools for solving eigen-problems. However, when eigenvalues are known *a priori* (for example, in the simple case of asymptotic free systems), eigenfunctions of Eq. (4.0.1) can be directly computed by solving Eq. (4.0.1) as an ODE, where the eigenvalues are treated as parameters. In this work, we consider scattering potentials with free particle asymptotic conditions (see Sec. 2.2.1 for details). When the potential is nonzero only in a closed scattering region $[-L_S, +L_S]$ and zero outside, eigenfunctions are plane waves with momentum p and energy $E = \frac{p^2}{2m}$ in the asymptotic limit $|x| \gg L_S$. Because no bound states exist for $E > 0$ (in this case, bound states are defined with energies $E < 0$ and they exist only if $V(x) < 0,\ x \in [-L_S, +L_S]$), we can divide the spectrum of Eq. (4.0.1) in two parts: a continuous spectrum for $E > 0$ and a discrete spectrum (if present) for $E < 0$. Recalling that only unbound states are relevant, in our scattering potential cases, for the computation of the transmission probability $T(E)$, we can focus our attention exclusively on the continuous spectrum, where the energy is $E > 0$ and it can be treated as continuous parameter in the ODE.

4.1 Log-Derivative Method

A very popular and efficient method to the presented ODE method is the log-derivative (LD) method, where a log-derivative transformation of Eq. (4.0.1) leads to a first-order differential equation (usually known as the Riccati equation). Theoretical chemistry community has employed mainly this method for scattering reactions rate and transmission probabilities. Calculations are most often restricted to few atom reactions, such as H+H2, D+H2, Cl+HCl, H+BrH, and more recently to OH+H2, OH+CO, OH+HCl, X+CH3X [60]. Because the numerical solution of the Riccati equation requires the propagation of only one boundary condition, the LD method is in principle faster than the ODE method.

The log-derivative (LD) method is a time-independent method alternative to the one presented and it is widely used for solving multi-dimensional scattering problems [61,62]. As for the ODE method, in the LD method the Schrödinger equation of Eq. (4.0.1) is solved by direct evolution of the boundary conditions. However, unlike the ODE method which directly solves the Schrödinger equation, in the LD method a log-trasformation of Eq. (4.0.1) is performed. Specifically, the Schrödinger equation

$$\frac{\partial_x^2 \psi(x)}{\psi(x)} + \mathcal{Q}(x) = 0, \tag{4.1.1}$$

where $\mathcal{Q}(x) = \frac{2m}{\hbar^2}\left(E - V(x)\right)$ and $V(x)$ is an arbitrary one-dimensional scattering potential in the region $x \in [-L,\, L]$, is written in the following way

$$\partial_x u(x) + u^2(x) + \mathcal{Q}(x) = 0, \tag{4.1.2}$$

by employing the transformation $u(x) = \partial_x \log \psi(x) = \frac{\partial_x \psi(x)}{\psi(x)}$. Eq. (4.1.2) is also known as Riccati's differential equation (RDE). The RDE is a first order differential equation and it requires only one boundary condition. Thus, the LD method should be faster than the ODE method, which instead is based on a second order differential equation. However, as shown below, the LD method is subject to pathological behavior at very low energies where the probability transmission is very small. For this reason, it is not suitable for computing thermal rate constants $k(T)$ either at low temperature or for resonant tunneling systems, where low energies states becomes dominant.

For an incoming wave function of the form $\psi(x_0) = \mathrm{e}^{ipx/\hbar}$, where $x_0 \ll -L_{\mathcal{S}}$ is an arbitrary starting point outside the scattering potential region, the RDE boundary condition becomes

$$u(x_0) = ip/\hbar. \tag{4.1.3}$$

For any large $\tilde{x} \gg L_{\mathcal{S}}$, $\psi(\tilde{x})$ has the form of an outgoing wave function and the solutions

of the RDE have the following asymptotic form

$$\begin{aligned} u(\tilde{x}) &= i\,k\frac{\sqrt{R}\,e^{ip\tilde{x}/\hbar}-e^{-ip\tilde{x}/\hbar}}{\sqrt{R}\,e^{ip\tilde{x}/\hbar}+e^{-ip\tilde{x}/\hbar}} \\ &= -k\,\frac{\sin(2p\tilde{x}/\hbar)+i\frac{1-R}{2\sqrt{R}}}{\cos(2p\tilde{x}/\hbar)+\frac{1+R}{2\sqrt{R}}}. \end{aligned} \tag{4.1.4}$$

where $p=\sqrt{2mE}$ and R is the reflection probability. By multiplication of both numerator and denominator of Eq. (4.1.4) by $R^{-1/4}$, we obtain

$$\begin{aligned} u\left(\tilde{x}\right) &= i\,k\frac{\sqrt{R}\,e^{ip\tilde{x}/\hbar}-e^{-ip\tilde{x}/\hbar}}{\sqrt{R}\,e^{ip\tilde{x}/\hbar}+e^{-ip\tilde{x}/\hbar}} \\ &= i\,k\frac{e^{ip\tilde{x}/\hbar+\frac{1}{4}\log R}-e^{-ip\tilde{x}/\hbar-\frac{1}{4}\log R}}{e^{ip\tilde{x}/\hbar+\frac{1}{4}\log R}+e^{-ip\tilde{x}/\hbar-\frac{1}{4}\log R}} = -k\frac{\sin\left(p\tilde{x}/\hbar-\frac{i}{4}\log R\right)}{\cos\left(p\tilde{x}/\hbar-\frac{i}{4}\log R\right)} \\ &= -k\frac{\sin\left(p\tilde{x}/\hbar\right)\cosh\left(\frac{1}{4}\log R\right)-i\cos\left(p\tilde{x}/\hbar\right)\sinh\left(\frac{1}{4}\log R\right)}{\cos\left(p\tilde{x}/\hbar\right)\cosh\left(\frac{1}{4}\log R\right)+i\sin\left(p\tilde{x}/\hbar\right)\sinh\left(\frac{1}{4}\log R\right)} = -k\frac{N}{D}, \end{aligned} \tag{4.1.5}$$

where in the last line we used the identities

$$\sin\left(ix\right) = i\sinh x, \tag{4.1.6a}$$

$$\cos\left(ix\right) = \cosh x. \tag{4.1.6b}$$

In order to express $u\left(\tilde{x}\right)$ in the form

$$u\left(\tilde{x}\right) = u_R\left(\tilde{x}\right) + iu_I\left(\tilde{x}\right), \tag{4.1.7}$$

we multiply both N and D in Eq. (4.1.5) by D^*, so that

$$\begin{aligned} ND^* &= \sin\left(p\tilde{x}/\hbar\right)\cos\left(p\tilde{x}/\hbar\right)\left[\cosh^2\left(\frac{1}{4}\log R\right)-\sinh^2\left(\frac{1}{4}\log R\right)\right] \\ &\quad - i\sinh\left(\frac{1}{4}\log R\right)\cosh\left(\frac{1}{4}\log R\right)\left[\cos^2\left(p\tilde{x}/\hbar\right)-\sin^2\left(p\tilde{x}/\hbar\right)\right] \\ &= \sin\left(p\tilde{x}/\hbar\right)\cos\left(p\tilde{x}/\hbar\right) - i\sinh\left(\frac{1}{4}\log R\right)\cosh\left(\frac{1}{4}\log R\right), \end{aligned} \tag{4.1.8}$$

and

$$DD^* = \cos^2\left(p\tilde{x}/\hbar\right)\cosh^2\left(\frac{1}{4}\log R\right)+\sin^2\left(p\tilde{x}/\hbar\right)\sinh^2\left(\frac{1}{4}\log R\right). \tag{4.1.9}$$

Recalling that

$$\sin x\,\cos x = \frac{1}{2}\sin\left(2x\right), \tag{4.1.10}$$

Eq. (4.1.5) becomes

$$\begin{aligned} u\left(\tilde{x}\right) &= -k\frac{ND^*}{DD^*} \\ &= -\frac{k}{2}\frac{\sin\left(\frac{2p\tilde{x}}{\hbar}\right) - i\sinh\left(\frac{\log R}{2}\right)}{\cos^2\left(\frac{p\tilde{x}}{\hbar}\right)\cosh^2\left(\frac{\log R}{4}\right) + \sin^2\left(\frac{p\tilde{x}}{\hbar}\right)\sinh^2\left(\frac{\log R}{4}\right)}. \end{aligned} \tag{4.1.11}$$

Finally, using the identities

$$\sin^2 x = \frac{1-\cos 2x}{2}, \tag{4.1.12a}$$

$$\cos^2 x = \frac{1+\cos 2x}{2}, \tag{4.1.12b}$$

and recalling that

$$\sinh\left(\frac{1}{2}\log R\right) = \frac{R^{\frac{1}{2}} - R^{-\frac{1}{2}}}{2} = -\frac{1-R}{2\sqrt{R}}, \tag{4.1.13a}$$

$$\cosh\left(\frac{1}{2}\log R\right) = \frac{R^{\frac{1}{2}} + R^{-\frac{1}{2}}}{2} = \frac{1+R}{2\sqrt{R}}, \tag{4.1.13b}$$

we obtain

$$u\left(\tilde{x}\right) = -k\frac{\sin\left(2p\tilde{x}/\hbar\right) + i\frac{1-R}{2\sqrt{R}}}{\cos\left(2p\tilde{x}/\hbar\right) + \frac{1+R}{2\sqrt{R}}}. \tag{4.1.14}$$

As expected, the asymptotic solutions of the RDE depend only on R. In particular, real and imaginary parts of $u(x)$ are strictly related since only one boundary condition can be fixed. From Eq. (4.1.4) we can compute the transmission T and reflection R probabilities as functions of the scattering energy E

$$R(E) = \left|\frac{k - i\,u(\tilde{x})}{k + i\,u(\tilde{x})}\right|^2, \tag{4.1.15a}$$

$$T(E) = 1 - R(E). \tag{4.1.15b}$$

At very low energy, the transmission probability tends to zero and the RDE asymptotic solutions given by Eq. (4.1.4) assumes the pathological form

$$u(\tilde{x}) \approx -k\,\frac{\sin(2p\tilde{x}/\hbar) + i\frac{T}{2}}{2\cos^2(p\tilde{x}/\hbar) + \frac{T^2}{8}}, \tag{4.1.16}$$

where very large deviations of order of T^2 appear for both the real and imaginary parts of $u(x)$. Consequently, a correct propagation of the boundary condition at x_0 requires an integration step which goes to zero as T^2. In particular, for T^2 smaller than the

machine precision, the LD method becomes numerically unfeasible. Moreover, the effect is pronounced for smoothly changing potentials where RDE solutions have the form of a outgoing wave functions for large regions, but with the incorrect value of R (see Fig. 4.2.1). It is important to observe that for the ODE method, the transmission probability T is only a multiplicative factor. Therefore, the propagation of the boundary conditions is numerically efficient at very low energies as well.

4.2 The Ordinary Differential Equation (ODE) method

The last step needed to solve Eq. (4.0.1) as an ODE consists in providing an appropriate choice of the boundary conditions. Because no absorbing barriers are present, the total energy must be conserved. Therefore, the following scattering representation

$$\psi_p(x) = \begin{cases} \mathrm{e}^{ipx/\hbar} & x \ll -L \\ \frac{t}{|t|^2}\,\mathrm{e}^{ipx/\hbar} + \frac{r}{|t|}\,\mathrm{e}^{-ipx/\hbar} & x \gg +L \end{cases} \tag{4.2.1}$$

can be obtained after using the following choice of boundary conditions

$$\psi_p(x_0) = 1 \tag{4.2.2a}$$

$$\partial_x \psi_p\left(x_0\right) = i\,p/\hbar. \tag{4.2.2b}$$

where $x_0 \ll -L_{\mathcal{S}}$ (see Sec. 2.2.1 for details). The pre-factors $\frac{t}{|t|^2}$ and $\frac{r}{|t|}$ in Eq. (4.2.1) are necessary in order to satisfy the continuity equation Eq. (2.2.6). Therefore, given an arbitrary point $\tilde{x}$ such that $\tilde{x} \gg L_{\mathcal{S}}$, we have

$$\psi_p\left(\tilde{x}\right) = \frac{t}{|t|^2}\,\mathrm{e}^{ip\tilde{x}/\hbar} + \frac{r}{|t|}\,\mathrm{e}^{-ip\tilde{x}/\hbar}, \tag{4.2.3a}$$

$$\partial_x \psi_p\left(\tilde{x}\right) = \frac{i\,p}{\hbar}\left(\frac{t}{|t|^2}\,\mathrm{e}^{ip\tilde{x}/\hbar} - \frac{r}{|t|}\,\mathrm{e}^{-ip\tilde{x}/\hbar}\right). \tag{4.2.3b}$$

Linear combinations of Eq. (4.2.3) gives

$$\psi_p\left(\tilde{x}\right) + \frac{\hbar}{i\,p}\partial_x \psi_p\left(\tilde{x}\right) = 2\frac{t}{|t|^2}\,\mathrm{e}^{ip\tilde{x}/\hbar}, \tag{4.2.4a}$$

$$\psi_p\left(\tilde{x}\right) - \frac{\hbar}{i\,p}\partial_x \psi_p\left(\tilde{x}\right) = 2\frac{r}{|t|}\,\mathrm{e}^{-ip\tilde{x}/\hbar}, \tag{4.2.4b}$$

whose complex modulo results

$$\left|\psi_p\left(\tilde{x}\right)+\frac{\hbar}{i\,p}\partial_x\psi_p\left(\tilde{x}\right)\right|^2 = 4\left|t\right|^2, \tag{4.2.5a}$$

$$\left|\psi_p\left(\tilde{x}\right)-\frac{\hbar}{i\,p}\partial_x\psi_p\left(\tilde{x}\right)\right|^2 = 4\frac{\left|r\right|^2}{\left|t\right|^2}=4\frac{\left|r\right|^2}{1-\left|r\right|^2}. \tag{4.2.5b}$$

Therefore, by inversion of Eqs. (4.2.5), transmission and reflection probabilities become

$$T(E)=\left|t\right|^2=4\left|\psi_p(\tilde{x})+\frac{\hbar}{i\,p}\partial_x\psi_p(\tilde{x})\right|^{-2}, \tag{4.2.6a}$$

$$R(E)=\left|r\right|^2=1-\left(1+\frac{1}{4}\left|\psi_p(\tilde{x})-\frac{\hbar}{i\,p}\partial_x\psi_p(\tilde{x})\right|^2\right)^{-1}. \tag{4.2.6b}$$

Although many other boundary conditions can be chosen, we used the boundary conditions in Eq. (4.2.2) in order to have a simple and computationally efficient expression of $T(E)$.

The method described above has many advantages. On one hand, we can find the thermal rate constant avoiding the time integration and using the transmission probability. On the other, we provide an efficient way to solve the Schrödinger equation in Eq. (4.0.1) using tools for solving ODEs as the Numerov's method or the Runge-Kutta method, avoiding the related eigenproblem which is numerically harder to tackle. Moreover, the time-independent ODE method is not as much memory demanding as the time-dependent approach (see Sec. 2.1) given that the calculation of the transmission probability $T\left(E\right)$ in Eq. (4.2.6) requires only the value of eigenstates for $\tilde{x}\gg L$, which can be obtained by propagation of the boundary condition without storing the entire eigenstate. Moreover, within the present method, the transmission probability can be sampled *ad hoc*, using a finer energy grid near resonant peaks. This is very important when dealing with the integration in Eq. (2.2.2) because, in the case of resonance states for double barrier potentials very narrow energy peaks are present. By using a fine grid only around resonant peaks and a coarse grid in flat regions, we have been able to reach numerically converged results for the energy integration in Eq. (2.2.2). Hereafter, we describe the methods currently employed for solving the Schrödinger equation in Eq. (4.0.1) and their numerical drawbacks.

4.2.1 Numerov's Method

The Numerov's method is a fourth-order multi-step method for solving one-dimensional differential equations of the second order [63]. Consider the following differential equation

$$\left(\frac{d^2}{dx^2} + f(x)\right)\psi(x) = 0, \tag{4.2.7}$$

where $f(x)$ is an arbitrary function and $\psi(x)$ is the eigenfunction. Let x_n be an arbitrary point: using the fifth order expansion of $\psi(x)$ around x_n we obtain

$$\psi_{n-1} - \psi_{n+1} = 2\psi_n + \Delta x^2 \psi_n'' + \frac{\Delta x^4}{12}\psi_n^{(IV)} + O\left(\Delta x^6\right). \tag{4.2.8}$$

where Δx is an appropriate discretization of the $x-$space and $x_{n\pm1} = x_n \pm \Delta x$. Here we use the notation $\psi_n = \psi(x_n)$ and $\psi_{n\pm1} = \psi(x_n \pm \Delta x)$. Using Eq. (4.2.7) in Eq. (4.2.8) for expanding $\psi''(x_n) = -f(x_n)\psi(x_n)$ and $\psi^{(IV)}(x_n) = -\frac{d^2}{dx^2}\left[f(x_n)\psi(x_n)\right]$, we obtain

$$\begin{aligned}\Delta x^2 f_n \psi_n &= 2\psi_n - \psi_{n-1} - \psi_{n+1} - \\ &\quad -\frac{\Delta x^2}{12}\left[f_{n-1}\psi_{n-1} - 2f_n\psi_n + f_{n+1}\psi_{n+1}\right] + O\left(\Delta x^6\right),\end{aligned} \tag{4.2.9}$$

where $f_n = f(x_n)$ and $f_{n\pm1} = f(x_n \pm \Delta x)$. Finally, solving Eq. (4.2.9) for ψ_{n+1} we obtain the Numerov's propagator

$$\psi_{n+1} = \frac{\left[2 - \frac{5\Delta x^2}{6} f_n\right]\psi_n - \left[1 + \frac{\Delta x^2}{12} f_{n-1}\right]\psi_{n-1}}{1 + \frac{\Delta x^2}{12} f_{n+1}}, \tag{4.2.10}$$

For the Schrödinger equation in Eq. (4.0.1), the Numerov's propagator in Eq. (4.2.10) assumes the form

$$\psi_{n+1} = \frac{\left[2 - \frac{5m\,\Delta x^2}{3\hbar^2}(E - V_n)\right]\psi_n - \left[1 + \frac{m\,\Delta x^2}{6\hbar^2}(E - V_{n-1})\right]\psi_{n-1}}{1 + \frac{m\,\Delta x^2}{6\hbar^2}(E - V_{n+1})}, \tag{4.2.11}$$

where $E = \frac{p^2}{2m}$, $V_n = V(x_n)$ and $V_{n\pm1} = V(x_n \pm \Delta x)$. For the Numerov's method, the boundary conditions assume the form

$$\psi(x_0) = 1, \tag{4.2.12a}$$

$$\psi(x_1) = \frac{i\,p}{\hbar}\Delta x + \psi(x_0) = \frac{i\,p}{\hbar}\Delta x + 1. \tag{4.2.12b}$$

For any fixed energy E, the computational complexity for computing the transmission probability $T(E)$ using the Numerov's method is $\mathcal{O}(N)$, where $N = \frac{L}{\Delta x}$. The main

contribution to the computational complexity is given by the propagation of the initial boundary condition in Eq. (4.2.12). Therefore, for computing $T(E)$ with an energy precision ΔE, the total computational complexity will be $\mathcal{O}(NM)$, where $M \approx \frac{V_0}{\Delta E}$ and V_0 is the maximum of the potential $V(x)$. Assuming that $M \approx \alpha N$, where α is an appropriate constant, we finally obtain $\mathcal{O}\left(\alpha N^2\right)$. However, the Numerov's method allows to compute $T(E)$ using a energy grid finer only where a high resolution is necessary, as near resonant peaks. Consequently, the proportionality constant α results to be very small and the Numerov's method shows a numerical speed-up respect to any time-dependent method.

4.2.2 Runge-Kutta method

The Runge-Kutta method is a fourth-order method for solving one-dimensional differential equations of the first-order [64]. Consider the following first order differential equation

$$\left(\frac{d}{dx} - f(x)\right)\psi(x) = 0, \tag{4.2.13}$$

where $f(x)$ is an arbitrary function and $\psi(x)$ is the eigenfunction. For a given step size Δx and arbitrary point x_n, we define

$$\psi(x_{n+1}) = \psi(x_n) + \frac{1}{6}(k_1 + 2k_2 + 2k_3 + k_4), \tag{4.2.14}$$

where k_i are defined as follows

$$k_1 = \Delta x\, f(x_n)\,\psi(x_n), \tag{4.2.15a}$$
$$k_2 = \Delta x\, f\left(x_n + \frac{1}{2}\Delta x\right)\left[\psi(x_n) + \frac{1}{2}k_1\right], \tag{4.2.15b}$$
$$k_3 = \Delta x\, f\left(x_n + \frac{1}{2}\Delta x\right)\left[\psi(x_n) + \frac{1}{2}k_2\right], \tag{4.2.15c}$$
$$k_4 = \Delta x\, f(x_n + \Delta x)\left[\psi(x_n) + k_3\right]. \tag{4.2.15d}$$

Intuitively, Eq. (4.2.14) is an averaged Taylor expansion where k_i represent

- k_1 is the increment based on the slope at the beginning of the interval, using $\psi(x_n)$.
- k_2 is the increment based on the slope at the midpoint of the interval, using $\psi(x_n) + \frac{1}{2}k_1$.
- k_3 is again the increment based on the slope at the midpoint, but now using $\psi(x_n) + \frac{1}{2}k_2$.
- k_4 is the increment based on the slope at the end of the interval, using $\psi(x_n) + k_3$.

Recalling that any differential equation of the second order of the type in Eq. (4.0.1) can be written as a system of first order differential equations of the form

$$\left(\frac{d}{dx} - F(x)\right)\Psi(x) = 0, \tag{4.2.16}$$

where

$$\Psi(x) = \begin{pmatrix} \psi(x) \\ \psi'(x) \end{pmatrix}, \tag{4.2.17a}$$

$$F(x) = \begin{pmatrix} \psi'(x) \\ \frac{2m}{\hbar^2}\left[E - V(x)\right] \end{pmatrix} = \begin{pmatrix} \psi'(x) \\ \frac{1}{\hbar^2}\left[p^2 - 2m\,V(x)\right] \end{pmatrix}, \tag{4.2.17b}$$

with the following boundary condition

$$\Psi(x_0) = \begin{pmatrix} 1 \\ i\,p/\hbar \end{pmatrix}, \tag{4.2.18}$$

it is possible to use the Runge-Kutta method for solving any Schrödinger equation with arbitrary one dimensional potentials.

Since the Runga-Kutta method differs from the Numerov's method presented in Sec. 4.2.1 only in the form of the boundary condition propagator, the computational complexity of the Runge-Kutta method will be $\mathcal{O}\left(\alpha' N^2\right)$, where α' is an appropriate constant which is typically smaller than one.

4.2.3 Generalization to Multichannel Scattering

All considerations and equations presented in the previous Sections can be generalized to the multichannel case, i.e. to non-adiabatic problem where electronic transitions are contemplated or vibro-rotational channels transitions. One need to solve the coupled-channel Schrodinger equation

$$\left(-\mathbf{1}\frac{\hbar}{2m}^2\frac{d^2}{dx^2} + \mathbf{V}(x) - \mathbf{E}\right)\mathbf{\Psi}(x) = 0 \tag{4.2.19}$$

where $\mathbf{1}$ is the $N \times N$ identity matrix and N is the number of coupled channels, $\mathbf{E}$ is the same dimensional parametric diagonal matrix and

$$\mathbf{V}(x) = \begin{pmatrix} V_{11}(x) & \dots & V_{1N}(x) \\ \vdots & \vdots & \vdots \\ V_{1N}(x) & \dots & V_{NN}(x) \end{pmatrix} \tag{4.2.20}$$

where the diagonal terms are the potential along each channel and the off-diagonal ones are the couplings terms between each channel. The potential matrix in Eq.(4.2.20) is of course symmetric. Finally the wavefunction

$$\mathbf{\Psi}(x) = \left(\psi^1(x), \ldots, \psi^N(x)\right) \tag{4.2.21}$$

is the vector composed of each channel function. The way to solve Eq. (4.2.19) according to the algorithm presented above is to solve the set of N coupled differential equations for each $\psi^i(x)$, by calculating the coupling terms in each equation using the set of previous step solutions for each channel. The initial boundary conditions for a typical scattering process can be

$$\begin{cases} \psi_p^i(x_0) &= 1 \\ \partial_x \psi^i(x_0) &= ip/\hbar \\ \psi_p^j(x_0) &= 0 \quad j = 1, \ldots, N \wedge j \neq i \\ \partial_x \psi^j(x_0) &= 0 \quad j = 1, \ldots, N \wedge j \neq i \end{cases} \tag{4.2.22}$$

where x_0 is the left asymptotic position and an initial wavepacket started from the i-th channel will propagate into all channels. Clearly the results depend on the choice of the parametric $\mathbf{E}$ diagonal matrix. According to the boundary conditions of Eq.s(4.2.22), the diagonal values for the initially empty channels are $E_j = V_{jj}(x_0)$ and that one of the i-th channel E_i is parametrically varied as in the mono-channel case.

4.2.4 Comparison of our ODE method with the Log-derivative method

In this Section, we will compare the ODE method presented in this thesis with the existing LD method. In particular, we will show that, unlike the ODE method, the LD method becomes numerically unstable in the deep tunneling region, even for a single barrier potential. We have chosen the single Eckart barrier as a case of comparison, because in this case the analytical results are known.

In Fig. (4.2.1) the comparison between the ODE method and the LD method is shown using a single Eckart barrier $V(x) = V_0/\cosh^2(\pi x/a)$, where $V_0 = 0.424$ eV and $a = 2.305$ a.u. (left) or $a = 5$ a.u. (right). As one can see Fig. (4.2.1d), the LD method gives the wrong result for the transmission probability at very low energy due to the pathological form in Eq. (4.1.16) for sufficiently wide potentials. This issue is further enhanced in case of resonant tunneling double barrier passage, where small energy resonant peaks integration is crucial for a correct description of the tunneling. For these reasons, we have chosen to not adopt the LD methods on our resonant tunneling calculations.

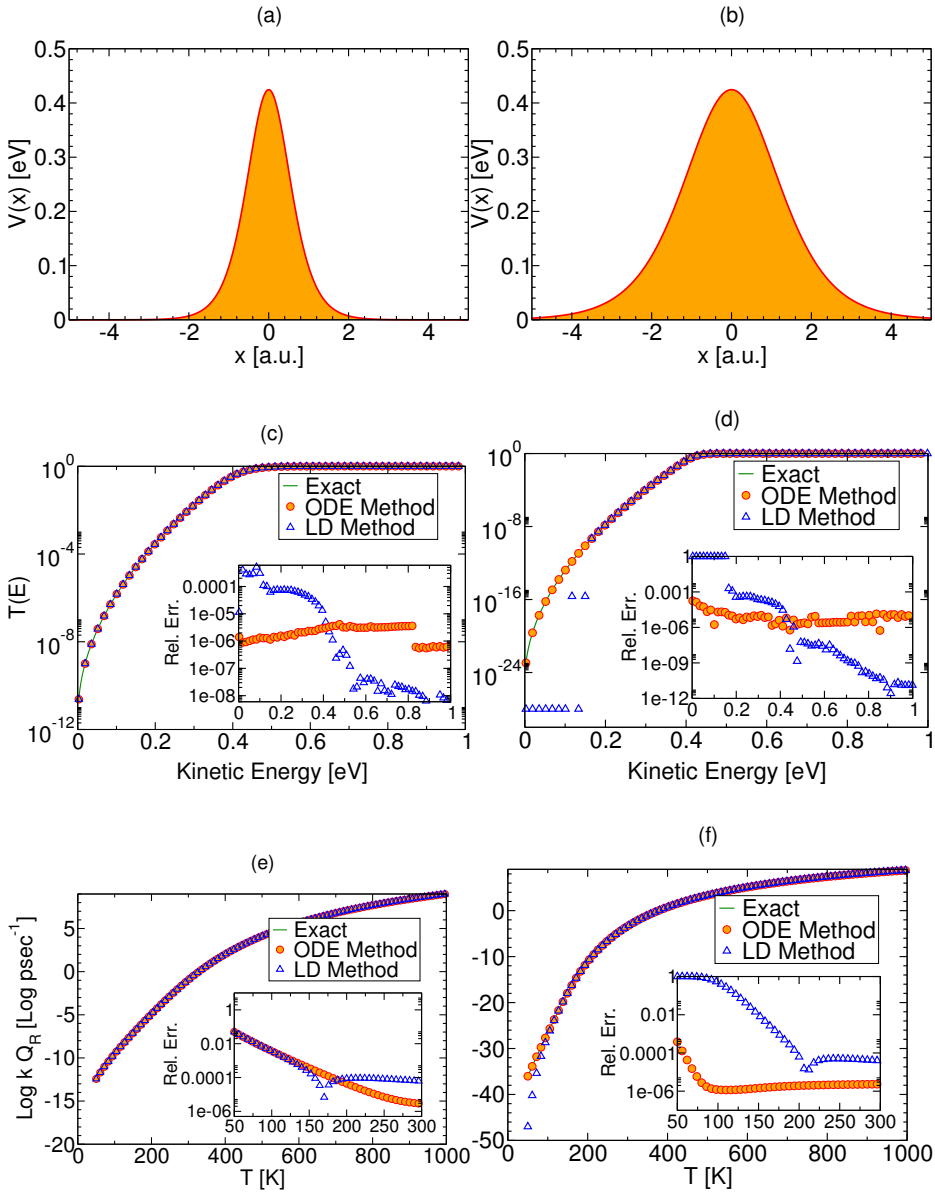

Figure 4.2.1: Thermal rate constant for a single Eckart barrier potential with width $a = 2.305$ a.u. (left) and $a = 5$ a.u. (right). Panels a) and b): The potential profiles. Panels c) and d): Comparison between the exact (solid) transmission probability $T(E)$ and our numerical results using the ODE method (dots) and the LD method (triangles up). Panels e) and f): Comparison between the exact (solid) thermal rate constant $k\,Q_r$ and our numerical results using the ODE method (dots) and the LD method (triangles up). In the insets, the relative error $\left|\frac{(k\,Q_R)_{\rm ODE}-(k\,Q_R)_{\rm exact}}{(k\,Q_R)_{\rm exact}}\right|$ is reported.

CHAPTER 5

ODE Method Results

In this Chapter we will test our ODE method using different potentials. In the first two examples, Sec. 5.1 and 5.2, we will compare the ODE method using the well known Eckart potential where an analytical expression for the transmission probability $T(E)$ is provided. Finally, as a more challenging test, Sec. 5.3 and 5.4 will be dedicated to test our ODE method for a potential with two distinct separated barriers. In particular, we will show that our ODE method can deal with extreme potential with many quasi-resonant states, even in the deep resonant regime at very low temperature.

5.1 Single Eckart Barrier

The typical textbook example for testing tunneling rate methods is the Eckart potential. A particle of $m = 1.060 \times 10^3$ a.u. is scattered against an Eckart barrier

$$V(x) = \frac{V_0}{\cosh^2(\pi x/a)}, \tag{5.1.1}$$

where $V_0 = 0.424$ eV and $a = 2.305$ a.u. The potential profile is reported in the top panel in Fig. (5.1.1). Since for the single Eckart barrier potential in Eq. (5.1.1), the probability transmission $T(E)$ can be exactly computed [17]

$$T_{exact}(E) = \frac{\cosh\left(\sqrt{\frac{8m\,E\,a^2}{\hbar}}\right) - 1}{\cosh\left(\sqrt{\frac{8m\,E\,a^2}{\hbar}}\right) + \cosh\left(\sqrt{\frac{8m\,V_0\,a^2}{\hbar} - \pi^2}\right)}, \tag{5.1.2}$$

it is possible to directly test the ODE method and to determine its precision. In Fig. (5.1.1), the central panel shows the comparison between the exact transmission probability $T_{exact}(E)$ in Eq. (5.1.2) and the transmission probability $T_{ODE}(E)$ computed with the ODE method. In order to better appreciate the difference between the exact (continuous

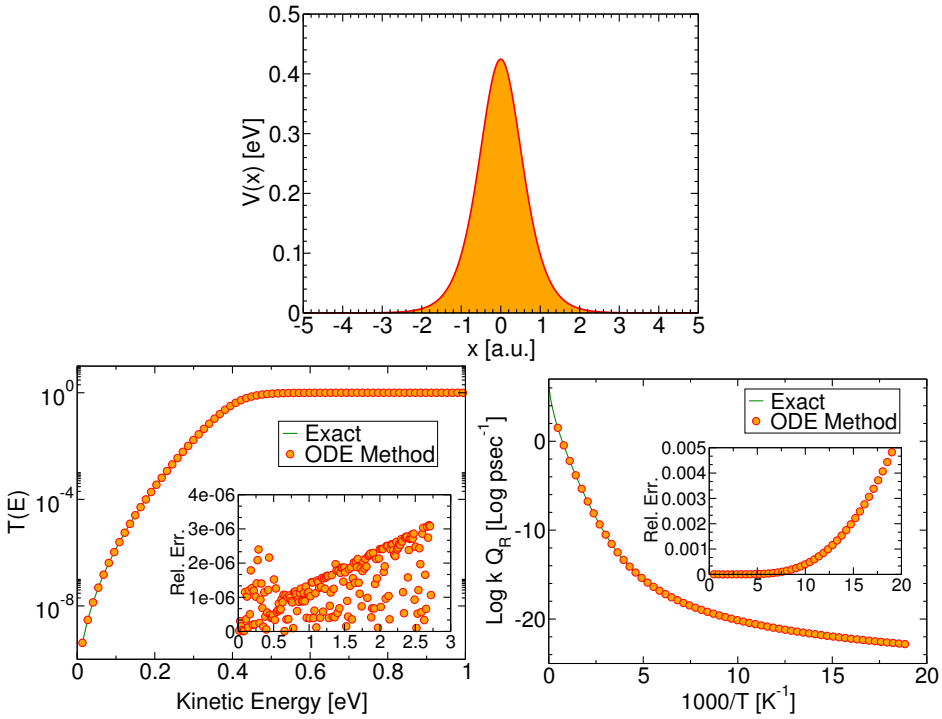

Figure 5.1.1: Thermal rate constant for a single Eckart barrier potential. (Top panel) The potential profile. (Middle panel) Comparison between the exact (solid) transmission probability $T(E)$ and our numerical results using the ODE method (dots). As reported in the inset, the relative error $\left|\frac{T_{\rm ODE}(E)-T_{\rm exact}(E)}{T_{\rm exact}(E)}\right|$ is smaller than 3×10^{-6}. (Lower panel) Comparison between the exact (solid) thermal rate constant $k\,Q_r$ and our numerical results using the ODE method (dots). In the inset, the relative error $\left|\frac{(k\,Q_{react})_{\rm ODE}-(k\,Q_{react})_{\rm exact}}{(k\,Q_{react})_{\rm exact}}\right|$ is shown.

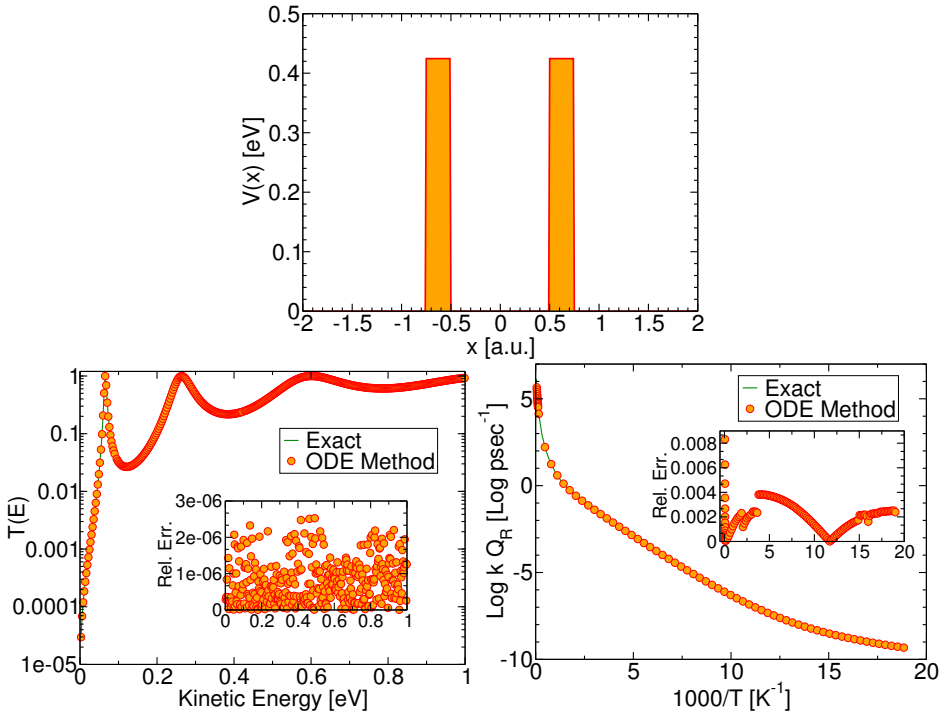

Figure 5.2.1: Thermal rate constant for a double rectangular barrier potential. (Top panel) The potential profile. (Middle panel) Comparison between the exact (solid) transmission probability $T(E)$ and our numerical results using the ODE method (dots). As reported in the inset, the relative error $\left|\frac{T_{\rm ODE}(E)-T_{\rm exact}(E)}{T_{\rm exact}(E)}\right|$ is smaller than 3×10^{-6}. (Lower panel) Comparison between the exact (solid) thermal rate constant $k\,Q_r$ and our numerical results using the ODE method (dots). In the inset, the relative error $\left|\frac{(k\,Q_R)_{\rm ODE}-(k\,Q_R)_{\rm exact}}{(k\,Q_R)_{\rm exact}}\right|$ is shown.

line) and the calculated (dots) values, the relative error is reported in the inset. This shows that the percentage error is always smaller than $0.03\,\%$. The values of $k(T)\cdot Q_{react}$ are reported in the bottom panel and there is almost no deviation from the analytical results even at very low temperatures. For example at $T = 60$ K the percentage error is smaller than half a percent.

5.2 Double Rectangular Barrier

The main goal of this thesis is to look at resonance barrier scattering rate constants. In order to test the method in the case of an analytical example, we have chosen the double rectangular barrier, whose profile is reported in the top panel of Fig. (5.2.1). The particle's mass and the potential maximum value are the same as for the Eckart barrier calculation in Sec. 5.1, that is $m = 1.060\times10^3$ a.u. and $V_0 = 0.424$ eV. The rectangular barriers width

has been set equal to $\Delta = 0.25$ a.u. and the gap between the barriers equal to $\delta = 1$ a.u.

$$V(x) = V_0 \left[\chi_{[-\delta-\Delta,\,-\Delta]}(x) + \chi_{[\Delta,\,\Delta+\delta]}(x) \right], \tag{5.2.1}$$

where $\chi_{[a,\,b]}(x)$ is the characteristic function which is equal to one in the region $x \in [a,\,b]$ and zero otherwise. As in the case of the single Eckart barrier, for the double rectangular potential in Eq. (5.2.1), the exact transmission probability has the form

$$T_{exact}(E) = \frac{2^8\, E^2\, (V_0 - E)^2}{V_0^4\, |K(E)|^2}, \tag{5.2.2}$$

where

$$\begin{aligned} K(E) &= e^{-2[\delta\,\chi(E) + i(\Delta\,k(E) + 2\phi(E))]}\,. \\ &\quad \cdot \left[\left(-1 + e^{2\delta\,\chi(E) + 4i\,\phi(E)} \right)^2 - \left(e^{2\delta\,\chi(E)} - 1 \right)^2 e^{4i(\Delta\,k(E) + \phi(E))} \right] \end{aligned} \tag{5.2.3}$$

and

$$k(E) = \frac{\sqrt{2m\,E}}{\hbar}, \tag{5.2.4a}$$

$$\chi(E) = \frac{\sqrt{2m\,(V_0 - E)}}{\hbar}, \tag{5.2.4b}$$

$$\phi(E) = \arctan\left(\frac{\chi(E)}{k(E)} \right). \tag{5.2.4c}$$

As shown in the middle panel of Fig. (5.2.1), three quasi-bound states can clearly be distinguished from the $T(E)$ profile. Despite the discontinuity of the first derivative of the double rectangular barrier potential, the numerical solution is in accordance with the analytical result for the entire energy range, as in the case of the Eckart potential. The same considerations can be made for the bottom panel, where the thermal rate constant is reported.

5.3 Peskin's Potential

In this Section, we considered a well known double Eckart barrier potential with a single quasi-bound state [32]. In particular, we will show that time-dependent methods as the FAM fails in the calculation of thermal rate constants. Following Peskin et al. [32], the mass of the scattering particle is set to $m = 1.834 \times 10^3$ a.u. and the potential energy function is

$$V(x) = V_0 \left(\frac{1}{\cosh^2(x)} - \frac{1}{\cosh^2(a\,x)} \right), \tag{5.3.1}$$

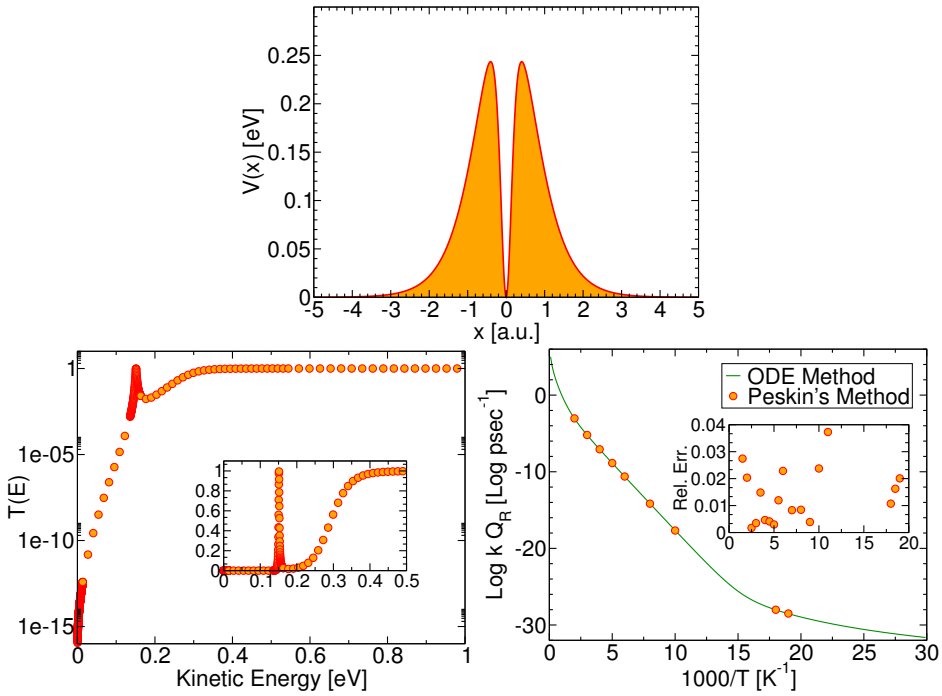

Figure 5.3.1: Thermal rate constant for a double barrier potential, Eq. (5.3.1). (Top panel) The potential profile. (Middle panel) Transmission probability $T(E)$ calculated using the ODE method (log-lin scale for the main figure and lin-lin scale for the inset). (Lower panel) Comparison between the thermal rate constant $k\,Q_r$ computed using our numerical method (solid) and the FAM method (dots). In the inset, the relative error $\left|\frac{(k\,Q_R)_{\rm ODE}-(k\,Q_R)_{\rm FAM}}{(k\,Q_R)_{\rm FAM}}\right|$ is shown. The deviation between the two numerical methods is contained within $4\,\%$.

where $V_0 = 0.310$ eV and $a = 5$ a.u. The potential profile is reported in the top panel of Fig. (5.3.1). The potential gap is such that there is a single quasi-bound state, as shown in the middle panel where there is a single transmission probability resonance peak. To use the FAM formulation of the thermal rate of Eq. (1.3.10), we calculate the flux auto-correlation functions $C_{R,R}\,(t)$ and $C_{R,P}\,(t)$ using a sinc-DVR grid method [65] (see App. A for more details). As an example, the value and the profile of Eq. (1.3.10) versus the truncation times at $T = 125$ K are reported in Fig. (5.3.2). These are in close agreement with the time-independent method presented here and reported on the same figure as a horizontal dashed line. The complete set of thermal rate constant results are reported on the bottom panel of Fig. (5.3.1). In particular, the inset reveals that the agreement between the FAM method and the present is within $4\,\%$ down to 50 K.

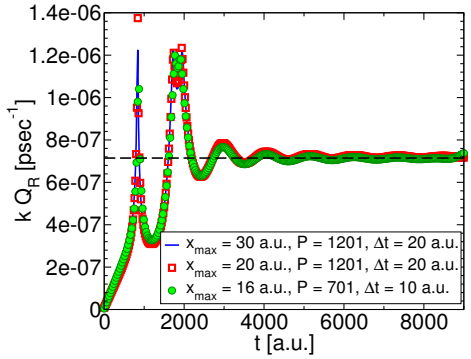

Figure 5.3.2: Thermal rate constant as a function of the truncation time t_0 obtained using the FAM method of Eq. (1.3.10) at $T = 125$ K and for the potential of Eq. (5.3.1). The dotted line is the value of $k\,Q_r$ obtained using our ODE method. $x_{\max}$ denotes the DVR grid extension, P the number of points and Δt the time increment in the time-dependent simulation.

5.4 Double Barrier Potential

As a final and even more challenging test, we considered a potential with two Eckart barriers separated by a wide gap, Fig. (5.4.1). In this case, a large number of low-energy quasi-bound states are present. As in the third example, the particle's mass is set to $m = 1.834 \times 10^3$ a.u. and the potential equation is

$$V(x) = V_0 \left(\frac{1}{\cosh^2(x-a)} + \frac{1}{\cosh^2(x+a)} - \frac{2}{\cosh^2(a)\cosh^2(x)} \right) \tag{5.4.1}$$

where $V_0 = 0.310$ eV and $a = 2$ a.u. The potential profile is shown in the top panel of Fig. (5.4.1) and the transmission probability in the middle one. This potential represents a real challenge for a numerical method for calculating thermal rate constants, because several resonance peaks are present in the transmission probability and a wider logarithmic range has to be taken in order to describe all rates in the presence of resonances. In the inset of the middle panel plot of Fig. (5.4.1) the transmission probability is reported in linear scale. With this plotting choice, resonance peaks are even more evident. When carrying out the energy integration of Eq. (2.2.2) in presence of many low-energy quasi-bound states, one needs to be very careful in choosing the integration grid set-up around the resonance peaks. With the method labeled "ODE method" in Fig. (5.4.1) the grid density has been properly enhanced around the resonance peaks. With the method labeled "ODE method + BW Correction", a Breit-Wigner distribution is used to fit the resonance peaks of the transmission probability, in order to have a better integration of $T\,(E)$ and overcome the numerical limitation of having a very dense grid near peaks. More specifically, the

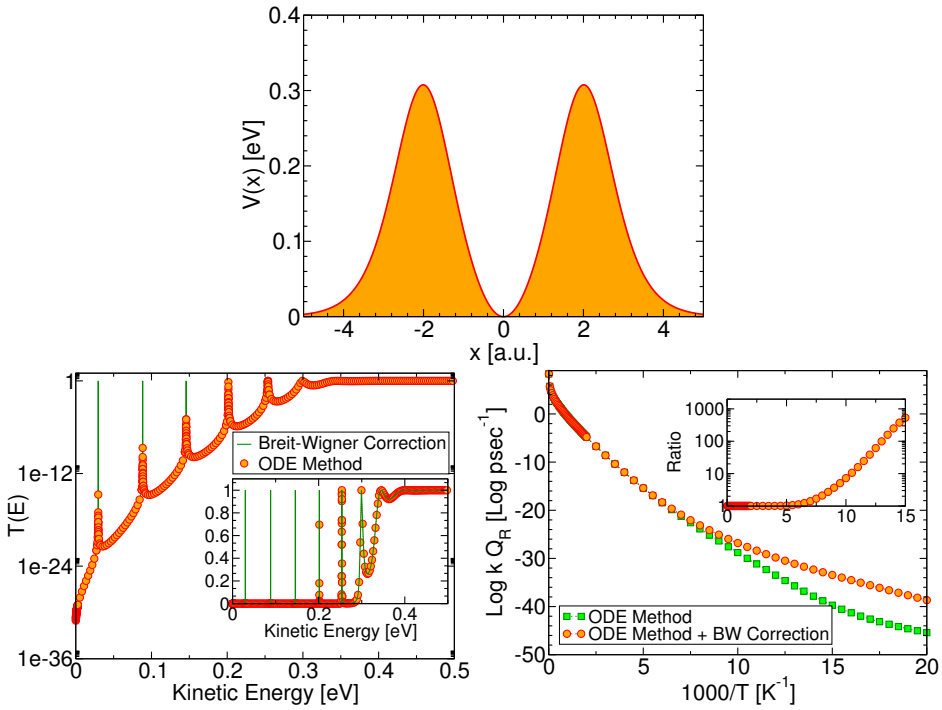

Figure 5.4.1: Thermal rate constant for a double Eckart barrier potential, Eq. (5.4.1). (Top panel) The potential profile. (Middle panel) Transmission probability $T(E)$ computed using our ODE method with (solid) and without (dots) the Breit-Wigner correction (log-lin scale for the main figure and lin-lin scale for the inset). (Lower panel) Comparison between thermal rate constants computed using the ODE method with (circles) and without (squares) the Breit-Wigner correction. In the inset, the ratio $\left|\frac{(k\,Q_R)_{\mathrm{ODE+BW}}}{(k\,Q_R)_{\mathrm{ODE}}}\right|$ is shown.

Table 5.1: Breit-Wigner distribution parameters for Eq. 5.4.2 employed for the double Eckart potential rate calculation ($\omega_0 = 27.211$ eV).

Peak	E_r/ω_0	Γ_r/ω_0
I	$1.090 \cdot 10^{-3}$	$2.936 \cdot 10^{-15}$
II	$3.247 \cdot 10^{-3}$	$9.540 \cdot 10^{-12}$
III	$5.358 \cdot 10^{-3}$	$3.280 \cdot 10^{-9}$
IV	$7.408 \cdot 10^{-3}$	$2.664 \cdot 10^{-7}$
V	$9.326 \cdot 10^{-3}$	$1.648 \cdot 10^{-5}$

narrow peaks are well approximated by the Breit-Wigner (BW) approximation

$$T_r(E) \approx \frac{\left(\Gamma_r/2\right)^2}{\left(E - E_r\right)^2 + \left(\Gamma_r/2\right)^2}, \tag{5.4.2}$$

where E_r and Γ_r are respectively the resonance energy and the width of the resonant peak. A JWKB (Jeffreys-Wenzel-Brillouin-Kramer) [66–69] derivation of the BW distribution for these resonance peaks is given in App. B. Consequently, we corrected our "ODE method" using an analytical expression for the transmission probability at the center of the narrowest peaks. Differences between the two approaches can be appreciated only at very low temperatures, namely below $T = 200$ K. At these temperatures, the BW fitting resulted to be necessary in order to have an accurate thermal rate constant value. In Tab. (5.1), we report values of E_r and Γ_r (starting from the lowest in energy peak) obtained fitting Eq. (5.4.2) near each peak.

5.4.1 Importance of the Resonant Peaks for the Calculation of the Thermal Rate Constant in the Deep Resonant Tunneling Regime

In general, the thermal rate constant $k\left(T\right)$ in Eq. (2.2.2) can be written as the sum of a singular part (resonant contribution) and a non-singular part

$$k\left(T\right) Q_R\left(T\right) = \frac{1}{2\pi\hbar} \sum_{i=1}^{n_p} \int_{E_i-\Delta}^{E_i+\Delta} e^{-\beta E} N_i\left(E\right) dE \tag{5.4.3a}$$

$$+ \frac{1}{2\pi\hbar} \int_0^{+\infty} e^{-\beta E} N_{\mathrm{NR}}\left(E\right) dE, \tag{5.4.3b}$$

where n_p is the number of resonant peaks. In Eqs. (5.4.3), $N_i(E)$ and $N_{\mathrm{NR}}(E)$ are respectively the cumulative transmission probabilities in proximity of the $i-th$ resonance peak and outside singular regions, and Δ is supposed to be small enough to allow for a clear separation of each resonance peak. In the case of symmetric double barriers, the trans-

mission probability $N_i(E)$ for energies close to a resonance peak is well approximated by Eq. (5.4.2) as shown in App. B. For sufficiently small width Γ_i, $N_i(E)$ can be further approximated, for analytical integration purposes, by [30]

$$N_i(E) = \frac{(\Gamma_i/2)^2}{(E-E_i)^2 + (\Gamma_i/2)^2} \approx \frac{\pi\Gamma_i}{2}\delta(E-E_i). \tag{5.4.4}$$

Using Eq. (5.4.4), we obtain an estimate of the resonant contribution to the thermal rate constant as

$$k_{\text{res}}(T)\, Q_{react}(T) \approx \frac{1}{2\pi\hbar}\frac{\pi}{2}\sum_{i=1}^{N_P}\Gamma_i\, e^{-\beta E_i}, \tag{5.4.5}$$

which depends directly on each finite width Γ_i and resonant energy E_i.

Because the resonant part in Eq. (5.4.5) is a sum of exponentials, $k_{\text{res}}(T)\, Q_R(T)$ will be dominated by those peaks i^* for which $E_{i^*} \approx \frac{1}{\beta} = k_B T$ and then

$$\log\left[k(T)\, Q_{react}(T)\right] \approx -\beta\, E_{i^*} + A(\beta), \tag{5.4.6}$$

where $A(\beta)$ is a slowly changing function which contains the contribution of the non-resonant part in Eq. (5.4.3b). Therefore, as a consequence of the resonant tunneling, the interplay between the resonant peak weights induces, as the temperature is lowered, a clear variation of the slope in a log-lin plot of the thermal rate constant $k(T)$. It is important to observe that this phenomenon is completely absent in non-resonant potentials where in deep tunneling regime the logarithm of the thermal rate is constant.

For this reason, it is necessary to include all resonant peaks in the transmission probability integration when resonant potentials are considered. In this direction, we performed some numerical tests by artificially removing the lower energy peaks and we have found the thermal rate to change drastically, even if the Boltzmann weight reduces the contribution coming from the lower energy peaks.

CHAPTER 6

Helium Isotopes Selection by Resonant Tunneling in a Double Layer Polyphenylene System

In the previous Chapter, we showed that the ODE method, as described in Chaps. (4) and (5), can successfully be used to compute thermal rate constants $k(T)$, even in the deep resonant tunneling regime at low temperature. In this Chapter, we will describe how resonant tunneling can be used to select species with different masses. In particular, in this Chapter we considered the selection of Helium isotopes.

6.1 Potential Energy Surface construction by ab initio methods[1]

Two stable isotopes of helium exist. On earth, the predominant isotope is ^{4}He, which is produced as uranium alpha-decays to lead. Very low concentrations of ^{3}He can be found in various terrestrial sources (remaining from the accretion of the earth) and lunar regolith (deposited by solar wind), but currently the only viable source is from the decay of tritium, as a byproduct of nuclear weapons stockpile. [70] The dwindling supply of ^{3}He, combined with growing use for neutron-detection sensors, and to a lesser extent basic research and oil and petroleum and natural gas exploration, has raised concerns over the long-term supply of this isotope. [71] A vast quantity of ^{3}He could potentially be separated from existing helium stockpiles, natural gas, or the atmosphere, but the energy costs of performing the separation make these exceedingly impractical with current cryogenic distillation methods. [72]

Membrane-based methods of gas separation are potentially more efficient because they avoid the energy cost of liquefying the gases necessary for cryogenic distillation. [73] Several groups [74,75] have examined the use of two-dimensional polyphenylene (2D-PP) shown in Fig. (6.1.1), a nanoporous analogue of graphene synthesized by Bieri [76], for

[1] In collaboration with A. M. Brockway and J. Schrier, Department of Chemistry, Haverford College, Haverford (PA), USA.

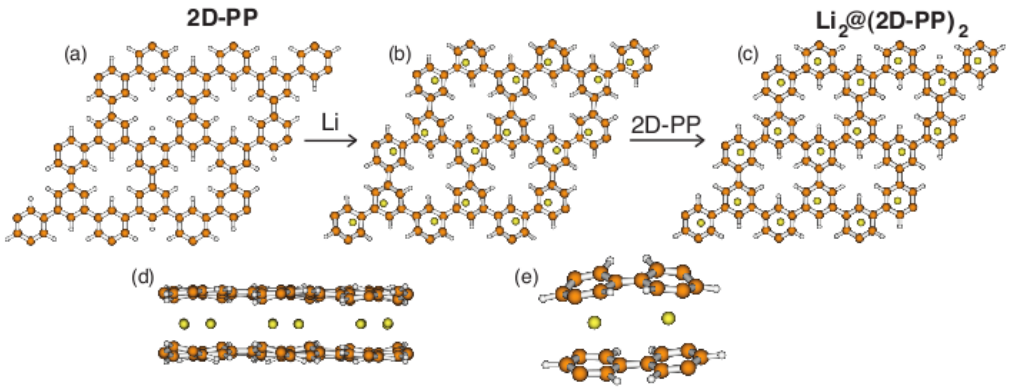

Figure 6.1.1: PM6-D2 optimized geometries, with carbon, hydrogen, and lithium atoms depicted in orange, white, and yellow. (a) Two-dimensional polyphenylene (2D-PP); (b) 2D-PP with a monolayer of lithium atoms; (d) Lithiated 2D-PP bilayer (Li_2@(2D-PP)$_2$); (e) Side view of Li_2@(2D-PP)$_2$; (f) Close up view of a single unit cell of Li_2@(2D-PP)$_2$.

separating helium from natural gas and air. The small size of the 2D-PP pores allows helium atoms (and hydrogen molecules [77]) to pass through, but rejects the passage of larger molecules, even at high temperatures. Because 2D-PP is only one atom thick, and the mass of helium atoms is not too large, quantum tunneling plays a significant role in the transmission of helium atoms, even at room temperature. [74] The mass-dependence of tunneling provides a potential means of separating the two isotopes which would not be possible classically. [78] Because the concentrations of ^{3}He are so low, it is important to have a very high selectivity for the transmission of this isotope if one is to create a practical process. Unfortunately, 2D-PP has low ^{3}He selectivity at temperatures where the flux rate is high, and higher selectivities only occur at low temperatures where the flux rate is impractically small. [74] Very recently, Hauser and Schwerdtfeger have proposed nitrogen-functionalized pores in graphene as a way of achieving both high flux and high selectivity. [79] Their highest selectivity of 19, is achieved only at 10 K, and rapidly approaches 1 (no selectivity) by 25 K. They estimate that even at the lowest temperature, the flux rate is about 10^{-9} moles cm^{-2} s^{-1} under a feed pressure of 1 bar. Our goal is to develop nanostructures with higher selectivity and flux rate, capable of operating at higher temperatures, which will further lower the cost of obtaining ^{3}He from natural sources.

All previous studies of helium isotope separation by tunneling have used a single-barrier device. [74,78,79] Here we propose resonant tunneling through a double-barrier nanostructure constructed from organometallically joining two 2D-PP layers with lithium atoms (see Figs. (6.1.1c-d)). In resonant tunneling, complete transmission occurs when the incoming particles have kinetic energies matching the quasi-bound states of the potential

well formed by the double-barrier. These resonant transmissions occur much lower than the barrier height; thus even when the temperature is such that very few atoms have sufficient kinetic energy to classically pass over the potential energy barrier, the transmission can be quite high due to these resonant peaks. Thus, quantum mechanics allows in some cases that the atoms will be more likely to be transmitted through the double-barrier structure than through a single barrier at low temperatures, providing a way to increase the flux rate through the system. Because the energies of the quasi-bound states (and thus the resonant transmissions) are inversely dependent on the particle mass (e.g., consider the eigenstates of the quantum particle in a 1D-box problem), resonant transmissions of ^{4}He atoms occurs at higher energies than those of the ^{3}He atoms. This provides a means of separating the two isotopes. What we propose here is *not to be confused* with the resonant tunneling of electrons within the π-bands of a graphene sheet where the potential has been modulated to form a double barrier, studied by Pereira *et al*. [80] Rather, we propose transmission of a helium atom through two aligned pores of two nanoporous graphene sheets; the double-barrier arises due to the nature of the potential energy surface for performing this atom transmission. From a fundamental perspective, this extends a basic quantum mechanical phenomenon to heavy atoms. From the perspective of chemical engineering, this is both the first application of resonant tunneling to separations, and makes a significant improvement to the helium isotope separation problem discussed above.

How are we to construct a double-barrier nanostructure? A simple bilayer of 2D-PP will not work. The $\pi - \pi$ stacking interaction between benzene rings favors a parallel-displaced arrangement, [81] resulting in an offset stacking analogous to the Bernal stacking of graphene bilayers. Consequently, this will occlude the pores, preventing atom transmission. The only way to avoid occluding the pores is to aligning the benzene rings atop each other. Density functional theory (DFT) calculations indicate that many alkali metal and transition metal atoms selectively bind to above the benzene rings in 2D-PP, leaving the pores open for atom transmission. [82, 83] Additionally, these calculations show that forming a disperse layer of isolated atoms on the 2D-PP surface is energetically more favorable than forming multi-atom clusters. For example, a small amount of Li atoms deposited on the 2D-PP surface will distribute themselves to form a single-atom monolayer rather than forming clusters, as shown in Fig. (6.1.1b). Because the 2D-PP unit cell consists of two benzene rings, two lithium atoms per unit cell are needed for stoichiometric coverage. When a second layer of 2D-PP is placed on top, the Li atoms that are already bound to the center of the benzene rings of the bottom 2D-PP will prefer to also bind to the center of the benzene rings in the top 2D-PP sheet, as shown in Figs. (6.1.1c,d). This is analogous to the well-known organometallic double- and multi-layer "sandwich"

compounds. [84–86] Though we will only consider Li atoms here, other metal atoms (e.g., V, Sc, Ti) also have the same behavior on 2D-PP, [83] which can provide a means of tuning the interlayer separation between the two 2D-PP sheets.

Single-barrier porous graphene coordinates were constructed with C-C bond lengths of 1.421 Å and C-H bond lengths of 1.070 Å, forming a 3x3 supercell (Fig. (6.1.1a)). Lithium atoms were placed between two such porous graphene sheets, and the atom coordinates and supercell lattice constants were optimized using PM6-D2 [87,88] semi-empirical Hartree-Fock theory with empirical dispersion correction terms, using MOPAC 2009, v11.053L [89]. These calculations imposed two-dimensional periodic boundary conditions, and only sample the Γ-point in the Brillouin zone; the same k-point sampling and 3x3 supercell (shown in Figs. (6.1.1c,d)) was used in the DFT calculations of 2D-PP by Blankenburg *et al*. [75]

To establish the validity of the PM6-D2 geometry, we also performed a benchmark calculation examining Li adsorption on a series of 6-24 carbon polyaromatic hydrocarbon (PAH) molecules, and compared to the results of Baker and Head-Gordon. [90] They found that density functional theory (DFT) favors ionic configuration by about 0.5 eV and Hartree-Fock (HF) favors non-ionic configurations by about 0.5 eV, compared to coupled-cluster-single-doubles (CCSD) and O2-theory results which are taken to be authoritative. Both DFT and HF theories give comparable Li-PAH distances of 2.36–6.48 Å for nonionic configurations, and distances of 1.70–1.88 Å for ionic configurations. In contrast, the post-HF O2 and CCSD methods give a state which combines ionic and non-ionic configurations, and has Li-PAH distances of 2.25–2.97 Å. Our PM6-D2 calculations found Li-PAH distances of 2.04–2.30 Å, suggesting that the semiempirical parameterization of this HF-type method accounts for a portion of the systematic error seen in the ab initio HF (and DFT) methods.

To obtain the potential energy surface (PES), DFT calculations with ABINIT 6.4.1, [91] using the Perdew-Burke-Ernzerhof (PBE) generalized gradient exchange correlation functional, norm-conserving Trollier-Martins pseudopotentials, and a planewave energy cutoff of 50 Rydberg. A 16 Å vacuum region was added above and below the two 2D-PP sheets, and like the geometry calculations, and only the Γ-point in the Brillouin zone was used for these calculations. Empirical dispersion corrections were computed with `dftd3`, [92] V2.1 Rev.1 using the D2, [93] D3, [94] and D3(BJ) [95] methods of Grimme and co-workers. The inclusion of the dispersion correction has two effects on the PES: (i) lowering the barrier height maxima; and (ii) introducing potential wells above/below the 2D-PP sheet. To establish the validity of the dispersion-corrected DFT PES, one can see a comparison of PES of He passing through a single 2D-PP barrier obtained from these theories to the corresponding MP2/cc-pVTZ PES from Ref. [74]. Uncorrected PBE

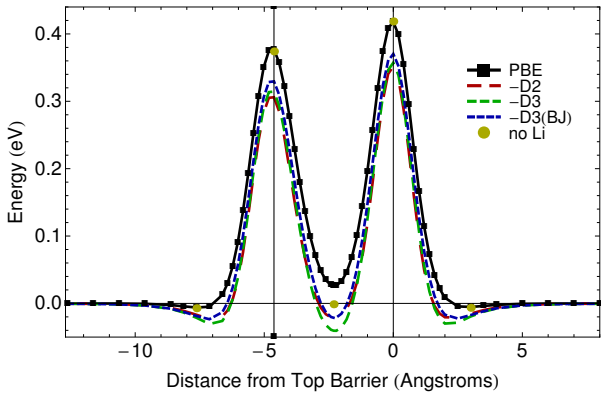

Figure 6.1.2: Potential energy surface for the transmission of He atoms through the double-barrier structure.

gives a 0.015 eV higher barrier, and the various dispersion corrected-PBE results give an approximately 0.04 eV lower barrier. The potential wells above and below the 2D-PP are roughly -0.009 eV at 2.67 Å from the barrier for uncorrected PBE, and roughly 0.030-0.043 eV at 2.05-2.32 Å for dispersion-corrected PBE. This demonstrates the agreement between the dispersion-corrected DFT result and the previous post-HF results. This is important because the dispersion-corrected DFT approach is more computationally tractable than MP2 and can be used for periodic structures, eliminating the need to create finite-sized models of the porous structures.

The PES for Li_2@(2D-PP)$_2$ is shown in Fig. (6.1.2). The barrier height maxima are lower (0.38 and 0.42 eV versus 0.54 eV for 2D-PP) and wider (the minima of the potential energy wells on either side are 2.79 Å from the pore versus 2.67 Å for 2D-PP) than the single 2D-PP PES. There is also a small asymmetry of 0.041 eV between the two maxima of the PES, that arises from the asymmetrical location of the lithium atom with respect to the top and bottom benzene rings of the 2D-PP sheets, which tilts and twist the benzene rings, bringing the hydrogen atoms on those rings a little closer and further away from the pore center, (see Fig. (6.1.1e) and thus slightly increasing or decreasing the PES barrier heights. (A similar asymmetry was observed in DFT calculations of metal atoms on the surface of 2D-PP. [83]) While the geometry asymmetry is small, because the transiting helium atom is within the van der Waals radii of the hydrogen atoms comprising the pore, this small geometry change creates a relatively large change in the PES. For the slightly higher barrier, the He atom is 0.05 Å closer to the inner ring of hydrogen atoms, 0.01 Å closer to the first ring of carbon atoms, 0.14 Å further from the second ring of carbon atoms, and 0.12 Å further from the lithium atoms than in the other pore. This suggests that the barrier height depends more on helium proximity to the first ring of hydrogens

and carbons than to the lithium atoms and the second ring of carbon atoms, since it is likely that this proximity slightly increases the barrier height due to overlapping electron densities. In the 3x3 supercell, there are four possible pores for atom transmission; these have barrier heights of 0.42, 0.39, 0.39, and 0.43 eV for the 2D-PP surface slightly further from the Li atoms, and values of 0.38, 0.38, 0.37, and 0.36 eV for the surface slightly closer to the Li atoms. Overall variations in barrier height were on the order of 0.03 eV. Following the discussion above, it is likely that similar slight geometry differences among the other pores contribute to the deviations in barrier heights.

To understand the role of the lithium atoms on the PES, we also computed a few points on the PES in which we kept the geometry of the 2D-PP sheets fixed but removed the Li atoms (shown as yellow circles in Fig. (6.1.2). The barrier height asymmetry only increases by 0.004 eV when no lithium atoms are present, supporting the claim that the PES asymmetry is primarily due to the interaction with hydrogen atoms lining the pore, and not due to the asymmetrical position of the lithium atoms. The nearly identical PES demonstrates that the features of the PES, including its asymmetry, are dictated by the interactions with the hydrogen atoms lining the pore, rather than the lithium atoms. This is important, because it suggests that the metal atoms primarily control the spacing between the maxima, and induce only small modifications to the shape of the PES.

Addition of the Li atoms to the double barrier system resulted in small, systematic changes in partial charges within the system, as demonstrated by Hirsfeld-I calculations performed on the unit cell. Charges on C3 carbons, originally approximately 0.10 e-charge, generally decreased by no more than roughly 0.05 e- with the addition of Li, while partial charges on C2H carbons, originally approximately 0.22-0.23 e-, generally decreased by roughly 0.08 e-. Partial charges on hydrogens throughout the structure increased from approximately 0.11-0.12 e- to approximately 0.12-0.14 e-. These results suggest that the addition of Li atoms does not significantly disrupt the overall electronic properties of the structure.

6.2 Thermal rate constant for ^{3}He-^{4}He

As described in the previous Section, resonant tunneling can be used to separate isotopes of Helium. However, resonant tunneling becomes dominant only at very low temperature. In Chap. 5 we showed that our ODE method can successfully be used for the calculation of the thermal rate constant $k(T)$, even in deep resonant regime where $k(T)$ is dominated by the quasi-metastable states. Hence, in this Section, we will use our numerical ODE method to prove that the two isotopes of Helium can be separated using resonant tunneling.

6.2.1 Numerical convergence of $k\,(T)$

As described in Sec. 2.2, the Boltzmann-weighted energy integration of $T(E)$ gives the thermal rate constant $k\,(T)$ for one-dimensional systems, i.e.

$$\mathcal{Q}_{react}\,(T)\,k\,(T) = \frac{1}{2\pi\hbar}\int_0^{+\infty} dE\, e^{-\beta E} T\,(E)\,, \tag{6.2.1}$$

where $\beta = \frac{1}{k_B T}$ is the inverse temperature. In this thesis, we are interested in the deep resonant regime at very low temperature, where resonant tunneling becomes dominant. Because we want to numerically integrate Eq. (6.2.1), we have to fix both a lower-bound energy cutoff E_{min} and an upper-bound energy cutoff E_{max} in Eq. (6.2.1). In this Section, we will show that an inappropriate choice of these energy cutoffs E_{min} and E_{max} might lead to a completely wrong value of the thermal rate constant $k\,(T)$ at low temperature.

It is easy to observe that the upper-bound energy cutoff E_{max} is relevant only in the high temperature regime. Indeed, for very large energy $E \gg V_o$, where $V_o = \max_x V\,(x)$ is the highest barrier in the potential profile, we expect that $T\,(E) \approx 1$. Hence, it is possible to approximate the thermal rate constant in Eq. (6.2.1) as

$$\mathcal{Q}_{react}\,(T)\,k\,(T) \approx \frac{1}{2\pi\hbar}\int_0^{E_{max}} dE\, e^{-\beta E} T\,(E) + \frac{1}{2\pi\hbar} e^{-\beta E_{maxx}}, \tag{6.2.2}$$

where E_{max} satisfies the condition $|1 - T\,(E_{max})| \leq 10^{-4}$. Different is the case of the lower-bound energy cutoff E_{min}. In fact, at low temperature, the thermal rate constant in Eq. (6.2.1) is strongly dominated by those energies such that $E \approx \beta^{-1}$. Therefore, in order to correctly compute $k\,(T)$ at very low temperature, the lower-bound energy cutoff E_{min} must be small enough. In order to test how small E_{min} must be, we study the relative error in computing the thermal rate constant $k\,(T)$ for the two isotopes of Helium diffusing through a single Eckart barrier potential $V\,(x) = \frac{V_0}{\cosh^2\left(\frac{\pi x}{a}\right)}$, with a typical width of $a = 2$ Å and height $V_0 = 0.4$ eV (see Fig. (6.2.1)). In Fig. (6.2.2), the comparison between exact thermal rate constant $[\mathcal{Q}_{react}\,(T)\,k\,(T)]_{\text{Exact}}$ and the thermal rate constant computed with a fixed lower-bound energy cutoff $[\mathcal{Q}_{react}\,(T)\,k\,(T)]_{E_{min}}$ is shown. As expected, E_{min} must be decreased accordingly with temperature. In particular, for very low temperature $T \approx 20$K, the lower-bound energy cutoff must be of the order $E_{min} \approx 10^{-40}$ eV!

Interestingly, more subtle problems arise when the ratio between the thermal rate constants of the two isotopes of the Helium is considered. From the definition of the

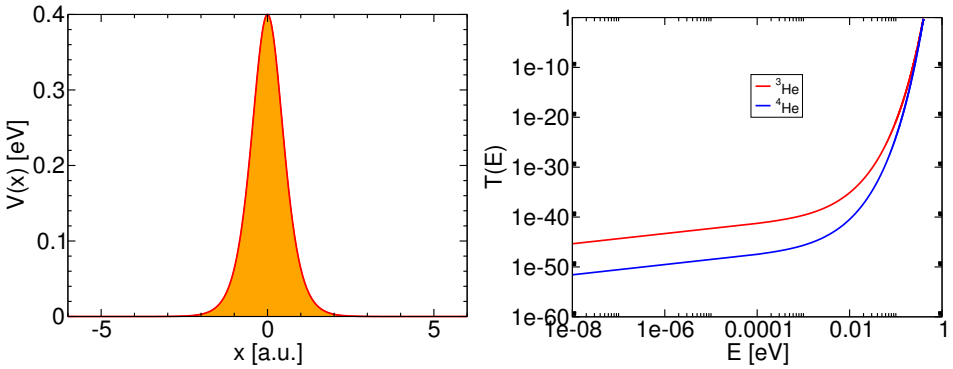

Figure 6.2.1: (Left) Potential profile for the single Eckart barrier $V(x) = \frac{V_0}{\cosh^2\left(\frac{\pi x}{a}\right)}$ used for the convergence test. Here, $V_0 = 0.4$ eV and $a = 2$ Å. (Right) Exact transmission probability $T(E)$ for the ^{3}He (red, upper curve) and ^{4}He (blue, bottom curve). As expected, ^{3}He has a larger transmission probability than ^{4}He at low temperature.

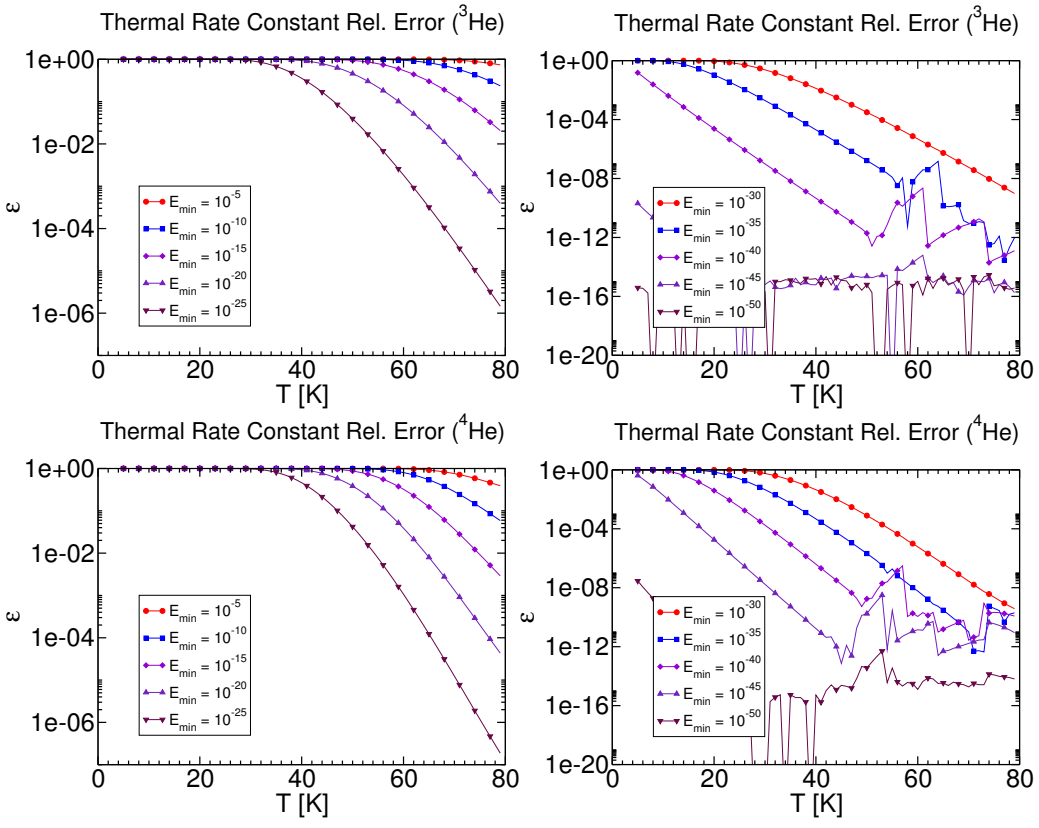

Figure 6.2.2: Analysis of the relative error, defined as $\varepsilon = \left| \frac{[\mathcal{Q}_{react}(T)k(T)]_{\text{Exact}} - [\mathcal{Q}_{react}(T)k(T)]_{E_{min}}}{[\mathcal{Q}_{react}(T)k(T)]_{\text{Exact}}} \right|$, at varying minimum energy cutoff E_{min}.

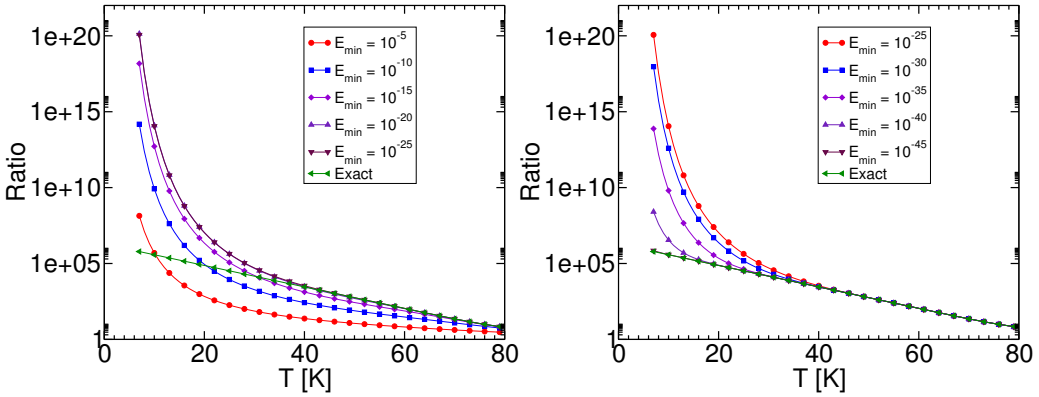

Figure 6.2.3: Comparison of the exact ratio between the thermal rate constants of ^{3}He and ^{4}He,ratio $= \frac{\mathcal{Q}_{react}(T) k_{^3He}(T)}{\mathcal{Q}_{react}(T) k_{^4He}(T)}$, and the same quantity varying the minimum energy cutoff E_{min}: the approximated ratio might be either larger or smaller than the exact ratio. Hence, the choice of the cutoff E_{min} is of fundamental importance.

thermal rate constant $k\,(T)$ in Eq. (6.2.1), it is easy to see that

$$\left[\mathcal{Q}_{react}\,(T)\,k\,(T)\right]_{\text{Exact}} \geq \left[\mathcal{Q}_{react}\,(T)\,k\,(T)\right]_{E_{min}} \geq \left[\mathcal{Q}_{react}\,(T)\,k\,(T)\right]_{E'_{min}}, \tag{6.2.3}$$

where the inequality is true for any $E_{min} < E'_{min}$. Therefore, at first sight, one can think that errors introduced by the lower-bound cutoff E_{min} are negligible when considering the ratio of thermal rate constants between the isotopes of Helium

$$\text{ratio} = \frac{\mathcal{Q}_{react}\,(T)\,k_{^3He}\,(T)}{\mathcal{Q}_{react}\,(T)\,k_{^4He}\,(T)}. \tag{6.2.4}$$

In conclusions, as shown in Fig. (6.2.3), the ratio in Eq. (6.2.4) is strongly dependent on the value of E_{min}. In particular, it is possible to observe that the approximated ratio with a fixed E_{min} might be either larger or smaller than the actual ratio. Finally, the value of E_{min} must be carefully chosen in order to consistently compute any thermal rate constant ratio as in Eq. (6.2.4).

6.2.2 Calculation of the Thermal Rate Constant for ^{3}He-^{4}He in resonant tunneling regime: the double barrier 2D-PP layer potential

In order to compute the thermal rate constant, we employ the potential shown in Fig. (6.1.2) with $m_3 = 5497.89$ eV and $m_4 = 7296.3$ eV, the masses respectively for ^{3}He and ^{4}He. Figure (6.2.4) shows the transmission probability $T(E)$ of the two isotopes through Li_2@(2D-PP)$_2$ as a function of incident kinetic energy, computed with our ODE method. As expected, the resonant transmission peaks for ^{4}He are shifted respect to those

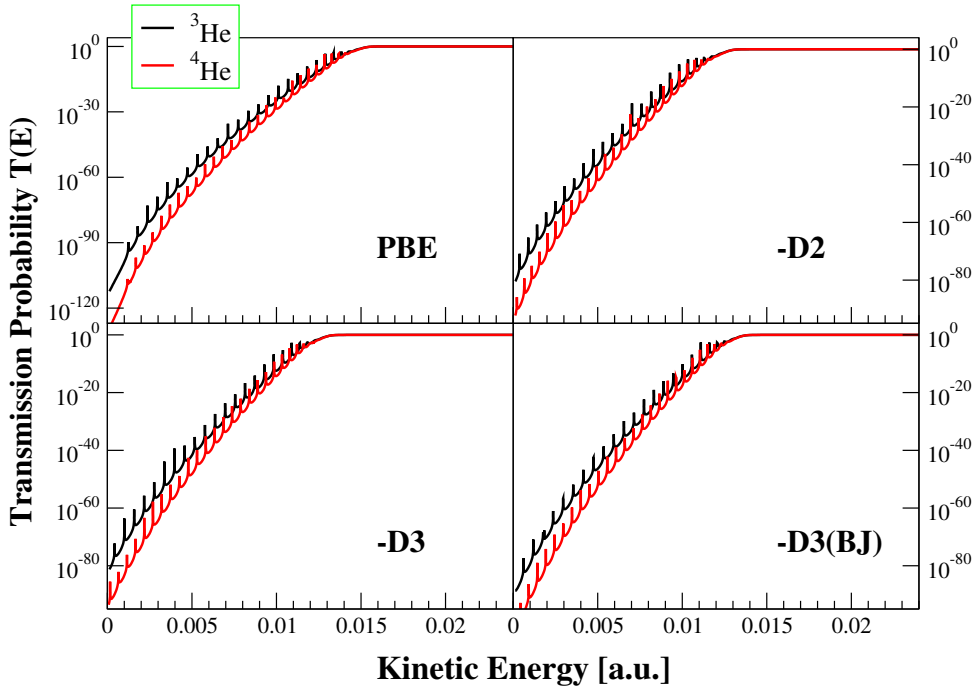

Figure 6.2.4: Transmission probability of ^{3}He and ^{4}He through Li_2@(2D-PP)$_2$ double-barrier potential as a function of kinetic energy.

of ^{3}He, due to the different metastable energy levels between the two barriers. Unlike the symmetric double-barrier potential, asymmetric double-barriers do not have unit transmission at resonances.

As explained in Sec. 2.2, the Boltzmann-weighted energy integration of $T(E)$ gives the thermal rate constant $k(T)$, i.e. the fraction of reactants (He atoms) crossing the Li_2@(2D-PP)$_2$ double layer per unit of time at fixed temperature. When employing the PBE bare potential, the rate values are those reported with black lines, while the red values correspond to employing the potential corrected by the -D2 functional. There can be up to 5 orders of magnitude difference between these rate calculations. This shows how important it is to properly correct the DFT functional. The ^{4}He rates (dashed lines) are always smaller than the ^{3}He ones, because of the less amount of tunneling of ^{4}He respect to ^{3}He and the partition function difference. A close comparison with the classical Transition State rates [1,2,4] is reported below.

On the same panel of Fig.(6.2.5), the scattering rates from a 2D-PP layer at the level of -D2 potential calculations are reported by green lines. [74] These are about ten orders of magnitude smaller than the double barrier -D2 corrected ones, due to the higher energy barrier of the 2d-PP layer. We calculated also other single barrier [79] rates, reported on

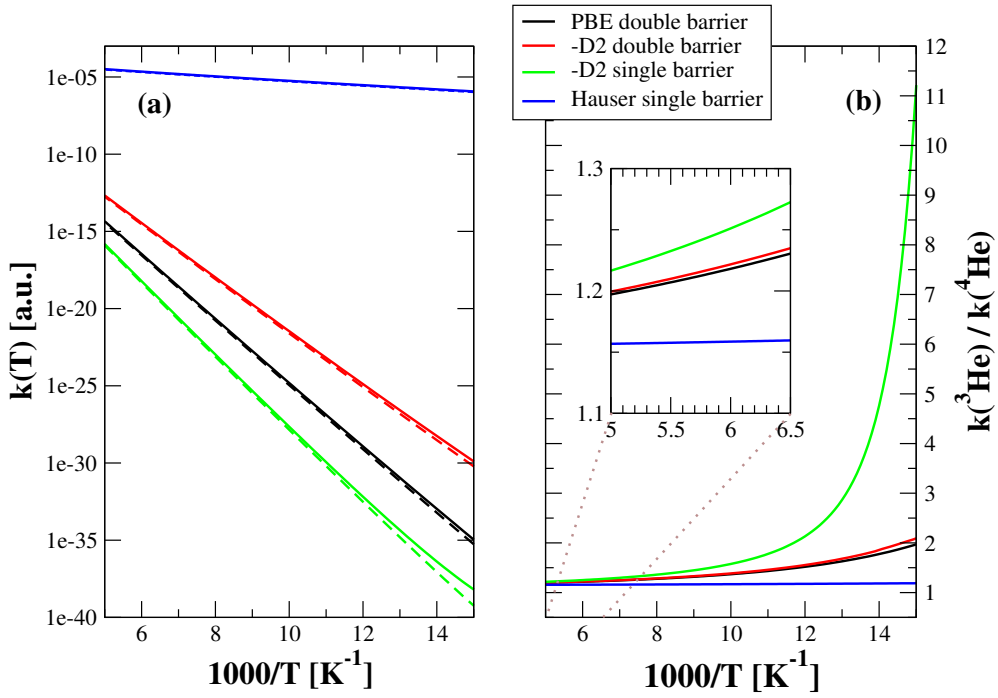

Figure 6.2.5: Temperature dependence of the: (a) thermal rate constants of ^{3}He (continuous lines) and ^{4}He (dashed lines) through the double-barrier; (b) Ratio of the ^{3}He and ^{4}He thermal rate constants. Inset for thermal rates ratio from 150 to 200 K.

the same Figure by blue lines. These rates values are between 20 to 30 order of magnitude bigger than the Li_2@(2D-PP)$_2$ rates in the temperatures ranging from 60 to 200 K. On one side, such a single barrier, cleverly designed by Hauser et al. [79], allows for a large amount of ^{3}He atoms flux across the layer. On the other, the thermal rate ratio is very much contained in the temperatures range from 60 to 200 K. Instead, the Li_2@(2D-PP)$_2$ double barrier potential allow for a better selection between the two isotopes within the same temperatures range. Actually, the single barrier, elaborated by [74] shows an even stricter isotope selection. More specifically, the inset of panel (b) in Fig.(6.2.5) shows that ratio of the rates, obtained with the potential of Hauser et al. is constant and is exclusively due to the partition function ration of ^{3}He and ^{4}He (~ 1.155). In order to activate tunneling selection between the two isotopes according to this single barrier potential, much lower temperatures should be reached. Instead, both single [74] and the present double barrier results include tunneling contributions for the selection of ^{3}He from ^{4}He even at temperature of 200 K.

As a general rule of thumb, one can assert that the higher the flux of isotopes, the smaller the rate ratio and, consequently, the ability to select the ^{3}He isotope. Clearly, it is necessary to fix the temperature in order to see if the amount of flux is the desired one. However, we think that the present amount of rates for the Li_2@(2D-PP)$_2$ can turn useful for experimental implementation (see below for details). For example, at 77 K (the nitrogen evaporation temperature) the rate is of the order of 10^{-24} a.u./molecule $= 6.13 \times 10^{-39}\text{cm}^3/molecule \times s = 3.7 \times 10^{-15}\text{cm}^3/mol \times s$, where "mol" stands for mole. Assuming the mole of gas is contained into a spherical volume, then 1cm^3 correspond to a surface of 22cm^2. In such a surface we can place about 2×10^{16} holes, given a hole every 10 Å^2. Thus, we can say that we have a number of $3.7 \times 10^{-15} \times 2 \times 10^{16}\text{cm}^3/mol \times s = 7.4 \times 10\text{cm}^3/mol \times s$ He atoms per moles escaping the volume per second. Then, per unit of surface the rate is $7.4 \times 10\text{cm}^3/10 \times 10^{-16}\text{cm}^2 mol \times s = 7.4 \times 10^{16}\text{cm}/mol \times s$. Given the rates ratio of 1.5, 60% of these molecules are ^{3}He isotopes and by repeating the procedure one can have a $1.5 \times 1.5 = 2.25$ effective ratio, with a composition of 70% of ^{3}He. And so on so forth. This is equal to 0.01 mole of ^{3}He gas per day per surface/volume in the case of a spherical container shape, i.e. per cm unit. If one take a irregular and porous composition of Li_2@(2D-PP)$_2$ and other materials with large surface area to volume ratios the ^{3}He reacts at much faster rates than monolithic spherical materials, because more surface is available.

6.2.3 Approximated full dimensional calculations

In Chap. 6, all theoretical calculations are confined to a one-dimensional model and one may wonder how the rate and, eventually, the ratio would change if dealing with the full dimensional problem. We performed classical and tunneling corrected calculations for the full dimensional rate. In the first case, we employed the Transition State Theory (Sec. 1.2) according to which the thermal rate constant is

$$k^{TST}(T) = \frac{k_B T}{2\pi\hbar} e^{-\beta V(x_\circ)} \frac{Q^{TS}(T)}{Q_{3d}^{He}(T)\, Q^{2d-PP}(T)} \tag{6.2.5}$$

where $V(x_\circ)$ is the highest potential value between the two barrier tops located at $x_\circ$ along the reaction path, $Q^{TS}(T)$ is the harmonic vibrational partition function of the He atom and the 2d-PP layer placed at $x_\circ$, $Q^{2d-PP}(T)$ harmonic vibrational partition function of the bare 2d-PP and $Q_{3d}^{He}(T)$ the 3-dimensional free He atom one. The second layer can be disregarded in the transition state approximation because it does not interact with the He atom when the He atom is on the other layer's plane. As an alternative formulation which includes tunneling, we consider the scattering motion to be adiabatic respect to the others degrees of freedom and obtain the following tunneling-corrected rate expression

$$k(T) = \left(k_{1d}(T)\, Q_{1d}^{He}(T)\right) \frac{Q^{TS}(T)}{Q_{3d}^{He}(T)\, Q^{2d-PP}(T)} \tag{6.2.6}$$

where $k_{1d}(T)$ are the rates values reported in Fig.(6.2.5) and $Q_{1d}^{He}(T)$ the corresponding one-dimensional partition function. Results are reported in Figs. (6.2.6), (6.2.7), (6.2.8) and (6.2.9) and the full dimensional rates are about one order of magnitude smaller than one-dimensional ones.

6.2.4 Estimate for the number of He atoms filtered by the 2D-PP double layers

In this Section, we will provide a **classical** derivation of the number of particles which flow through the 2D-PP double layer for a fixed rate constant value. Suppose we have an ideal gas inside a box and suppose that one of its sides is made of 2D-PP, for instance the side perpendicular to the x axes. The number of particles that reach the filter of surface A in an interval of time Δt can be estimates as

$$\# = \frac{p_x}{m} A\, \Delta t\, p(v_x) \frac{N}{V}, \tag{6.2.7}$$

where $p(v_x)$ is the Boltzmann probability to have a particle with a (positive) velocity v_x and N and V are respectively the number of particles and the volume of the system. Assuming an homogeneous distribution of holes with density ρ_{holes} per unit of surface,

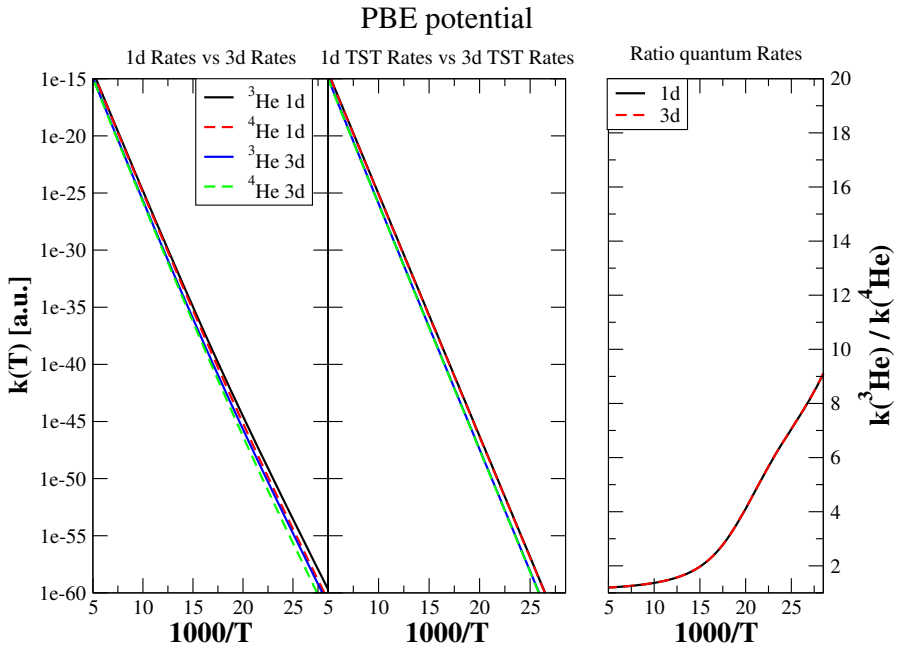

Figure 6.2.6: Left panel: one-dimensional and extrapolated full dimensional thermal rates constant of ^{3}He and ^{4}He scattering across a Li_2@(2D-PP)$_2$ employing the PBE potential. Central panel in Transition State Theory approximation and right panel the ratio of the rates.

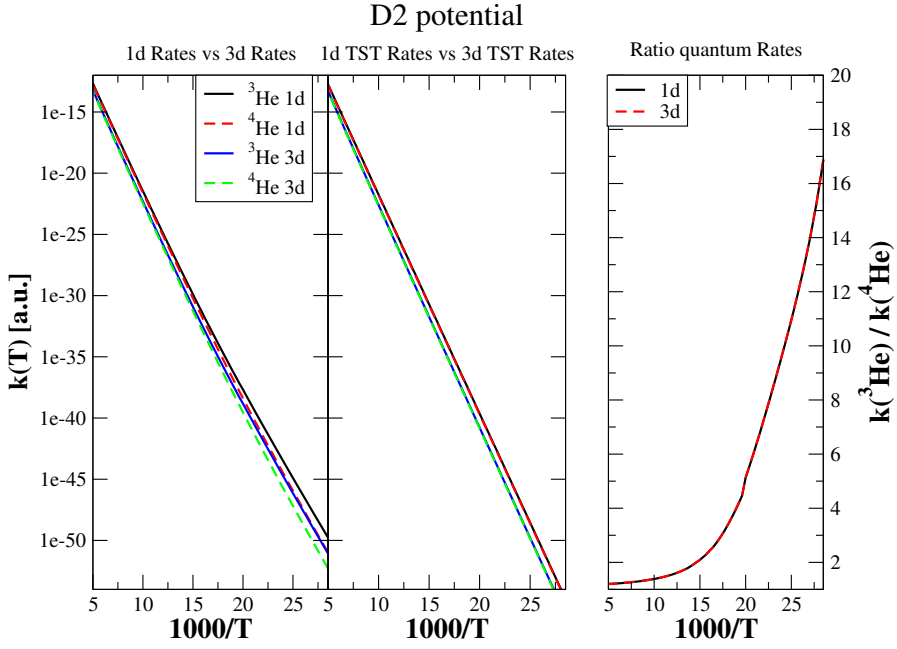

Figure 6.2.7: Left panel: one-dimensional and extrapolated full dimensional thermal rates constant of ^{3}He and ^{4}He scattering across Li_2@(2D-PP)$_2$ employing the -D2 potential correction. Central panel in Transition State Theory approximation and right panel the ratio of the rates.

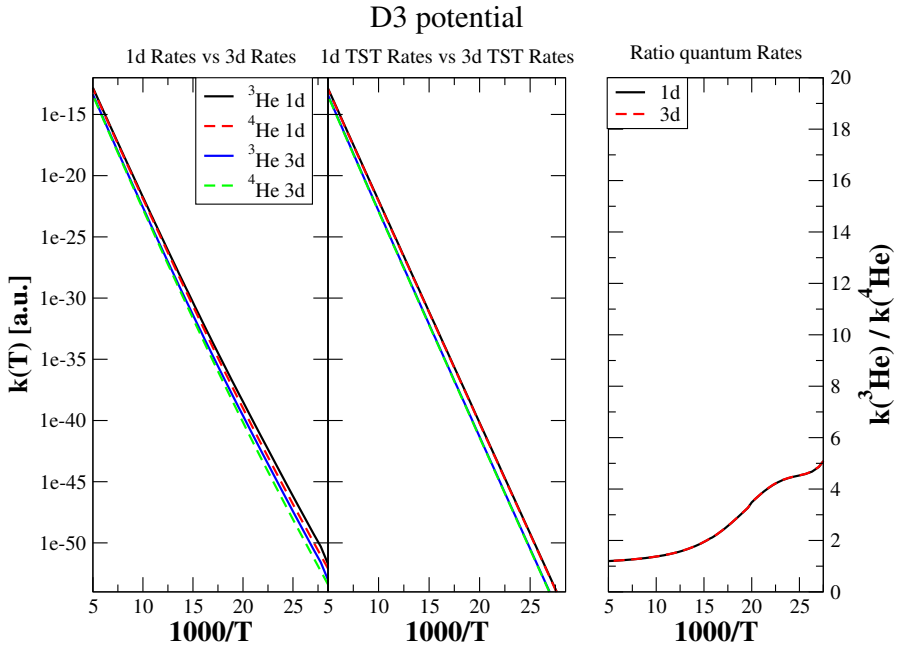

Figure 6.2.8: Left panel: one-dimensional and extrapolated full dimensional thermal rates constant of ^{3}He and ^{4}He scattering across Li_2@(2D-PP)$_2$ employing the -D3 potential correction. Central panel in Transition State Theory approximation and right panel the ratio of the rates.

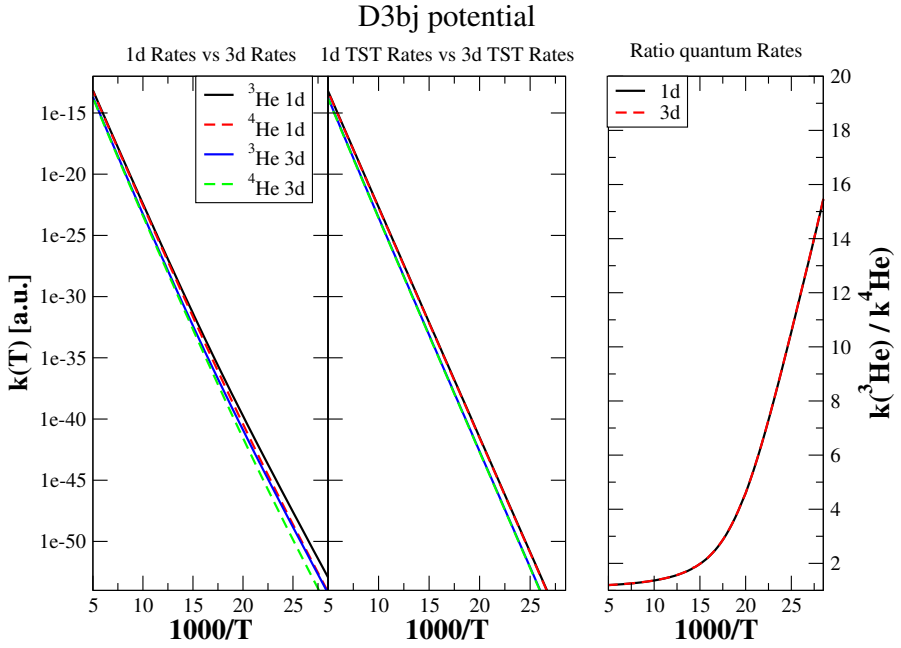

Figure 6.2.9: Left panel: one-dimensional and extrapolated full dimensional thermal rates constant of ^{3}He and ^{4}He scattering across Li_2@(2D-PP)$_2$ employing the -D3(BJ) potential correction. Central panel in Transition State Theory approximation and right panel the ratio of the rates.

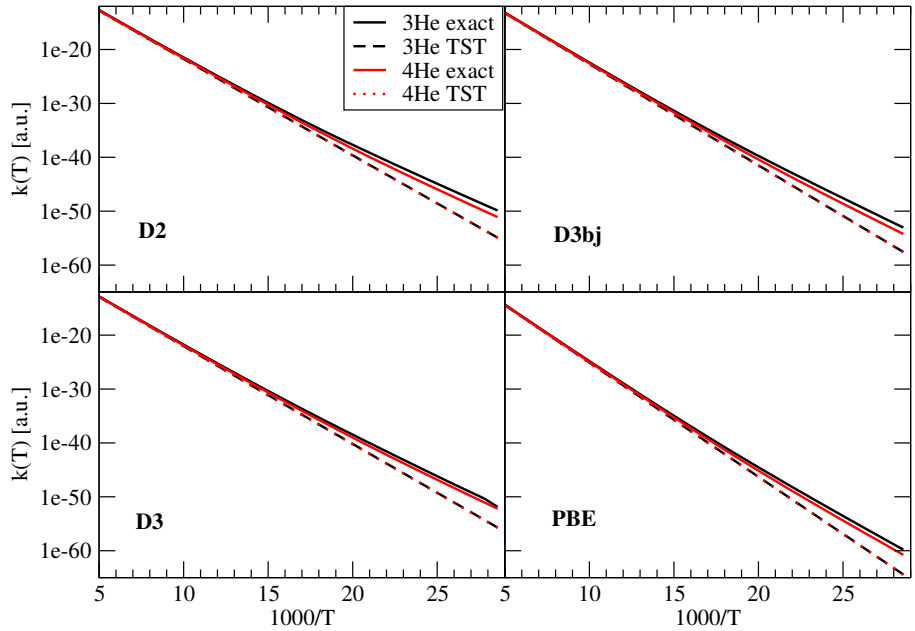

Figure 6.2.10: One-dimensional thermal rate constants with (exact) and without (TST) tunneling contribution for ^{3}He and ^{4}He. Different panel for different potential energy surface set-up.

the probability that a single particle can flow through a hole is

$$p_{int} = \rho_{holes} A_{hole} T(E_x), \tag{6.2.8}$$

where A_{hole} is the interaction area of one hole and $T(E_x)$ is the transmission probability of a particle with energy $E_x = \frac{\hbar^2 p_x^2}{2m}$ (in this simple model we assume that the hole-interaction Hamiltonian depends only on the dimensionality perpendicular to the hole). Hence, the total number of particles that cross the filter per unit of time and surface for a fixed velocity v_x will be

$$j_{cross}(v_x) = \frac{\# p_{int}}{A\,\Delta t} = \frac{p_x}{m}\, p(v_x) \frac{N}{V} \rho_{holes} A_{hole} T(E_x). \tag{6.2.9}$$

Using the quantities we previously introduced we obtain

$$\begin{aligned} j_{cross} &= \frac{N}{V} (\rho_{holes} A_{hole}) \sqrt{\frac{1}{2\pi m\, k_B T}} \int_0^{+\infty} dp_x e^{-\frac{p_x^2}{2m\, k_B T}} \frac{p_x}{m} T(E_x) \\ &= \frac{N}{V} (\rho_{holes} A_{hole}) \sqrt{\frac{k_B T}{2\pi m}} \int_0^{+\infty} dy\, e^{-y} T\left(\frac{y}{k_B T}\right) \\ &= \frac{P}{\sqrt{2\pi m\, k_B T}} (\rho_{holes} A_{hole}) \int_0^{+\infty} dy\, e^{-y} T\left(\frac{y}{k_B T}\right) \end{aligned} \tag{6.2.10}$$

where in the last equality we used the ideal gas law $PV = N\,k_B T$. Recalling that

$$\mathcal{Q}_{react}\,(T)\,k\,(T) = \frac{1}{2\pi\hbar}\int_0^{+\infty} e^{-\frac{E}{k_B T}}\,T(E) = \frac{k_B T}{2\pi\hbar}\int_0^{+\infty} dy\,e^{-y}T\left(\frac{y}{k_B T}\right), \tag{6.2.11}$$

we have

$$j_{cross} = \frac{P}{(k_B T)^{3/2}}\sqrt{\frac{2\pi\hbar^2}{m}}\,(\rho_{holes}A_{hole})\,(\mathcal{Q}_{react}\,(T)\,k\,(T))\,. \tag{6.2.12}$$

Using the equivalences

$$1\;J = 1\;Kg\,\frac{m^2}{s^2} \tag{6.2.13a}$$

$$P = 1\;atm = 1.01\times 10^5\;Pa = 1.01\times 10^5\;\frac{Kg}{m\,s^2} = 1.01\times 10^5\;J\,m^{-3} \tag{6.2.13b}$$

$$k_B = 1.380\times 10^{-23}\;J\,K^{-1} \tag{6.2.13c}$$

$$\hbar = 1.054\times 10^{-34}\;J\,s \tag{6.2.13d}$$

$$m = 5.003\times 10^{-27}\;Kg \tag{6.2.13e}$$

$$N_a = 6.022\times 10^{23}\;mol^{-1} \tag{6.2.13f}$$

$$(\rho_{holes}A_{hole}) = 1, \tag{6.2.13g}$$

we obtain

$$\begin{aligned} j_{cross} &= \frac{P}{T^{3/2}}\,(k\cdot Q_R)\cdot 1.22\times 10^{-5}\;m^{-2}mol \\ &= \frac{P}{T^{3/2}}\,(k\cdot Q_R)\cdot 1.22\times 10^{-7}\;cm^{-2}mol, \end{aligned} \tag{6.2.14}$$

where P is expressed in atm and T in K. For a free particle at $T = 77\;K$ and $P = 1\;atm$ we have

$$(\mathcal{Q}_{react}\,(T)\,k\,(T))^{FP}_{77\;K} = \frac{k_B T}{2\pi\hbar} = 1.60\times 10^{12}\;s^{-1} = 1.39\times 10^{17}\;day^{-1}, \tag{6.2.15}$$

and then

$$j^{FP}_{cross}(77\;K) = 2.51\times 10^7\;cm^{-2}\,day^{-1}mol. \tag{6.2.16}$$

For a 3-Helium particle the thermal reaction constant at $T = 77\;K$ is

$$(\mathcal{Q}_{react}\,(T)\,k\,(T))_{77\;K} = 5.26\times 10^{-23}\;psec^{-1} = 4.54\times 10^{-6}\;day^{-1}, \tag{6.2.17}$$

and finally

$$j_{cross}(77\;K) = 8.21\times 10^{-16}\;cm^{-2}\,day^{-1}\,mol. \tag{6.2.18}$$

CHAPTER 7

Inverse Kinetic Isotope Effect Induced by Resonant Tunneling

In the previous Chapter we have discussed how isotopes can be separated using a "quantum" filter, exploiting quantum resonant tunneling properties. In particular, we showed that resonant tunneling introduces a non trivial contribution to the thermal rate constant $k(T)$, increasing the probability for ^{3}He to cross the quantum filter, and reducing at the same time the probability for ^{4}He to cross the filter. As a quantum filter, we considered a bilayer structure of two-dimensional polyphenylene, a nanoporous analogue of graphene (2D-PP, Fig. (6.1.1)). In this case, the distance between the two potential barriers was completely determined by the conformal configuration of the polyphenylene used for producing the filter. In fact, using different molecules it is possible to produce two layers quantum filters with different spacing, i.e. with an arbitrary distance between the two potential barriers. Therefore, it is of paramount importance to understand what should be the optimal distance between the potential barriers that can lead us to develop more suitable quantum filters.

In this Chapter, we will use our ODE method (Chap. 5) to extensively study the effects of the resonant tunneling by varying the distance Δ between two potential barriers. In particular, we will show that resonant tunneling induces "oscillations" in the thermal rate constant $\mathcal{Q}_{react}(T)\, k(T)$ that varies by changing the distance between the barriers Δ. More importantly, we found that this oscillations lead to important phenomena of the type of the "Inverse Isotope Effects", where heavier isotopes result to have an higher thermal rate constant with respect to the lighter ones. We want to stress that, at the moment and according to our knowledge, we are the first group who was able to numerically observed these phenomena for a double Eckart barrier potential, even for one-dimensional systems.

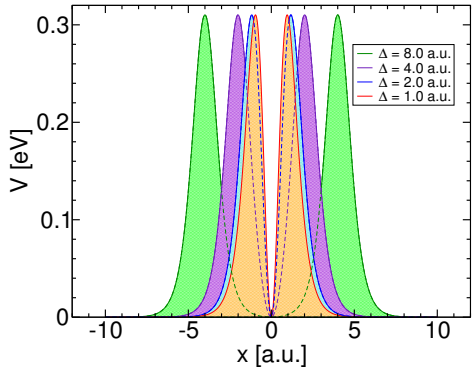

Figure 7.1.1: Potential profiles of Eq. (7.1.1), varying the distance of the two barriers Δ.

7.1 Thermal Rate Constant Oscillations

In order to study the effects of the resonant tunneling on the thermal rate constant $k\left(T\right)$ by varying the distance Δ between barriers, we used the following potential

$$V\left(x;\,\Delta\right)=V_0\left[\frac{1}{\cosh^2\left(x-\Delta/2\right)}+\frac{1}{\cosh^2\left(x+\Delta/2\right)}-\frac{2}{\cosh^2\left(\Delta/2\right)\cosh^2\left(x\right)}\right], \quad (7.1.1)$$

where $V_0\left(\Delta\right)$ is chosen so that $\max_x V\left(x;\,\Delta\right)=V_0=0.310$ eV. Classical approximation to the thermal rate constant will of course not depend on the value of Δ and thermal rate constants can be directly compared to quantum ones. In Fig. (7.1.1), different potential profiles are shown by varying Δ. One can observe that potential profiles in Eq. (7.1.1) have the property

$$V\left(0;\,\Delta\right)=0, \quad (7.1.2)$$

which ensures that quasi-bound states can be found at any $E>0$. Unlike Chap. 6 where two isotopes of Helium were used for calculations, here we consider a lighter couple of isotopes: the Hydrogen (H) and its isotope, the Deuterium (^{2}H), with masses respectively $m=1.834\times10^3$ and $m_2=3.671\times10^3$ in atomic units. Because, Hydrogen and Deuterium atoms are two times lighter than Helium isotopes, numerical results include a consistent tunneling contribution.

As described in Sec. 2.2, the Boltzman-weighted energy integration of $T(E)$ gives the thermal rate constant $k\left(T\right)$ for one-dimensional systems is

$$\mathcal{Q}_{react}\left(T\right)k\left(T\right)=\frac{1}{2\pi\hbar}\int_0^{+\infty}dE\,e^{-\beta E}T\left(E\right), \quad (7.1.3)$$

where $\beta=\frac{1}{k_BT}$ is the inverse temperature. The transmission probabilities $T\left(E\right)$ at

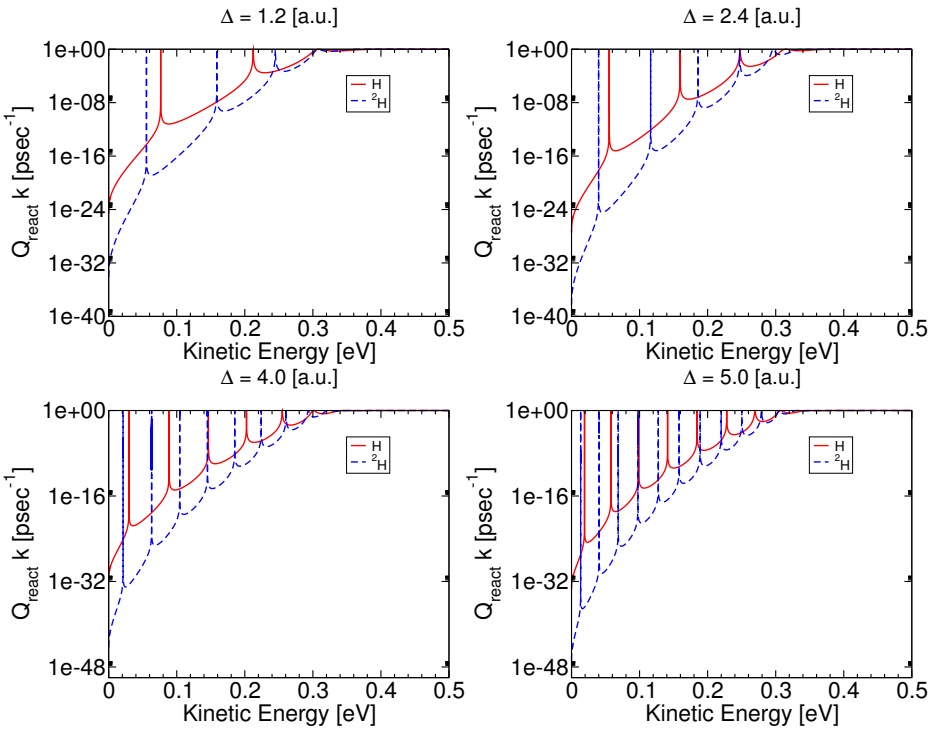

Figure 7.1.2: Transmission probabilities $T(E)$ at different distances between the two barriers Δ. As expected, the heaviest isotope has a higher number of resonant peaks than the lightest isotope.

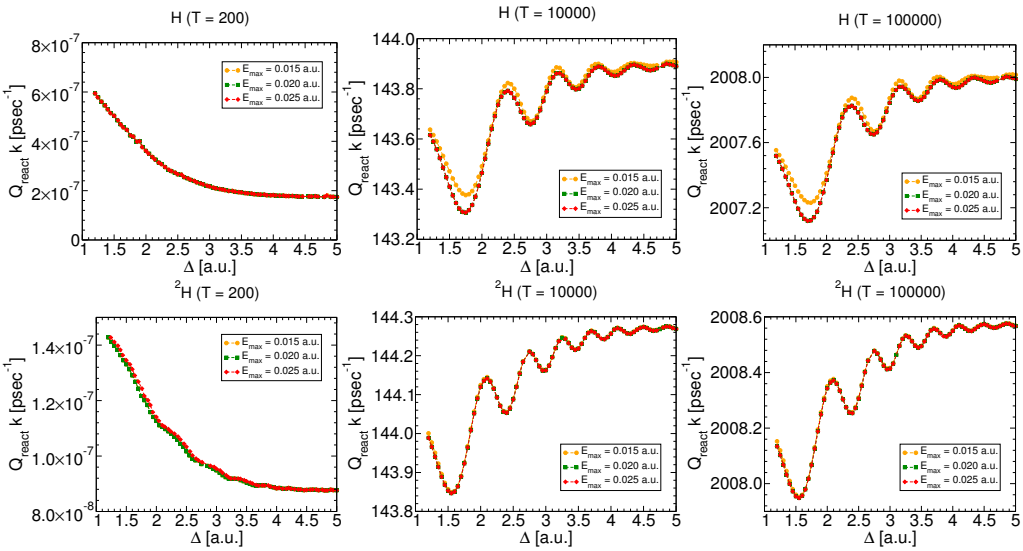

Figure 7.1.3: Thermal rate constant $\mathcal{Q}_{react}\,(T)\;k\,(T)$ varying the upper-bound cutoff E_{max}, at fixed $\Delta E = 2.72 \times 10^{-4}$ eV. As expected, the error is larger for higher temperature and greater energy integration spacing.

different distances between the barrier Δ are shown in Fig. (7.1.2). For the calculation of $T\,(E)$, we considered the energy range $E \in \left[2.72 \times 10^{-4}\,\text{eV},\, 0.680\,\text{eV}\right]$ with $\Delta E = 2.72 \times 10^{-4}$ eV. These parameters have been tested as shown in Fig. (7.1.3, 7.1.4)). Below and above the energy range, we set $T\,(E)$ respectively to zero and one. Successively, a bisection method has been used in order to enhance $T\,(E)$ around resonant peaks. As expected, the number of resonant peaks increases with Δ and the number of resonant states for the lightest isotope is smaller than the number of resonant states for the heaviest isotope. In Fig. (7.1.5), we report $\mathcal{Q}_{react}\,(T)\,k\,(T)$, at fixed $\Delta = 0.7,\, 1.5,\, 2.0,\, 2.5$ a.u. Interestingly, the contribution to $k\,(T)$ from the resonant tunneling is non-trivial. At high temperature, where quantum tunneling is negligible, TST approximation to the thermal rate constant

$$\left[\mathcal{Q}_{react}\,(T)\,k\,(T)\right]_{TST} = \frac{1}{2\pi\hbar}\int_0^{+\infty} dE\, e^{-\beta E}\theta\,(E - V_0) = \frac{k_B T}{2\pi\hbar} e^{-\frac{V_0}{k_B T}}, \tag{7.1.4}$$

gives good results, independently to the choice of Δ. On the contrary, at very low temperature, where the deep resonant tunneling is crucial, the thermal rate constant $k\,(T)$ is larger for larger Δ (see Left-panel of Fig.(7.1.5) at very low temperatures). For intermediates temperatures, it is possible to observe a transition between the high and the low temperature regime.

Here, we will study the thermal rate constant $k\,(T)$ by varying the distance between

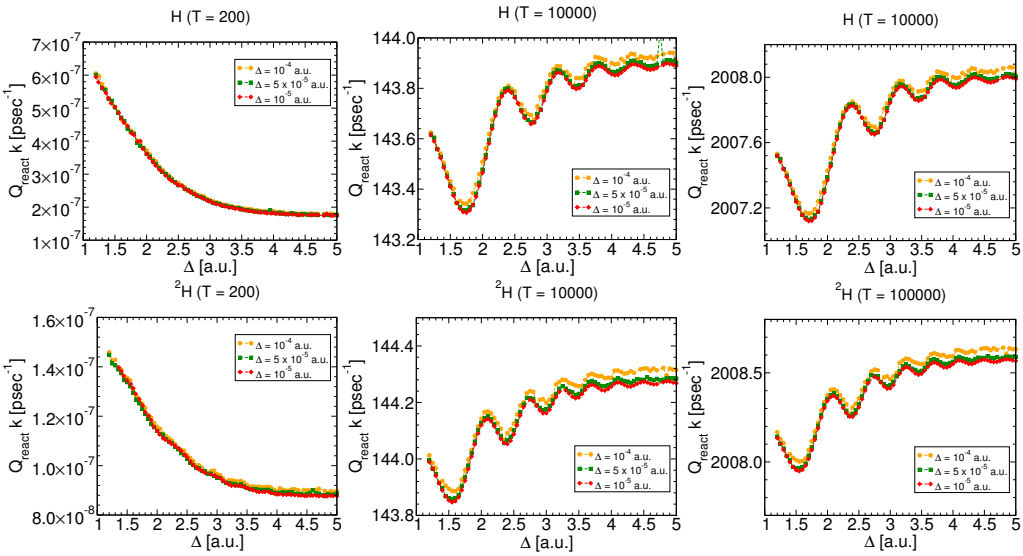

Figure 7.1.4: Thermal rate constant $\mathcal{Q}_{react}\,(T)\;k\,(T)$ varying the energy step ΔE, $E_{max} = 0.680$ eV.

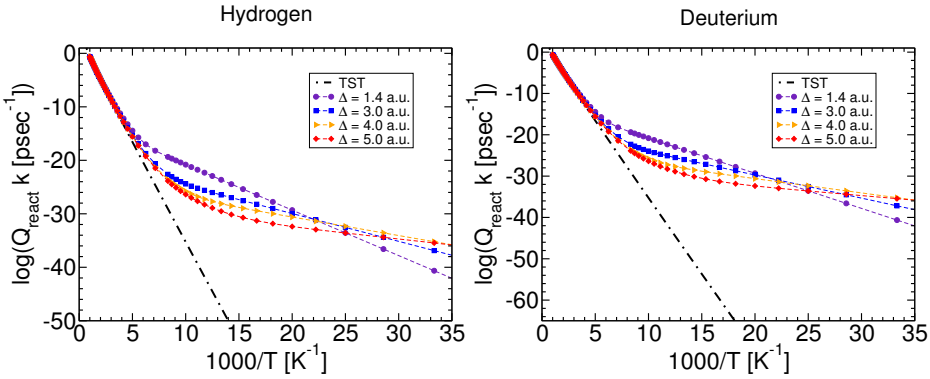

Figure 7.1.5: Thermal rate constant $\mathcal{Q}_{react}\,(T)\,k\,(T)$ for Hydrogen atoms (Left) and Deuterium isotopes (Right), varying the distance Δ between the barriers. Black-dashed curve is thermal rate constant $\mathcal{Q}_{react}\,(T)\,k\,(T)$ in the TST regime. Quantum effects are dominant for $T \lesssim 200$ K.

the two barriers Δ. Because Eq. (7.1.3) is dominated by resonant peaks at low temperatures (Sec. 5.4.1), on one hand, the thermal rate constant $k(T)$ get a fine amount increment any time a new quasi bound-state appears. On the other, greater values of Δ, unless a new quasi-bound state is found, has the only effect to further separate the two barriers, and to reduce the thermal rate constant. Hence, we expect that the seesaw behavior induced by increasing the distance between barriers and adding new quasi-bound states will generate "oscillations" in the thermal rate constant $k(T)$, as shown in Fig. (7.1.6). In particular, we can observe two distinct trends:

- Oscillations are wider for smaller Δ, where quasi-bound states are well separated.
- $\mathcal{Q}_{react}(T)\, k(T)$ converges to constant value in the limit of well separated barriers.

One can observe that these oscillations are present even at very high temperature, where TST predicts a larger thermal rate constant. The reason is simple: if at high temperature $k_B T \gtrsim V_0$ classical particles can easily cross the double barrier potential, instead quantum particles may undergo to quantum reflections, which reduces the thermal rate constant $k(T)$. In conclusions, the presence of resonant peaks combines with the quantum reflection, are responsible for the oscillations of $k(T)$.

Finally, Fig. (7.1.7) shows the thermal rate constant $k(T)$ as a function of both the temperature T and the distance between barrier Δ. As one can see, $k(T)$ is strongly and non trivially influenced by the resonant tunneling at low temperature and by resonant reflection at high temperatures.

7.2 Inverse Isotopic Effect

In the previous Section, we have studied the effect of the resonant tunneling for the thermal rate constant $k(T)$, by varying the distance Δ between the two barriers. In particular, we observed the presence of "oscillations" of $k(T)$ induced by the variation of the number of resonant peaks as Δ is increased. As shown in Fig. (7.1.6), oscillations for different isotopes have not only different amplitudes but also different frequencies. In particular, for a given Δ and temperature T, heavier isotopes have more resonant peaks than lighter isotopes and then a greater oscillation frequency. In Fig. (7.2.1) we reported the ratio between the thermal rate constants of Hydrogen atoms and Deuterium isotopes, defined as ratio $= \frac{[\mathcal{Q}_{react}(T)k(T)]_H}{[\mathcal{Q}_{react}(T)k(T)]_{^2H}}$, by varying Δ. One can observe that, even at high temperatures where TST gives a good approximation to the thermal rate constant $k(T)$ for both Hydrogen and Deuterium, it is possible to observe oscillations induced by the resonant tunneling (recall that TST predicts a ratio equals to one according to Eq. (7.1.4)). In particular, for sufficiently high temperature, the thermal rate constant $k(T)$ for the

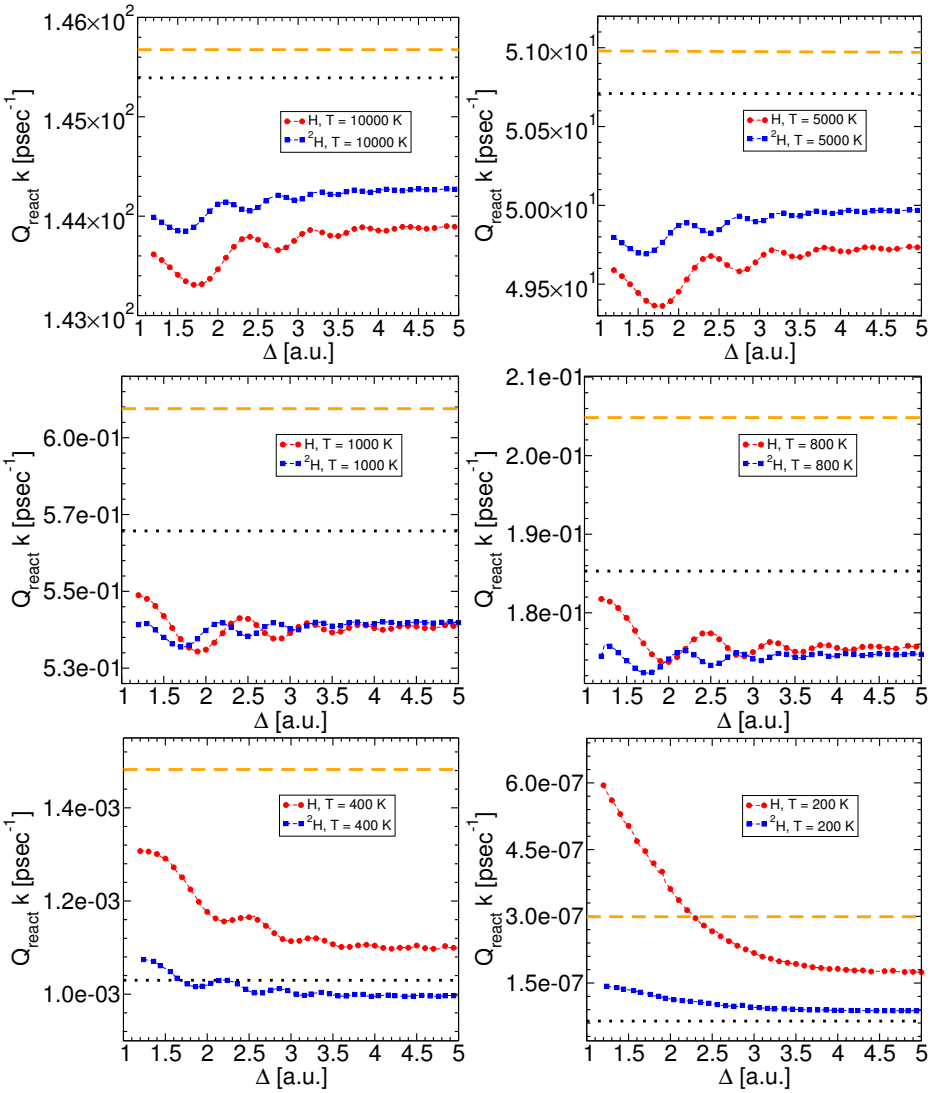

Figure 7.1.6: Comparison between the thermal rate constants $\mathcal{Q}_{react}\left(T\right)k\left(T\right)$ for Hydrogen atoms (H, circled-red curves) and Deuterium isotopes (^{2}H, squared-blue curve), at different temperatures. As described in the main text, oscillations are the direct results of the resonant tunneling phenomenon. Black-dotted and dashed-orange curves are respectively the value of the thermal rate constant $\mathcal{Q}_{react}\left(T\right)k\left(T\right)$ using the TST and a single Eckart barrier of the form $V\left(x\right)=\frac{V_0}{\cosh^2(x)}$ and $m=1.834\times10^3$ a.u.

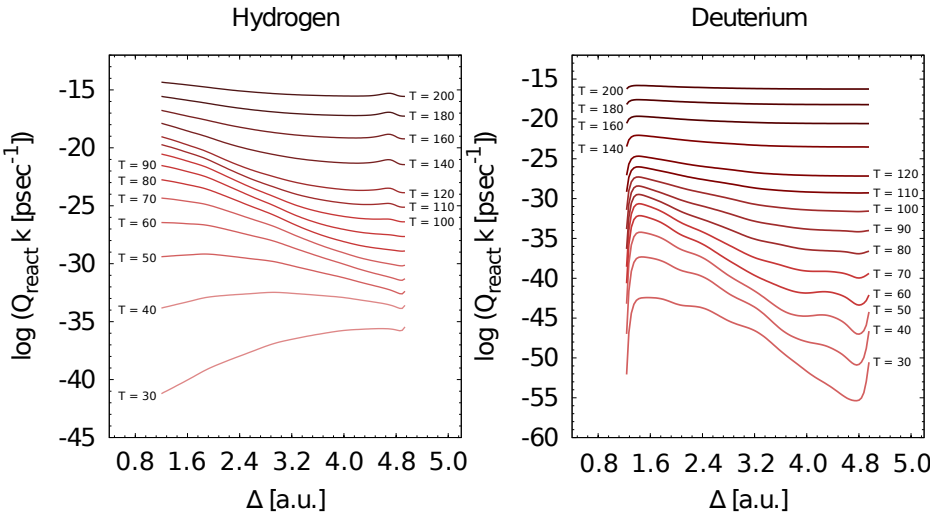

Figure 7.1.7: Thermal rate constant $\mathcal{Q}_{react}(T)\,k(T)$ for Hydrogen atoms (Left) and Deuterium isotopes (Right), varying both temperature T (expressed in Kelvin) and distance between the two barriers Δ. Figures show that the thermal rate constants $\mathcal{Q}_{react}(T)\,k(T)$ for both Hydrogen atoms and Deuterium isotopes are strongly and non trivially influenced by the resonant tunneling at low temperature.

heavier isotope results to be larger than $k(T)$ of the lighter one: this is an example of "Inverse Kinetic Isotope Effect". We have found that this important effect can be observed for one-dimensional systems exclusively if all the resonant states are taking into account with an accurate amount of precision.

In order to understand the origin of such a phenomenon, we will study how transition probabilities change at the variation of the distance between the two barriers Δ. For $\Delta \approx 0$, no quasi-bound states are present. Then, by increasing Δ, new quasi-bound states start to appear (Fig. (7.2.2)). By looking at Fig.(7.2.1) for the Δ intervals where the isotope effect is inverted as showed in Fig.(7.2.2), we can conclude that the inversion is induced by the greater resonant peak numbers given by the heavier isotope with respect to the lighter one. In other words, when the percentile peak number difference is increased, the deuterium transmission might be favored respect to the hydrogen one. This is the case of small distances Δ, where the percentage variation in the peaks number is more significant. Instead, by pushing the barriers far away, the percentage difference decreases and the inversion isotope effects is quenched. This inversion occurs only in the region where neither tunneling or classical transmission are predominant. Thus, we can assert that the type of quantum reflection generated by a second barrier is actually doing the job of inverting the isotope effects.

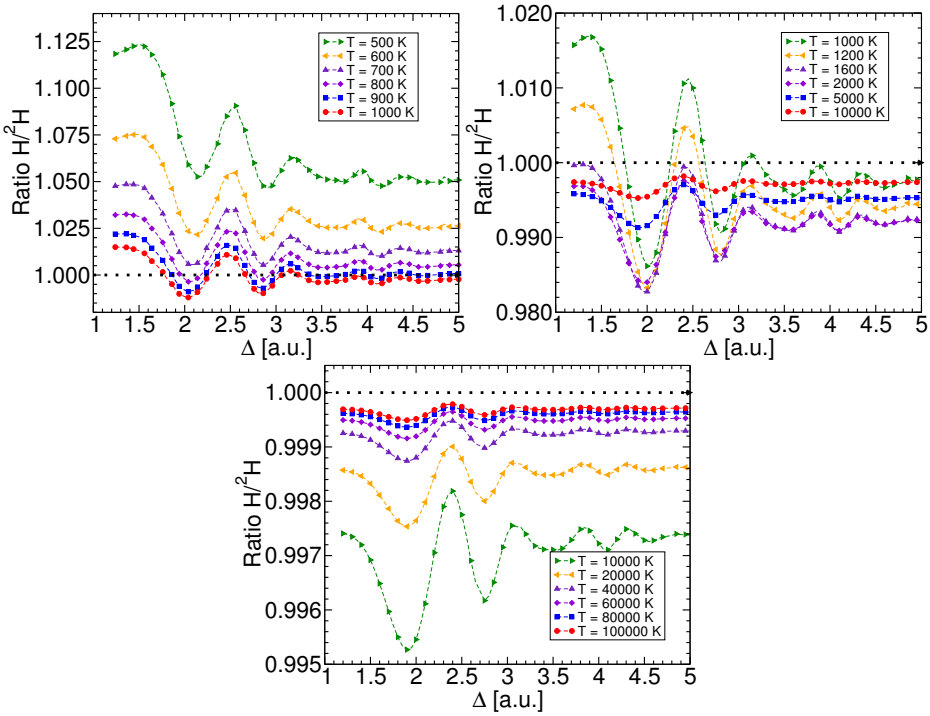

Figure 7.2.1: Ratio between the thermal rate constants of Hydrogen atoms and Deuterium isotopes, defined as Ratio $= \frac{[\mathcal{Q}_{react}(T)k(T)]_H}{[\mathcal{Q}_{react}(T)k(T)]_{^2H}}$. Even at high temperature, where TST gives a good approximation for the thermal rate constants $\mathcal{Q}_{react}\,(T)\,k\,(T)$ for both Hydrogen and Deuterium (see Fig. (7.1.5)), it is possible to observe resonance oscillations induced by the resonant tunneling and the so called "Inverse Isotope Effect" for sufficiently high temperatures. Then one can observe that TST predicts a ratio equals to one (black-dotted line), for any value of the temperature T and distance between barriers Δ.

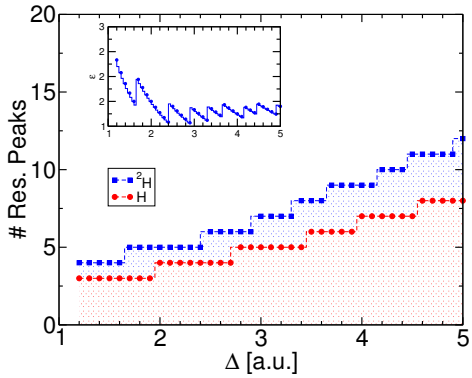

Figure 7.2.2: Number of resonant peaks by varying the distance between the barriers Δ. (Inset) The ratio between the difference in number of peaks over the number of peaks of the lightest isotope $\epsilon = \frac{\#_{^2H} - \#_H}{\#_H}$ is shown.

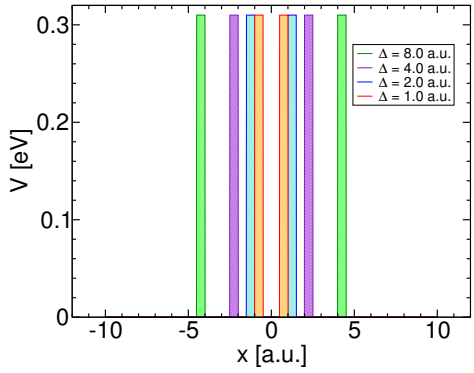

Figure 7.3.1: Potential profiles of Eq. (7.3.1), varying the distance of the two rectangular barriers Δ.

7.3 An Analytic example: the Double Rectangular Barrier Potential

In the previous Section, we showed that increasing the distance between two barriers in a double Eckart barrier potential, two important phenomena can be observed: the oscillation of the thermal rate constant $k\left(T\right)$ (as in Fig. (7.1.6)) and the inverse kinetic isotope effect, for which the heaviest isotope has a larger thermal rate constant than the lightest isotope (Fig. (7.2.1)). In this Section, we will show that this inversion is independent of the profile of the double barrier potential. In particular, we will compare the results for the double Eckart barrier potential in Eq. (7.1.1) with a double rectangular barrier potential

$$V\left(x\right)=V_{0}\left[\theta\left(x+\frac{\Delta}{2}+\delta\right)-\theta\left(x+\frac{\Delta}{2}\right)\right]+V_{0}\left[\theta\left(x-\frac{\Delta}{2}\right)-\theta\left(x-\frac{\Delta}{2}-\delta\right)\right], \tag{7.3.1}$$

where $V_{0}=0.310$ eV, $\delta=0.5$ a.u. is the width of the rectangular barrier, $\theta\left(\cdot\right)$ is the Heaviside theta and Δ is the distance between the two rectangular barriers (Fig. (7.3.1)), for which an analytic expression of the transmission probability $T\left(E\right)$ is known (Eq. (5.2.2)). For the integration of the transmission probability $T\left(E\right)$ in Eq. (7.1.3), we used the energy range $E\in\left[2.72\times10^{-4}\text{ eV},\,27.211\text{ eV}\right]$, with an energy step $\Delta E=2.72\times10^{-4}$ eV. Below and above the energy range, we set $T\left(E\right)$ respectively to zero and one. In this case, we used such a large energy upper-bound due to the strong quantum reflection that this system presents even at very high temperature, probably due to its first derivative discontinuity. As shown in Figs. (7.3.2, 7.3.3), these parameters are optimal for the temperature and the distances between the two barrier we considered in this Section.

In Fig. (7.3.4), thermal rate constants $\mathcal{Q}_{react}\left(T\right)$ $k\left(T\right)$ for different temperatures are shown. As for the double Eckart barrier potential, we observe oscillations of the thermal rate constant. The frequency of the oscillation is given by the different number of resonant

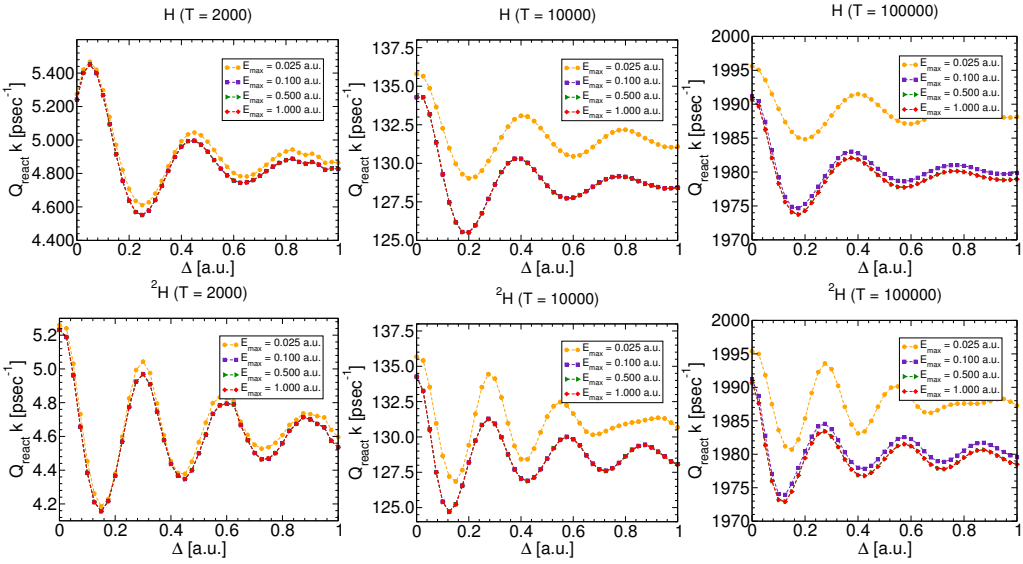

Figure 7.3.2: Thermal rate constant $\mathcal{Q}_{react}\,(T)\;k\,(T)$ varying the upper-bound cutoff E_{max}, at fixed $\Delta E = 2.72 \times 10^{-4}$ eV. As expected, the error is larger for higher temperature.

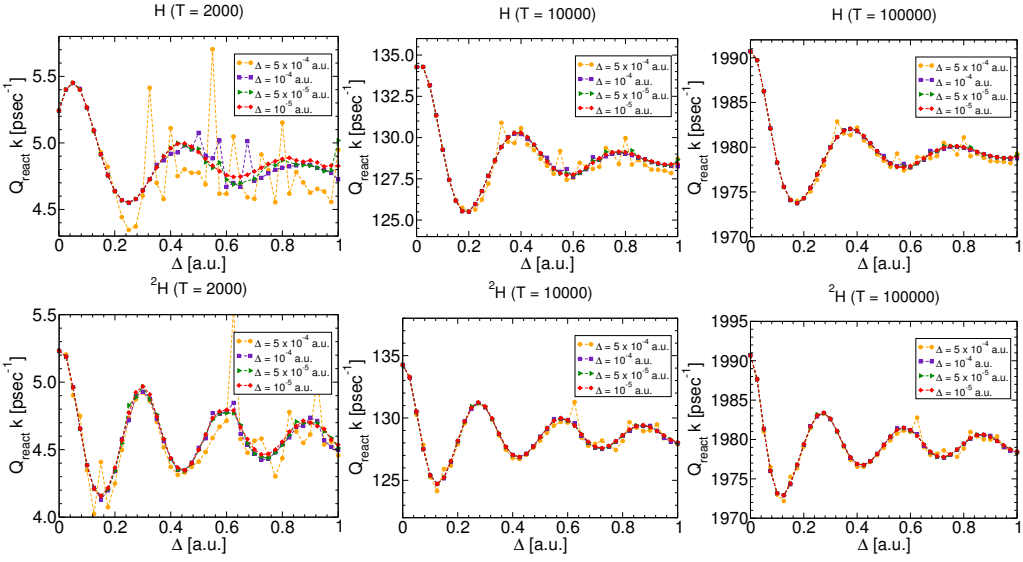

Figure 7.3.3: Thermal rate constant $\mathcal{Q}_{react}\,(T)\;k\,(T)$ by varying the energy integration step ΔE, at fixed $E_{max} = 27.211$ eV. As expected, errors are larger for smaller temperatures at a given energy interval, due to the presence of the resonant peaks in the transmission probabilities $T\,(E)$ in the low-energy region.

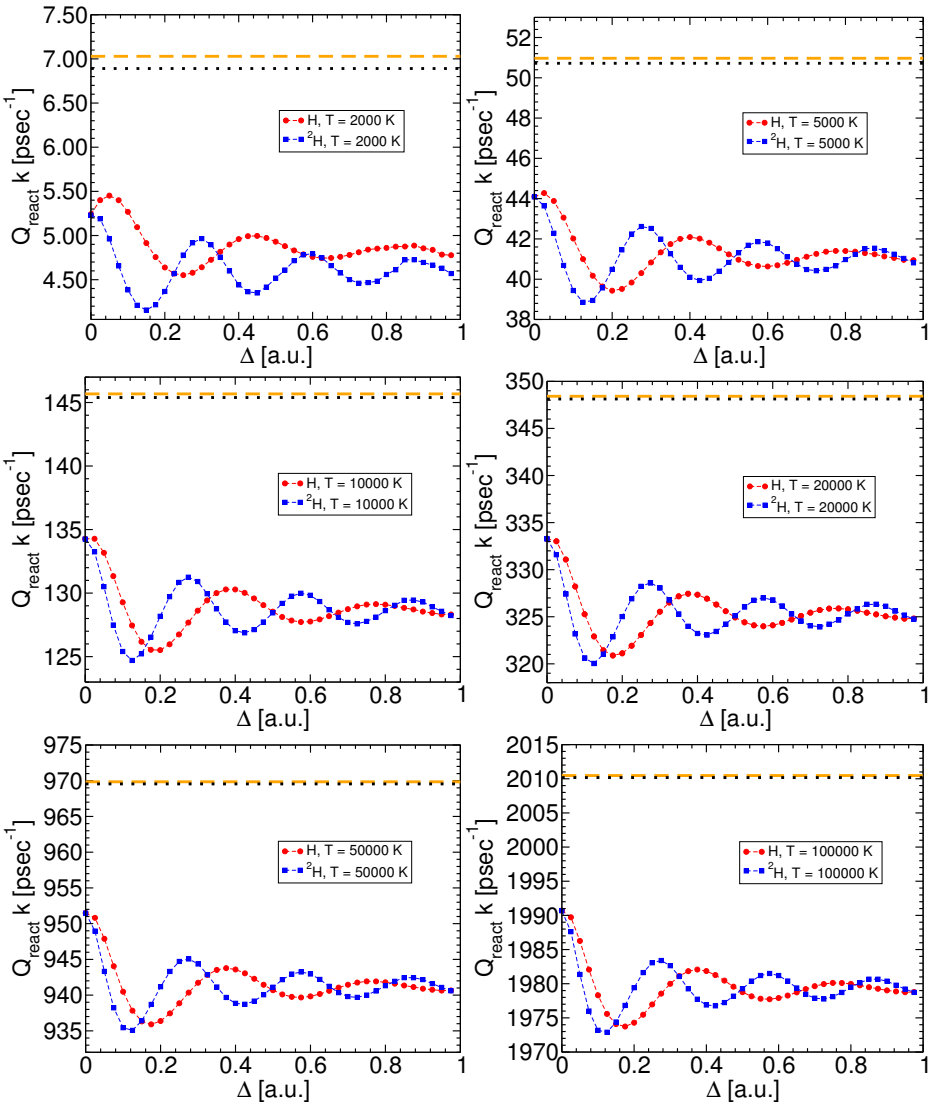

Figure 7.3.4: Comparison between the thermal rate constants $\mathcal{Q}_{react}\left(T\right)k\left(T\right)$ for Hydrogen atoms (H, circled-red curves) and Deuterium isotopes (^{2}H, squared-blue curve), at different temperatures, for the double rectangular barrier potential in Eq. (7.3.1). Similarly to the case of a double Eckart barrier potential as in Eq. (7.1.1), oscillations are the direct results of the resonant tunneling phenomenon. Black-dotted and dashed-orange curves are respectively the value of the thermal rate constant $\mathcal{Q}_{react}\left(T\right)k\left(T\right)$ using the TST and a single Eckart barrier of the form $V\left(x\right)=\frac{V_0}{\cosh^2(x)}$ and $m=1.834\times10^3$ a.u.

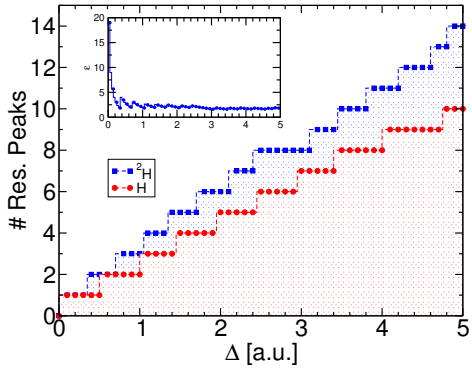

Figure 7.3.5: Number of resonant peaks by varying the distance between the barriers Δ for the double rectangular barrier potential in Eq. (7.3.1). (Inset) The ratio between the difference in number of peaks over the number of peaks of the lightest isotope $\epsilon = \frac{\#_{^2H} - \#_H}{\#_H}$ is shown.

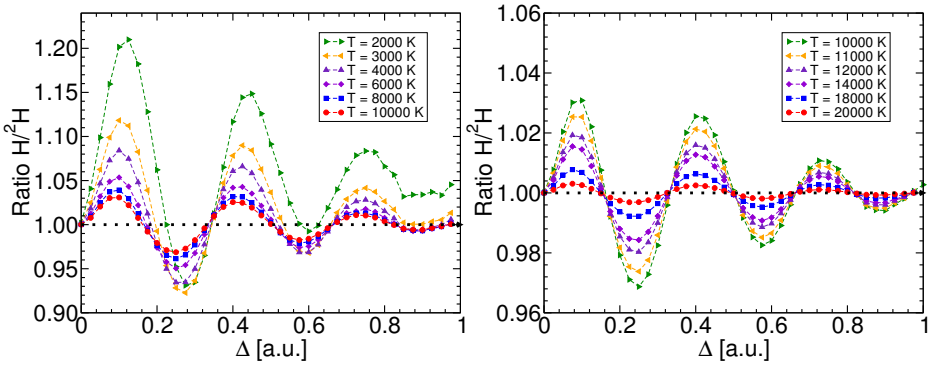

Figure 7.3.6: Ratio between the thermal rate constants of Hydrogen atoms and Deuterium isotopes, defined as ratio $= \frac{[\mathcal{Q}_{react}(T)k(T)]_H}{[\mathcal{Q}_{react}(T)k(T)]_{^2H}}$. As in the case of the double Eckart barrier potential in Eq. (7.1.1), even for the double rectangular barrier potential in Eq. (7.3.1) it is possible to observe resonance oscillations induced by the resonant tunneling and the so called "Inverse Kinetic Isotope Effect".

peaks between the two isotopes varying the distance between the two rectangular barrier (Fig. (7.3.5)).

Finally, Fig. (7.3.6) shows the ratio between the thermal rate constants of the two isotopes. In particular, even for the double rectangular barrier potential in Eq. (7.3.1) we numerically observe the inverse isotope effect. There results confirm what we observed in the previous Section for a (more realistic) double Eckart barrier potential.

Conclusions

This thesis presents a new method to calculate thermal rate constants $k\,(T)$ for one dimensional scattering potentials in the presence of many quasi-bound states. In particular this novel methodology can be applied to the case of multiple-barrier passages where quasi-bound states are present. After showing that thermal rate constants can be calculated from asymptotic conditions, the Schrödinger equation has been solved as an ordinary differential equation, with the energy as a fixed parameter, by choosing convenient boundaries conditions. The method we propose is time-independent and it provides a significant advantage over any available time-dependent method for the calculation of rate constants in the presence of resonance states. We have shown this by calculating $k(T)$ for arbitrary potentials, even for first-derivative discontinuous potentials as well as the double barrier potential with several quasi-bound states. In both cases, the error respect to the exact expression was less than 1% even at extremely low temperatures. Possible multidimensional implementations of the method are under way in our group. In multidimensional applications overlapping resonances will most probably occur. We think that one can deal with this issue by a convolution of Breit-Wigner distributions where the centers and the width are fitted to the shape the transmission probability profile. This method has recently been published [35].

As a first application of our method, we studied how Helium isotopes might be separated by resonant tunneling in a double layer Polyphenylene system (2D-PP, Fig. (6.1.1)). The double layer Polyphenylene acts as a filter for the Helium isotopes and its double barrier profile is shown in Fig. (6.1.2). The potential in Fig. (6.1.2) was obtained experimentally by ab-initio calculation, thanks to our collaboration with A. M. Brockway and J. Schrier (Department of Chemistry, Haverford College, Haverford (PA), USA). Due to the presence of resonant states given by the double barrier potential, the 2D-PP filter was

able to select between ^{3}He from ^{4}He, even at relatively high temperatures (Fig. (6.2.5)). We showed how this occurs by simulations using our method for rate calculations. A paper with all the material presented in Chap. 6 is in preparation.

Finally, we used our method to extensively study the effects of resonant tunneling on the thermal rate constants for double barrier potentials. In particular, we numerically observed two important phenomena: the "oscillation" of the thermal rate constant as a function of the distance between the two barriers (Fig. (7.1.6)), and the "Inverse Kinetic Isotope Effect" where heavier isotope gains a larger thermal rate constant with respect to the lightest isotope (Fig. (7.2.1)). The inverse kinetic isotope effect can be explained considering the different contribution of the resonant peaks to the thermal rate constant in the low-temperature region versus the high-temperature region. In the low temperature region, the thermal rate constant is dominated by the contribution of a few peaks (see Sec. 5.4.1 for details). Therefore, deep resonant tunneling favors the lighter isotope with respect to the heavier isotope. On the contrary, in the high-temperature region, all resonant peaks contribute to the thermal rate constant: hence the heaviest isotope, which present more resonant states than the lightest isotope at fixed distance between the two barriers (Fig. (7.2.2)), has a larger thermal rate constant than the lightest isotope. The inverse kinetic isotope effect might be used to experimentally connote direct tunneling versus shallow tunneling and quantum reflection. It is important to note that all the results presented in Chap. 7 were possible thanks to our ODE method numerical robustness.

In conclusion, this thesis presents a new numerical method for studying resonant tunneling from a time-independent point of view. The method can be applied to arbitrarily complex one dimensional potentials at any temperature, avoiding the numerical convergence issues which occur in the time-dependent case. It is thus one of the first tools available to accurately and rapidly assess reaction rates in the low temperature regime in the presence of many quasi bound states. The extension to higher dimensions is in progress.

Future Perspectives: Computation of the Thermal Rate Constant on Quantum Computers

In this thesis, we presented a fast and robust method for computing thermal rate constant in extreme conditions (the ODE method, Sec. 4.2), where deep resonant tunneling dominates. In particular, we used a time-independent approach (Sec. 2.2), which results much faster and more stable than a time-dependent approach (Sec. 2.1). As examples, we considered two case studies where resonant tunneling plays a fundamental role: the isotope selection by a double barrier potential (Chap. 6) and the kinetic isotope effect (Chap. 7).

Even if the time-independent ODE method is not numerically demanding and its computational complexity scales only as $\mathcal{O}\left(\alpha N^2\right)$, where $N = \frac{L}{\Delta x}$ is the linear grid size and α is a constant which depends on the used method (see Sec. 4.2 for details), for multiple barrier potentials supporting several resonant states N can grows quickly. Hence, the computation of the thermal rate constant might result unfeasible even for our ODE method.

In 1982, Feynman conjectured for the first time the possibility to use the quantum mechanics for "quantum computation" [96], taking advantage of phenomena like the linear superposition of quantum states and the quantum entanglement for an exponential speed-up with respect to classical computers. However, it was only in 1991 that a seminal work by Lloyd [97] proved that quantum computers can be programmed to simulate any local quantum system. An exponential growing interest of the scientific community started since on. Therefore, many quantum algorithms have been proposed to simulate quantum systems [98–104] which have an exponential speed-up with respect to any equivalent classical algorithm. More importantly, in the last few years, the first quantum

devices with quantum capabilities have been devised [105–108], showing that quantum computing is not merely an academic exercise.

In the rest of this Chapter, we will outline a "quantum" ODE method to take advantage of the computational potentiality of quantum computers.

7.4 Brief Introduction on Quantum Computation

In order to set up a problem on a quantum computer, it is necessary to introduce quantum *registers* $|\mathbf{b}\rangle$ of ν *q-bits* (two-level systems). These registers will be used for both quantum computation and storing information. Unlike classical registers whose bits can assume only two value, zero and one, any of the q-bit in a quantum register can be in a superposition of states

$$|b_i\rangle = a_i\,|0_i\rangle + b_i\,|1_i\rangle\,, \tag{7.4.1}$$

where $|a|^2 + |b|^2 = 1$. Initially, a quantum register $|\mathbf{b}\rangle$ is in a direct product of all the q-bits

$$|\mathbf{b}\rangle = \bigotimes_{i=0}^{\nu-1} |b_i\rangle\,. \tag{7.4.2}$$

Allowed operations on quantum registers are all the *unitary transformation* (corresponding to propagation of the register) and *measurement*. In particular, the last operation causes the collapse of the quantum register onto one of the subspaces of the full Hilbert space. By convention, unitary operations (**quantum gates**) should be explicitly given as operations on one or (at most) two q-bits. In fact, most of the quantum gates that can be constructed in practice involves no more than two q-bit at time. Starting from an early work of Deutsch [109], it has been proven that the set of all the single q-bit operations (formally the $U\,(2)$ group), in addition with the *controlled-not* (CNOT) which acts on two q-bits

$$|b_0\rangle \otimes |b_1\rangle \mapsto |b_0\rangle \otimes \left|(b_0 + b_1)_{\mathrm{mod}\,2}\right\rangle, \tag{7.4.3}$$

form an universal set of quantum gates [110–112], i.e. any arbitrary large unitary transformation can be represented as operations on one or two q-bits. Similar to classical computers, the computational complexity of quantum computers can be defined as the number of quantum gates used in the quantum algorithm [113]. In Fig. (7.4.1), examples of CNOT gates are shown in terms of quantum circuits, i.e. linear representations of quantum gates applied to quantum registers. In order to simplify quantum circuits, some common operations are given as unitary gates. For example, the Hadamard transformation

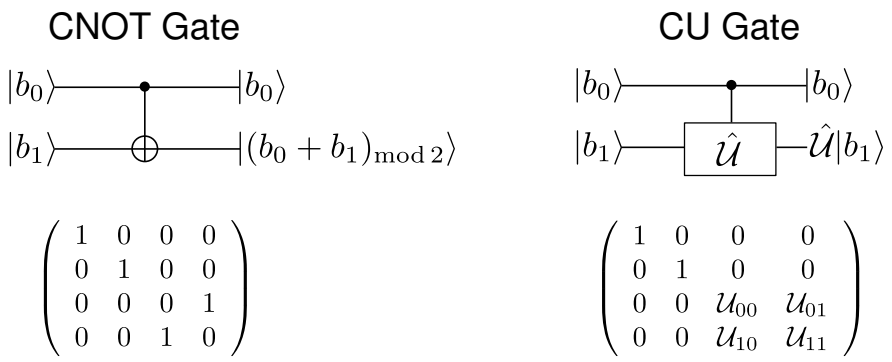

Figure 7.4.1: Examples of quantum circuits for a *controlled-not* gate (left) and *controlled-U* gate (Right). In both cases, the unitary transformation is applied on the second q-bit only if the first q-bit is in the state $|1\rangle$.

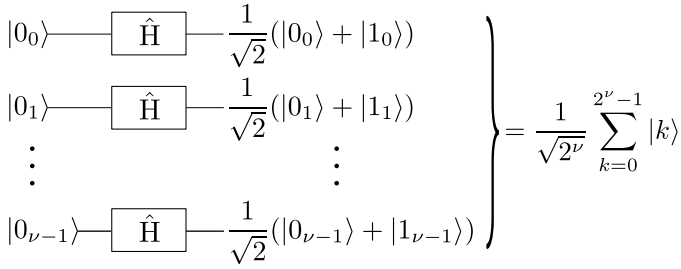

Figure 7.4.2: Example of quantum circuit for obtaining a quantum superposition of all the states starting from the initial quantum state $|\mathbf{0}\rangle = \bigotimes_{i=0}^{\nu-1} |0\rangle$. $\hat{\mathrm{H}} = \frac{1}{\sqrt{2}} \begin{pmatrix} 1 & 1 \\ 1 & -1 \end{pmatrix}$ is the Hadamard operator. Here, $|k\rangle = |k_0\rangle \otimes |k_1\rangle \otimes \cdots \otimes |k_{\nu-1}\rangle$ is the bit-representation of the integer k.

$$\hat{\mathrm{H}} = \frac{1}{\sqrt{2}} \begin{pmatrix} 1 & 1 \\ 1 & -1 \end{pmatrix}, \tag{7.4.4}$$

which is typically used for obtaining a quantum superposition of all the states

$$\begin{aligned} \hat{\mathrm{H}}_1 \hat{\mathrm{H}}_2 \cdots \hat{\mathrm{H}}_\nu |\mathbf{0}\rangle &= \bigotimes_{i=0}^{\nu-1} \left(\hat{\mathrm{H}}_i |0_i\rangle \right) \\ &= \frac{1}{\sqrt{2^\nu}} \bigotimes_{i=0}^{\nu-1} (|0_i\rangle + |1_i\rangle) \\ &= \frac{1}{\sqrt{2^\nu}} \sum_{k=0}^{2^\nu-1} |k\rangle \,, \end{aligned} \tag{7.4.5}$$

where $|k\rangle = |k_0\rangle \otimes |k_1\rangle \otimes \cdots \otimes |k_{\nu-1}\rangle$ is the bit-representation of the integer k. Fig. (7.4.2) shows the explicit quantum circuit of the Hadamard transformation in Eq. (7.4.5). Another

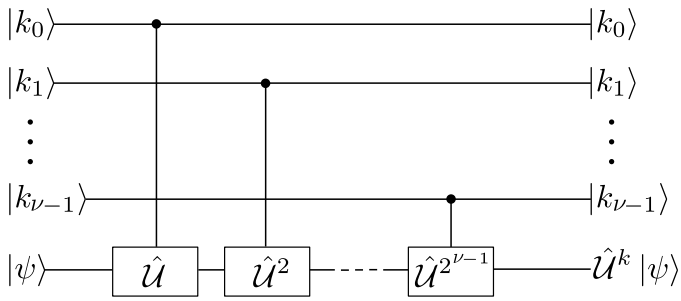

Figure 7.4.3: Example of quantum circuit used for the implementation of the unitary transformation $|k\rangle \otimes |\psi\rangle \mapsto |k\rangle \otimes \left(\hat{\mathcal{U}}^k |\psi\rangle\right)$.

important unitary transformation commonly used in quantum computer is the application to the register of powers of unitary operators $\hat{\mathcal{U}}$ of the form [114, 115]

$$|k\rangle \otimes |\psi\rangle \mapsto |k\rangle \otimes \left(\hat{\mathcal{U}}^k |\psi\rangle\right), \tag{7.4.6}$$

where $|\psi\rangle$ is a second quantum register. It is important to observe that k is not a given parameter but it is given by the actual state of the quantum register. Recalling that $|k\rangle = |k_0\rangle \otimes |k_1\rangle \otimes \cdots \otimes |k_{\nu-1}\rangle$, we have

$$\begin{aligned} \hat{\mathcal{U}}^k &= \hat{\mathcal{U}}^{k_0 2^0 + k_1 2^1 + \ldots + k_{\nu-1} 2^{\nu-1}} \\ &= \hat{\mathcal{U}}^{k_0 2^0} \hat{\mathcal{U}}^{k_1 2^1} \cdots \hat{\mathcal{U}}^{k_1 2^1}. \end{aligned} \tag{7.4.7}$$

Therefore, as shown in Fig. (7.4.3), it is possible to implement the transformation in Eq. (7.4.6) simply using CNOT gates. Observe that the quantum circuit represented in Fig. (7.4.3) requires only a number of $\mathcal{O}(\nu)$ gates.

7.5 Time-Dependent approach

The idea to use quantum computers for the calculation of thermal rate constants was firstly used by Lidar and Wang in 1999 [116]. Their idea consists in finding a quantum algorithm that calculates the spectrum $\omega_n = \epsilon_n/\hbar$ and the position probability for any relevant eigenstate $|n\rangle$ of the Schrödinger equation

$$\hat{\mathcal{H}} |n\rangle = \epsilon_n |n\rangle, \tag{7.5.1}$$

in order to quickly compute the flux-flux auto-correlation function

$$C_{ff}\left(t,\,T\right)=\sum_{m,\,n}e^{-\frac{\tilde{\beta}}{2}\left(\omega_n+\omega_m\right)}e^{-i\left(\omega_n-\omega_m\right)t}\,\left(\omega_n-\omega_m\right)^2\left|\chi_{nm}\right|^2, \tag{7.5.2}$$

where $\tilde{\beta}=\hbar\beta$ and $\chi_{nm}\equiv\langle n|\,\hat{\Theta}_p\,|m\rangle$ is the overlap between eigenstates in the product space (see Sec. 2.1 for more details). As described in their paper, they used a time-evolution algorithm which is mainly composed into three steps:

1. An appropriate initial state $|\mathbf{0}\rangle\otimes|\psi_0\rangle$ is prepared. The first register, or ancilla register, will be used for storing the eigenvalue, while the second register will be used for storing the eigenstate. For a faster convergence of the quantum algorithm, the initial state $|\psi_0\rangle$ must be a non-zero overlap with any relevant eigenstate. The simplest choice consists in initializing $|\psi_0\rangle$ as an equal superposition of all the possible states.

2. $|\psi_0\rangle$ is propagated for a time t using the split-operator propagation scheme [117]. This part is exponentially faster than any equivalent classical algorithm [97].

3. The final state $|\mathbf{0}\rangle\otimes|\psi_0\rangle\mapsto\sum_n\xi_n\left(t\right)|\omega_n\rangle\otimes|n\rangle$ is measured using the "von Neumann measurement" trick [118] (see the original paper [116] for the description and derivation of $\xi_n\left(t\right)$). After that, the first register will contain the eigenvalue ω_n and the second register the eigenstate $|n\rangle$ with probability $p_n=\left|\xi_n\left(t\right)\right|^2$.

4. Repeat 1-3 many times until convergence is reached to the desire accuracy for all the relevant eigenstates. The number of required iterations is proportional to the desired accuracy.

5. Compute (classically) the flux auto-correlation function in Eq. (7.5.2) and the thermal rate constant as
$$k\left(T\right)\,\mathcal{Q}_{react}\left(T\right)=\int_0^{+\infty}dt\,C_{ff}\left(t,\,T\right) \tag{7.5.3}$$

In principle, the above quantum algorithm has an exponential speed-up given by the calculation on a quantum computer of the spectrum of the Hamiltonian $\hat{\mathcal{H}}$. However, as any time-dependent method, this quantum algorithm presents several problems:

1. The exponential speed-up is limited to the calculation of the spectrum of $\hat{\mathcal{H}}$. In particular, if a good guess of initial state $|\psi_0\rangle$ is not provided, the convergence in (4) might be never reached if many resonant states are present.

2. As shown in [119], the propagation t might be very large if resonant states are present.

3. The computation of $C_{ff}(t)$ in Eq. (7.5.2) must be done classically. Therefore, given N the number of relevant eigenstates, the computation of $C_{ff}(t)$ will scale as N^2.

4. More importantly, the calculation of thermal rate constant in Eq. (7.5.3) still remains a time-dependent calculation. Hence, all the problematic described in Sec. 2.1 will affect this quantum algorithm.

Therefore, in the next Section we will propose a quantum algorithm based on our ODE method for computing thermal rate constants.

7.6 Time-Independent approach

The main idea of our ODE method (Sec. 4.2) consists in solving the Schrödinger equation

$$\hat{H}\psi_p(x) = \left[-\frac{\hbar^2}{2m}\frac{d^2}{dx^2} + V(x)\right]\psi_p(x) = E\psi_p(x), \tag{7.6.1}$$

as an ordinary differential equation. In fact, because no bounded states exist, the spectrum of the Hamiltonian $\hat{\mathcal{H}}$ is continuous and then, an eigenstate must exist for any fixed energy $E = \frac{p^2}{2m}$. Therefore, it is possible to calculate the transmission (reflection) probability $T(E)$ ($R(E)$) as

$$T(E) = |t|^2 = 4\left|\psi_p(\tilde{x}) + \frac{\hbar}{i\,p}\partial_x\psi_p(\tilde{x})\right|^{-2}, \tag{7.6.2}$$

$$R(E) = |r|^2 = 1 - \left(1 + \frac{1}{4}\left|\psi_p(\tilde{x}) - \frac{\hbar}{i\,p}\partial_x\psi_p(\tilde{x})\right|^2\right)^{-1}, \tag{7.6.3}$$

where $\tilde{x}$ is an arbitrary point far away from the scattering region. Therefore, a good quantum algorithm must provide both the spectrum and eigenstates of the Hamiltonian $\hat{\mathcal{H}}$. In the classical case, we provided two methods for solving Eq. (7.6.1): the Numerov's method (Sec. 4.2.1) and the Runge-Kutta method (Sec. 4.2.2), both based on the propagation of an appropriate choice of the boundary conditions. As explained in Sec. 7.6.1, both methods have a computational complexity $\mathcal{O}(N^2)$. In the quantum case, we will exploit the quantum speed-up that quantum computers have for solving any local quantum Hamiltonian [97]. In particular, we will use the "Quantum Phase Estimation" algorithm [115], which is a method for approximating eigenvalues of unitary matrices. It was recently used for solving linear system on quantum computers with an exponential speed-up [120–122].

In the next Sections, we will outline the idea of the time-independent quantum ODE and its application on the calculation thermal rate constants.

7.6.1 Quantum Phase Estimation

As for any quantum algorithm, it is necessary to provide an initial states. In this case, we set the initial state as

$$|\Phi\rangle = |\mathbf{0}\rangle \otimes |\phi\rangle = |\mathbf{0}\rangle \otimes \sum_p d_p \, |\psi_p\rangle \,, \tag{7.6.4}$$

where $|\mathbf{0}\rangle = \bigotimes_{i=0}^{\nu-1} |0_i\rangle$ (ν is the number of *ancilla* q-bits necessary for representing eigenvalues), $|\psi_p\rangle$ are eigenstate of the Hamiltonian in Eq. (7.6.1) and

$$d_p = \langle \phi | \psi_p \rangle \,. \tag{7.6.5}$$

By application of an Hadamard transformation on the first register

$$\begin{aligned} \hat{\mathrm{H}}_1 \hat{\mathrm{H}}_2 \cdots \hat{\mathrm{H}}_\nu \, |\mathbf{0}\rangle &= \bigotimes_{i=0}^{\nu-1} \left(\hat{\mathrm{H}}_i \, |0_i\rangle \right) \\ &= \frac{1}{\sqrt{2^\nu}} \bigotimes_{i=0}^{\nu-1} \left(|0_i\rangle + |1_i\rangle \right) \\ &= \frac{1}{\sqrt{2^\nu}} \sum_{k=0}^{2^\nu - 1} |k\rangle \,, \end{aligned} \tag{7.6.6}$$

the initial quantum state $|\Phi\rangle$ can be transformed to

$$|\Phi\rangle \mapsto |\Phi'\rangle = \frac{1}{\sqrt{2^\nu}} \sum_{k=0}^{2^\nu - 1} |k\rangle \otimes \left(\sum_E d_E \, |\psi_E\rangle \right) . \tag{7.6.7}$$

If $\hat{\mathcal{H}}$ is sparse and efficiently row computable with $\mathcal{O}(s)$, the unitary matrix $\hat{\mathcal{U}} = e^{i\,k\hat{\mathcal{H}}}$ can be computed in [97, 123]

$$\mathcal{O}\left(s \, 2^{2\nu} \log \, N \right) . \tag{7.6.8}$$

Therefore, the application of $\hat{\mathcal{U}}$ to $|\Phi'\rangle$ can be quickly performed on a quantum computer using controlled gates as in Fig. (7.4.3), giving the following result

$$\begin{aligned} |\Phi'\rangle \mapsto |\Phi''\rangle &= \frac{1}{\sqrt{2^\nu}} \sum_{k=0}^{2^\nu - 1} |k\rangle \, e^{i\,k\hat{\mathcal{H}}} \otimes \left(\sum_p d_p \, |\psi_p\rangle \right) \\ &= \frac{1}{\sqrt{2^\nu}} \sum_{k=0}^{2^\nu - 1} |k\rangle \otimes \left(\sum_p d_p e^{i\,kE} \, |\psi_p\rangle \right) \\ &= \sum_p d_p \left(\frac{1}{\sqrt{2^\nu}} \sum_{k=0}^{2^\nu - 1} e^{i\,kE} \, |k\rangle \right) \otimes |\psi_p\rangle \,, \end{aligned} \tag{7.6.9}$$

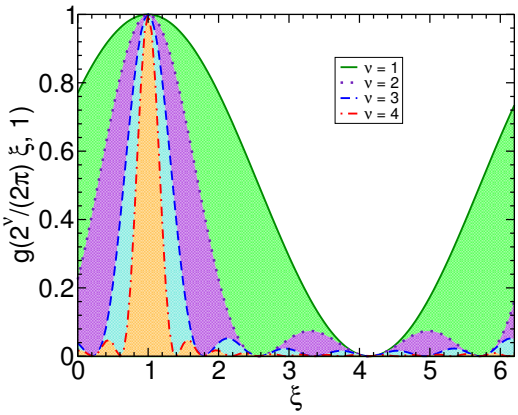

Figure 7.6.1: In this figure, $g\,(E,\,k)$ as defined in Eq. (7.6.11) is shown varying the number of ancilla q-bits ν. As one can see, $g\,(E,\,k)$ becomes peaked in $k = 2^{\nu}\,\frac{E}{2\pi}$ for sufficiently large ν.

where $E = \frac{p^2}{2m}$. The key of the quantum phase estimation algorithm is to apply a quantum Fourier transform (QFT) on the first register. As described in [115], QFT has an exponential speed-up on quantum computers with a computational complexity $\mathcal{O}\,(\log N\,\log\log N)$, where N is the number of states. Therefore, after the application of the QFT to first register, the quantum states $|\Phi''\rangle$ becomes

$$|\Phi''\rangle \mapsto |\Phi'''\rangle = \sum_p d_p \left(\sum_{k=0}^{2^{\nu}-1} g\,(E,\,k)\,|k\rangle \right) \otimes |\psi_p\rangle\,, \tag{7.6.10}$$

where

$$g\,(E,\,k) = \begin{cases} \frac{\sin\left[\pi\left(2^{\nu}\,\frac{E}{2\pi} - k\right)\right] e^{i\pi\left(\frac{E}{2\pi} - k\,2^{-\nu}\right)\left(2^{\nu}-1\right)}}{2^{\nu}\,\sin\left[\pi\left(\frac{E}{2\pi} - k\,2^{-\nu}\right)\right]} & 2^{\nu}\,\frac{E}{2\pi} \neq k \\ 1 & 2^{\nu}\,\frac{E}{2\pi} = k \end{cases}. \tag{7.6.11}$$

Hence, a measurement of the first register produces the outcome k with probability

$$p_k = \sum_p |d_p|^2\,|g\,(E,\,k)|^2\,, \tag{7.6.12}$$

and then, the second register will collapse to the state

$$\sum_p \frac{d_p\,g\,(E,\,k)}{\sqrt{p_k}}\,|\psi_k\rangle\,. \tag{7.6.13}$$

As shown in Fig. (7.6.1), for sufficiently large number of ancilla q-bits ν, $g\,(E,\,k)$ is peaked

around $k = \frac{2^\nu E}{2\pi}$. Therefore, Eq. (7.6.10) can be simplified as

$$|\Phi'''\rangle = \sum_p d_p \, |E\rangle \otimes |\psi_p\rangle \, . \tag{7.6.14}$$

Observe that the computational complexity for computing the final state $|\Phi'''\rangle$ in Eq. (7.6.14) scales as $\mathcal{O}\left(s\, 2^{2\nu} \log N\right)$, which results faster than any equivalent classical algorithm. However, $|\Phi'''\rangle$ is the superposition of all pairs of eigenvalues and its eigenstates, weighted by the overlap $d_p = \langle \psi_p | \phi_0 \rangle$ of the eigenstate $|\psi_p\rangle$ with the initial state $|\phi_0\rangle$. In the next Section, we will show how an appropriate choice of the initial condition $|\phi_0\rangle$ can be used for selecting eigenstates in Eq. (7.6.14).

7.6.2 Quantum ODE Algorithm

As explained in Sec. 4.2, the ODE method is based on the propagation of an appropriate choice of boundary conditions. Similarly, we will show that for the "Quantum ODE" algorithm, the choice of initial states $|\phi_0\rangle$ results to be fundamental. As shown in the previous Section, the quantum phase estimation algorithm maps an initial states $|\mathbf{0}\rangle \otimes |\phi_0\rangle$ to

$$|\mathbf{0}\rangle \otimes |\phi_0\rangle \mapsto \sum_p d_p \, |E\rangle \otimes |\psi_p\rangle \, , \tag{7.6.15}$$

where $E = \frac{p^2}{2m}$ and

$$d_p = \langle \phi | \psi_p \rangle \, . \tag{7.6.16}$$

In order to compute the transmission probability $T\,(E)$ using the expression in Eq. (7.6.2), it is necessary to extract only the specified eigenstate with the correct moment $p = \sqrt{2m\,E}$. The main idea is to set the initial quantum state $|\phi_0\rangle$ as

$$|\phi_{p'}\rangle = \frac{1}{\sqrt{2\pi\hbar}} \int_{-\infty}^{0} dx \, e^{ip'x/\hbar} \, |x\rangle \, , \tag{7.6.17}$$

where p' is a given parameter. $|\phi_{p'}\rangle$ can be obtained by an appropriate unitary transformation [114, 115]. An explicit example for a three q-bits system is given in Fig. (7.6.2). Hence, using the scattering representation for eigenstates $|\psi_p\rangle$ of the Hamiltonian in Eq. (7.6.1)

$$\left\langle x | \psi_p^R \right\rangle = \psi_p^R\,(x) = \begin{cases} \frac{1}{\sqrt{2\pi\hbar}} \left(\mathrm{e}^{ipx/\hbar} + r\, \mathrm{e}^{-ipx/\hbar} \right) & x \ll -L_{\mathcal{S}} \\ \frac{1}{\sqrt{2\pi\hbar}} t\, \mathrm{e}^{ipx/\hbar} & x \gg +L_{\mathcal{S}} \end{cases} , \tag{7.6.18a}$$

$$\left\langle x | \psi_p^L \right\rangle = \psi_p^L(x) = \begin{cases} \frac{1}{\sqrt{2\pi\hbar}} t\, \mathrm{e}^{-ipx/\hbar} & x \ll -L_{\mathcal{S}} \\ \frac{1}{\sqrt{2\pi\hbar}} \left(\mathrm{e}^{-ipx/\hbar} - r\, \mathrm{e}^{ipx/\hbar} \right) & x \gg +L_{\mathcal{S}} \end{cases} , \tag{7.6.18b}$$

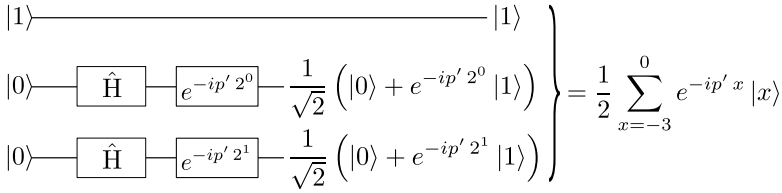

Figure 7.6.2: In this figure, an explicit example of quantum circuit for the unitary transformation $|\mathbf{0}\rangle \mapsto \frac{1}{\sqrt{2\pi\hbar}}\int_{-\infty}^{0} dx\, e^{ip'x/\hbar}|x\rangle$ using three q-bits. Here, the first q-bit represents the sign.

where $|x| \gg L_{\mathcal{S}}$ represents positions far away from the scattering region, we obtain

$$\left|d_p^R\right|^2 = \left|\langle\phi_{p'}|\psi_p^R\rangle\right|^2 \approx \delta\left(p-p'\right), \tag{7.6.19a}$$

$$\left|d_p^L\right|^2 = \left|\langle\phi_{p'}|\psi_p^L\rangle\right|^2 \approx 0. \tag{7.6.19b}$$

Therefore, using the appropriate initial condition $|\phi_{p'}\rangle$ as in Eq. (7.6.17), the measurement of the first register will produce outcome $E = \frac{p'^2}{2m}$ with high probability, and consequently the second register will collapse to the corresponding eigenstate. Unlike the "classical" ODE algorithm whose computational complexity is $\mathcal{O}\left(N^2\right)$, the "quantum" ODE (qODE) algorithm has a computational complexity $\mathcal{O}\left(N\,\log N\right)$. Moreover, unlike the time-dependent quantum algorithm described in [116], our qODE algorithm is totally time-independent and we expect that it will be numerical robust as the classical counterpart, even in presence of many metastable states.

APPENDIX A

Discrete Variable Representation (DVR)

In this appendix we describe how the DVR method can be employed in one dimension. For a rigorous theoretical description see [124] and references therein.

A.1 Basic idea of DVR methods

The idea of DVR (*Discrete Variable Representation*) is to solve the Schrödinger equation using a finite set of basis functions. The DVR method is a specific pseudo-spectral method employed to calculate matrix elements of the Hamiltonian operator [117]. One defines a spectral projection which is applied to the original Hamiltonian $\hat{\mathcal{H}}$ to arrive to a finite $n-dimensional$ Hilbert space in which the truncated Hamiltonian is a function of the projection operators. The projection operators are defined as $\hat{P}_n = \sum_i^n |\phi_i\rangle \langle\phi_i|$ where the basis $|\phi_i\rangle$ is the pseudo-spectral basis, i.e. a basis of spatially localized basis functions. Given a set of basis functions the equation which determines the expectation value of the energy for the system is

$$\int_{-\infty}^{+\infty} \psi^{\star}(x)\ \hat{\mathcal{H}}\,\psi(x)\,dx = E. \tag{A.1.1}$$

The wave function ψ is a linear combination of the n basis set functions $\{\phi_i(x)\}_{i=1}^n$,

$$\psi(x) = \sum_{i=1}^{n} c_i \phi_i(x)\,. \tag{A.1.2}$$

When the basis set is chosen appropriately Eq. (A.1.1) can be solved analytically and one can obtain an exact expression for the coefficients c_i. There are many types of basis sets which can be employed, one that has become popular is the so-called *sinc basis set* introduced by D. Colbert and W. H. Miller [125] in 1992.

A.2 The *sinc basis set*

The *sinc basis set* is a uniform Fourier grid basis. The advantage of this basis is that it allows for an analytical expression of the kinetic energy operator. It is extremely localized in each point of the grid as it consists of a set of delta functions. The sinc function in one dimension is defined as

$$Sinc\left[\xi\right] = \frac{sin\left[\xi\right]}{\xi}. \tag{A.2.1}$$

Consider a set of n points uniformly distributed in the range $[x_{min},\ x_{max}]$, each point of the grid x_j is defined as

$$x_j = x_{min} + \Delta x\left(j-1\right), \tag{A.2.2}$$

where

$$\Delta x = \frac{x_{max} - x_{min}}{n-1}. \tag{A.2.3}$$

Given this notation, the j-th basis function $\phi_j\left(x\right)$ corresponds to the grid spacing normalized $Sinc$ function

$$\phi_j\left(x\right) = \frac{1}{\sqrt{\Delta x}} \frac{sin\left[\pi\left(x-x_j\right)/\Delta x\right]}{\pi\left(x-x_j\right)/\Delta x} = \frac{1}{\sqrt{\Delta x}} Sinc\left[\pi\left(x-x_j\right)/\Delta x\right]. \tag{A.2.4}$$

The basis in Eq. (A.2.4) can be defined using a Fourier representation (Eq. A.2.5), in fact one has

$$\begin{aligned} \phi_j\left(x\right) &= \frac{\sqrt{\Delta x}}{2\pi} \int_{-\pi/\Delta x}^{+\pi/\Delta x} e^{ik(x-x_j)} dk \\ &= \frac{\sqrt{\Delta x}}{2\pi i\left(x-x_j\right)} \left[e^{i\pi(x-x_j)/\Delta x} - e^{-i\pi(x-x_j)/\Delta x}\right] \\ &= \frac{1}{\sqrt{\Delta x}} \frac{sin\left[\pi\left(x-x_j\right)/\Delta x\right]}{\pi\left(x-x_j\right)/\Delta x}. \end{aligned} \tag{A.2.5}$$

Analogously, it is possible to define them as the Fourier transform of the eigenfunctions of the time independent free particle Hamiltonian

$$\phi_j\left(x\right) = \frac{\sqrt{\Delta x}}{2\pi\hbar} \int_{-\pi/\Delta x}^{+\pi/\Delta x} e^{ip(x-x_j)/\hbar} dp. \tag{A.2.6}$$

Now, the value of the j-th basis function in the grid point x_k will be

$$\phi_j(x_k) = \frac{1}{\sqrt{\Delta x}} \frac{sin\left[\pi(k-j)\right]}{\pi(k-j)} = \frac{\delta_{kj}}{\sqrt{\Delta x}} \tag{A.2.7}$$

and so, we see that the basis is properly localized: i.e it is equal to $1/\sqrt{\Delta x}$ where it is centered and zero everywhere else. Note that this basis is also orthonormal, in fact

$$\begin{aligned}
&\int_{-\infty}^{+\infty} \phi_i^\star(x)\,\phi_j(x)\,dx = \\
&= \frac{\Delta x}{(2\pi)^2} \int_{-\infty}^{+\infty} \int_{-\pi/\Delta x}^{+\pi/\Delta x} e^{+ik(x-x_j)} dk \int_{-\pi/\Delta x}^{+\pi/\Delta x} e^{-ik'(x-x_i)} dk' dx \\
&= \frac{\Delta x}{(2\pi)^2} \int_{-\pi/\Delta x}^{+\pi/\Delta x} dk \int_{-\pi/\Delta x}^{+\pi/\Delta x} dk' e^{-ikx_j + ik'x_i} \int_{-\infty}^{+\infty} e^{ix\left(k-k'\right)} dx \\
&= \frac{\Delta x}{(2\pi)^2} \int_{-\pi/\Delta x}^{+\pi/\Delta x} dk \int_{-\pi/\Delta x}^{+\pi/\Delta x} dk' e^{-ikx_j + ik'x_i} 2\pi\delta(k-k') \\
&= \frac{\Delta x}{2\pi} \int_{-\pi/\Delta x}^{+\pi/\Delta x} e^{ik(x_i - x_j)} dk \\
&= \frac{sin\left[\pi(x_i - x_j)/\Delta x\right]}{\pi(x_i - x_j)/\Delta x} = \delta_{ij}.
\end{aligned} \tag{A.2.8}$$

A.2.1 Evaluation of moments

In order to express operators in this basis we need to find an expression for the moments. The n-th moment is defined as

$$\begin{aligned}
&\int_{-\infty}^{+\infty} \phi_i^\star(x) \frac{d^n}{dx^n} \phi_j(x)\,dx = \\
&= \frac{\Delta x}{(2\pi)^2} \int_{-\infty}^{+\infty} dx \int_{-\pi/\Delta x}^{+\pi/\Delta x} e^{-ik(x-x_i)} dk \int_{-\pi/\Delta x}^{+\pi/\Delta x} \left[\frac{d^n}{dx^n} e^{ik'(x-x_j)}\right] dk' \\
&= \frac{\Delta x}{(2\pi)^2} \int_{-\pi/\Delta x}^{+\pi/\Delta x} dk \int_{-\pi/\Delta x}^{+\pi/\Delta x} dk' e^{ikx_i - ik'x_j} (ik')^n \int_{-\infty}^{+\infty} e^{-ix\left(k-k'\right)} dx \\
&= \frac{\Delta x}{(2\pi)} \int_{-\pi/\Delta x}^{+\pi/\Delta x} dk\,(ik)^n e^{ik(x_i - x_j)} \\
&= \frac{\Delta x}{(2\pi)} \int_{-\pi/\Delta x}^{+\pi/\Delta x} dk \left[\frac{d^n}{dx_i^n} e^{ik(x_i - x_j)}\right] \\
&= \frac{d^n}{dx_i^n} \frac{sin\left[\pi(x_i - x_j)/\Delta x\right]}{\pi(x_i - x_j)/\Delta x}.
\end{aligned} \tag{A.2.9}$$

For $n = 1$, we find the first moment

$$\frac{d}{dx_i}\frac{sin\left[\pi\left(x_i - x_j\right)/\Delta x\right]}{\pi\left(x_i - x_j\right)/\Delta x} = \frac{cos\left[\pi\left(x_i - x_j\right)/\Delta x\right]}{\left(x_i - x_j\right)} - \frac{sin\left[\pi\left(x_i - x_j\right)/\Delta x\right]}{\pi\left(x_i - x_j\right)^2/\Delta x}. \tag{A.2.10}$$

If $i \neq j$, the sine terms are zero and we obtain the non diagonal elements

$$\int_{-\infty}^{+\infty} \phi_i^\star\left(x\right)\frac{d}{dx}\phi_j\left(x\right)dx = \frac{\left(-1\right)^{i-j}}{\Delta x\left(i-j\right)} \qquad (i \neq j). \tag{A.2.11}$$

For $n = 2$, we find the second moment

$$\begin{aligned}\frac{d^2}{dx_i^2}\frac{sin\left[\frac{\pi\left(x_i-x_j\right)}{\Delta x}\right]}{\frac{\pi\left(x_i-x_j\right)}{\Delta x}} &= -\frac{\pi}{\Delta x}\frac{sin\left[\frac{\pi\left(x_i-x_j\right)}{\Delta x}\right]}{\left(x_i-x_j\right)} - 2\frac{cos\left[\frac{\pi\left(x_i-x_j\right)}{\Delta x}\right]}{\left(x_i-x_j\right)^2} + \\ &+2\frac{sin\left[\frac{\pi\left(x_i-x_j\right)}{\Delta x}\right]}{\frac{\pi\left(x_i-x_j\right)^3}{\Delta x}}.\end{aligned} \tag{A.2.12}$$

Again when $i \neq j$, the sine terms cancel and we obtain

$$\int_{-\infty}^{+\infty} \phi_i^\star\left(x\right)\frac{d^2}{dx^2}\phi_j\left(x\right)dx = -2\frac{\left(-1\right)^{i-j}}{\Delta x^2\left(i-j\right)^2} \qquad (i \neq j). \tag{A.2.13}$$

The diagonal elements correspond to the derivatives in the limit of $x_i \to x_j$. Therefore, we can expand the sinc function $Sinc\left[\pi\left(x_i - x_j\right)/\Delta x\right]$ respect to x_i around x_j

$$\begin{aligned}Sinc\left[\frac{\pi\left(x_i-x_j\right)}{\Delta x}\right] &= \frac{\Delta x}{\pi\left(x_i-x_j\right)}\left(\frac{\pi\left(x_i-x_j\right)}{\Delta x} - \frac{1}{3!}\frac{\pi^3\left(x_i-x_j\right)^3}{\Delta x^3}\right) + \mathcal{O}\left(\left(\frac{x_i-x_j}{\Delta x}\right)^4\right) \\ &= 1 - \frac{1}{6}\frac{\pi^2\left(x_i-x_j\right)^2}{\Delta x^2} + \mathcal{O}\left(\left(\frac{x_i-x_j}{\Delta x}\right)^4\right).\end{aligned} \tag{A.2.14}$$

Finally, we obtain the diagonal terms for the first moment

$$\int_{-\infty}^{+\infty} \phi_i^\star\left(x\right)\frac{d}{dx}\phi_i\left(x\right)dx = -\frac{1}{3}\frac{\pi^2\left(x_i-x_j\right)}{\Delta x^2} = -\frac{1}{3}\frac{\pi^2\left(i-j\right)}{\Delta x} \qquad (i = j), \tag{A.2.15}$$

and for the second moment

$$\int_{-\infty}^{+\infty} \phi_i^\star\left(x\right)\frac{d^2}{dx^2}\phi_i\left(x\right)dx = -\frac{1}{3}\frac{\pi^2}{\Delta x^2} \qquad (i = j), \tag{A.2.16}$$

A.2.2 The Hamiltonian and other operators in the one dimensional sync basis

To represent the Hamiltonian operator we need a representation of the potential operator. Note that the position operator $\hat{x}$ is expressed as

$$\begin{aligned}
&\langle x_i|\,\hat{x}\,|x_j\rangle = \int_{-\infty}^{+\infty} dx\,\langle x_i|x|x\rangle\,\langle x|x_j| = \rangle \\
&= \frac{\Delta x}{(2\pi)^2}\int_{-\pi/\Delta x}^{+\pi/\Delta x} dk \int_{-\pi/\Delta x}^{+\pi/\Delta x} dk' e^{ikx_i - ik'x_j}\frac{d}{dik'}\int_{-\infty}^{+\infty} dx e^{ix\left(k'-k\right)} \\
&= \frac{\Delta x}{(2\pi)}\int_{-\pi/\Delta x}^{+\pi/\Delta x} dk \int_{-\pi/\Delta x}^{+\pi/\Delta x} dk' e^{ikx_i - ik'x_j}\frac{d}{dik'}\delta\left(k'-k\right) \\
&= \frac{\Delta x}{(2\pi i)}\int_{-\pi/\Delta x}^{+\pi/\Delta x} dk' e^{-ik'x_j}\frac{d}{dk'}\int_{-\pi/\Delta x}^{+\pi/\Delta x} dk e^{ikx_i}\delta\left(k'-k\right) \\
&= \frac{\Delta x}{2\pi}x_i\int_{-\pi/\Delta x}^{+\pi/\Delta x} dk' e^{ik'(x_i-x_j)} \\
&= x_i Sinc\left[\pi\left(x_i-x_j\right)/\Delta x\right] = x_i\delta_{ij}.
\end{aligned} \tag{A.2.17}$$

The potential $V\left(x\right)$ can always be expanded in a power series of x therefore it can be expressed as a diagonal matrix of the type

$$\int_{-\infty}^{+\infty}\phi_i^{\star}\left(x\right)V\left(x\right)\phi_j\left(x\right)dx = V\left(x_i\right)\delta_{ij}. \tag{A.2.18}$$

The typical Hamiltonian is expressed as the sum of a kinetic energy operator $\hat{T} = -\frac{\hbar^2}{2m}\nabla^2$ and a potential energy operator $\hat{V} = V\left(x\right)$, that is $\hat{\mathcal{H}} = \hat{T} + \hat{V}$. Using the DVR representation, the kinetic energy operator assumes the form

$$T_{ij} = \frac{\hbar^2\left(-1\right)^{i-j}}{2m\Delta x^2}\cdot\begin{cases}\frac{\pi^2}{3} & i = j\\ \frac{2}{(i-j)^2} & i \neq j\end{cases}. \tag{A.2.19}$$

To solve the k-th eigenvalue problem

$$\hat{\mathcal{H}}\psi_k = E_k\psi_k, \tag{A.2.20}$$

the procedure will consist in diagonalizing H_{ij} to obtain the eigenvalues $(E_1, ..., E_k, ...E_n)$ and eigenvector coefficients C_{ij}. Then one can obtain the k-th eigenfunction as

$$\psi_k\left(x\right) = \sum_{j=1}^{n} C_{jk}\phi_j\left(x\right). \tag{A.2.21}$$

Since the basis set is localized, the value of the k-th basis function in a specific grid location x_i will be given by

$$\langle x_i|\psi_k\rangle = \psi_k(x_i) = \sum_j C_{jk}\phi_j(x_i) = \sum_j C_{jk}\frac{\delta_{ji}}{\sqrt{\Delta x}} = \frac{C_{ik}}{\sqrt{\Delta x}}. \tag{A.2.22}$$

Generally speaking, higher energy eigenvalues will not be very accurate because they correspond to eigenfunctions which feel the edges of the grid more than lower energy states. This is typically not a problem because the states which contribute most to the dynamics are at low energies and higher energy states are not very populated.

APPENDIX B

The WKB Approximation for the Double Barrier

The WKB wave functions before, between and after the barriers reported in Fig. (B.1) are respectively

$$\psi_I(x) = \frac{A}{\sqrt{k(x)}} e^{i\left(\frac{\pi}{4}+\int_{x_1}^{x} k(x')dx'\right)} + \frac{B}{\sqrt{k(x)}} e^{-i\left(\frac{\pi}{4}+\int_{x_1}^{x} k(x')dx'\right)} \tag{B.1a}$$

$$\psi_{III}(x) = \frac{C}{\sqrt{k(x)}} e^{i\left(\frac{\pi}{4}+\int_{x_2}^{x} k(x')dx'\right)} + \frac{D}{\sqrt{k(x)}} e^{-i\left(\frac{\pi}{4}+\int_{x_2}^{x} k(x')dx'\right)} \tag{B.1b}$$

$$\psi_V(x) = \frac{E}{\sqrt{k(x)}} e^{i\left(\frac{\pi}{4}+\int_{x_4}^{x} k(x')dx'\right)} + \frac{F}{\sqrt{k(x)}} e^{-i\left(\frac{\pi}{4}+\int_{x_4}^{x} k(x')dx'\right)}, \tag{B.1c}$$

where $k(x)$ is the one dimensional wave vector, x_i the $i-th$ turning point, and the coefficients are reported in Fig. (B.1).

After applying the barrier connection formula twice [126], the coefficients E and F in terms of A and B are

$$\begin{pmatrix} E \\ F \end{pmatrix} = \begin{pmatrix} \sqrt{1+e^{2\theta_2}}, & -e^{\theta_2} \\ -e^{\theta_2} & \sqrt{1+e^{2\theta_2}} \end{pmatrix} \begin{pmatrix} \left(\sqrt{1+e^{2\theta_1}}A - Be^{\theta_1}\right) e^{i\phi} \\ \left(\sqrt{1+e^{2\theta_1}}B - Ae^{\theta_1}\right) e^{-i\phi} \end{pmatrix}, \tag{B.2}$$

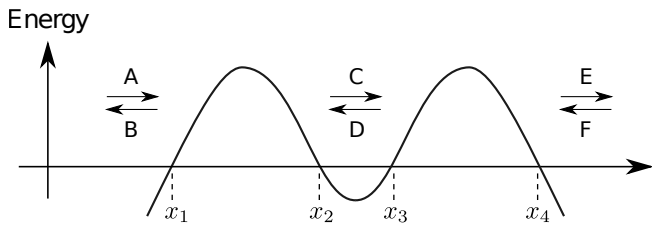

Figure B.1: Double barrier potential and turning points: A, B, C, D, E, and F are the WKB wave-function coefficients in the three allowed regions.

where

$$\theta_1 = \int_{x_1}^{x_2} |k(x)|\, dx \tag{B.3a}$$

$$\theta_2 = \int_{x_3}^{x_4} |k(x)|\, dx \tag{B.3b}$$

$$\phi = \int_{x_2}^{x_3} k(x)\, dx. \tag{B.3c}$$

In order to calculate the transmission probability of an incoming wave from the left, the coefficient F is set to zero and B is consequently expressed in terms of A. Then, the ratio is

$$\frac{E}{A} = \frac{1}{e^{\theta_1} e^{\theta_2} e^{i\phi} + \sqrt{1+e^{2\theta_1}}\sqrt{1+e^{2\theta_2}} e^{-i\phi}} \tag{B.4}$$

and the transmission probability is the modulus square of Eq. (B.4) [127]

$$T(E) = \frac{p_1 p_2}{1 + (1-p_1)(1-p_2) + 2\sqrt{1-p_1}\sqrt{1-p_2}\cos(2\phi)}, \tag{B.5}$$

where

$$p_i = \frac{1}{1+e^{\theta_i}}, \qquad i = 1, 2. \tag{B.6}$$

Taking a symmetric double barrier ($p_1 = p_2 = p$) and expanding $\phi(E) \approx \phi(E_i) + \phi'(E_i)(E - E_i)$ at the $i-th$ resonant energy, Eq. (B.5) is approximated as

$$T(E) \approx \frac{(\Gamma_i/2)^2}{(E-E_i)^2 + (\Gamma_i/2)^2}, \tag{B.7}$$

where the Breit-Wigner distribution width is

$$\Gamma_i = \frac{e^{-2\theta_i}}{\phi'(E_i)\sqrt{1-e^{-2\theta_i}}} \approx \frac{e^{-2\theta_i}}{\phi'(E_i)}. \tag{B.8}$$

List of Publications

As of March 5th, 2013. (*) refers to publications related to this thesis.

- **Publications in Peer-Reviewed Journals**
  - (*) S. Mandrà, S. Valleau and M. Ceotto, "*Deep nuclear resonant tunneling thermal rate constant calculation*", to be published on International Journal of Quantum Chemistry (2012).
  - S. Mandrà, S. Fortunato and C. Castellano, "*Coevolution of Glauber-like Ising dynamics and topology*", Physical Review E 80 (5), 056105 (2009).
  - F. Bassetti, M. Cosentino Lagomarsino and S. Mandrà, "*Exchangeable random networks*", Internet Mathematics 4 (4), 357-400 (2007)
- **Publications in preparation**
  - (*) S. Mandrà and M. Ceotto, "*Inverse Kinetic Isotope Effect Induced by Resonant Tunneling*" (2012).
  - (*) S. Mandrà, A. M. Brockway, M. Ceotto and J. Schrier, "*Helium Isotope Separation via Resonant Tunneling through an Organometallic Nanoporous Graphene Bilayer*" (2012).
  - M. Gherardi, S. Mandrà, B. Bassetti, M. Cosentino Lagomarsino, "Hard and soft bounds in the evolution of Ubuntu packages. A lesson for species body masses?", ArXiv:1303.0011 (2013).
- **Publication in conference proceedings**
  - S. Mandrà, M. Cosentino Lagomarsino and B. Bassetti, "*Typical rank of coin-toss power-law random matrices over GF (2)*", to be published on Lecture Notes on Computer Science, ArXiv:1011.1563 (2011).

Bibliography

[1] H. Eyring. *Chem. Rev.*, 17(1), 1935.

[2] H. Eyring. *J. Chem. Phys.*, 3, 1935.

[3] M. G. Evans and M. Polanyi. *Trans. of the Faraday Soc.*, 31, 1935.

[4] E. Wigner. *Trans. of the Faraday Soc.*, 34, 1938.

[5] L. Chang, L. Esaki, and R. Tsu. *Appl. Phys. Lett.*, 24(12), 1974.

[6] M. Hirose, M. Morita, and Y. Osaka. *Jap. J. of Appl. Phys. Suppl.*, 16, 1977.

[7] G. Bastard, J. Brum, and R. Ferreira. *Solid State Phys.*, 44, 1991.

[8] R. Ferreira and G. Bastard. *Rep. on Progr. in Phys.*, 60(3), 1999.

[9] R. Schuster, E. Buks, M. Heiblum, D. Mahalu, V. Umansky, and H. Shtrikman. *Nature*, 385(6615), 1997.

[10] A. Yariv. *Edition Holt, Rinehart and Winston*, 1991.

[11] J. D. Gezelter and W. H. Miller. *J. Chem. Phys.*, 103(18), 1995.

[12] T. C. Germann and W. H. Miller. *J. Phys. Chem. A*, 101(36), 1997.

[13] T. C. Germann and W. H. Miller. *J. Chem. Phys.*, 109(1), 1998.

[14] A. Viel, C. Leforestier, and W. H. Miller. *J. Chem. Phys.*, 108, 1998.

[15] J. Dai and J. Z. Zhang. *J. Phys. Chem.*, 100(17), 1996.

[16] S. Y. Lin, Z. Sun, H. Guo, D. H. Zhang, P. Honvault, D. Xie, and S.-Y. Lee. *J. Phys. Chem. A*, 112(4), 2008.

[17] H. S. Johnston. Ronald Press Company New York, 1966.

[18] E. Kane. *Tunn. Phen. in Solids*, 1969.

[19] Y. Zohta. *Phys. Rev. B*, 41, 1990.

[20] R. Tsu and L. Esaki. *Appl. Phys. Lett.*, 22(11), 1973.

[21] A. Dutt and S. Kar. *American J. of Phys.*, 78, 2010.

[22] V. Engel, R. Schinke, and E. Pollak. *J. Chem. Phys.*, 87, 1987.

[23] U. Peskin, N. Moiseyev, and R. Lefebvre. *J. Chem. Phys.*, 92, 1990.

[24] E. Narevicius and N. Moiseyev. *J. Chem. Phys.*, 113, 2000.

[25] H. Barkay and N. Moiseyev. *Phys. Rev. A*, 64(4), 2001.

[26] H. Barkay, E. Narevicius, and N. Moiseyev. *Phys. Rev. B*, 67(4), 2003.

[27] T. Goldzak, I. Gilary, and N. Moiseyev. *Phys. Rev. A*, 82(5), 2010.

[28] W. H. Miller, S. D. Schwartz, and J. W. Tromp. *J. Chem. Phys.*, 79, 1983.

[29] W. H. Miller. *J. Phys. Chem. A*, 102(5), 1998.

[30] V. Ryaboy and R. Lefebvre. *J. Chem. Phys.*, 99, 1993.

[31] L. Berman and U. Peskin. *Chem. Phys. Lett.*, 360(3), 2002.

[32] M. Caspary, L. Berman, and U. Peskin. *Chem. Phys. Lett.*, 369(1), 2003.

[33] L. Berman and U. Peskin. *Int. J. of Quant. Chem.*, 99(5), 2004.

[34] M. Caspary Toroker and U. Peskin. *Chem. Phys.*, 370(1), 2010.

[35] S. Mandrà, S. Valleau, and M. Ceotto. *Int. J. of Quant. Chem.*, doi:10.1002/qua.24395.

[36] S. Mandrà, A. M. Brockway, M. Ceotto, and J. Schrier. "Helium Isotope Separation via Resonant Tunneling through an Organometallic Nanoporous Graphene Bilayer.", *in preparation*.

[37] S. Mandrà and M. Ceotto. "Inverse Kinetic Isotope Effect Induced by Resonant Tunneling.", *in preparation*.

[38] P. Saalfrank and W. H. Miller. *Surface science*, 303(1), 1994.

[39] T. Yamamoto, H. Wang, and W. H. Miller. *J. Chem. Phys.*, 116(17), 2002.

[40] M. Thoss, H. Wang, and W. H. Miller. *J. Chem. Phys.*, 115, 2001.

[41] H. Wang, M. Thoss, K. L. Sorge, R. Gelabert, X. Giménez, and W. H. Miller. *J. Chem. Phys.*, 114, 2001.

[42] H. Wang, M. Thoss, and W. H. Miller. *J. Chem. Phys.*, 112, 2000.

[43] T. Seideman and W. H. Miller. *J. Chem. Phys.*, 96(6), 1992.

[44] T. Seideman and W. H. Miller. *J. Chem. Phys.*, 97, 1992.

[45] U. Manthe and W. H. Miller. *J. Chem. Phys.*, 99, 1993.

[46] Y. Guo, D. L. Thompson, and W. H. Miller. *J. Phys. Chem. A*, 103(49), 1999.

[47] W. H. Miller, Y. Zhao, M. Ceotto, and S. Yang. *J. Chem. Phys.*, 119, 2003.

[48] M. Ceotto and W. H. Miller. *J. Chem. Phys.*, 120, 2004.

[49] D. J. Tannor and S. Garashchuk. *Ann. Rev. of Phys. Chem.*, 51(1), 2000.

[50] S. Garashchuk and T. Vazhappilly. *J. Chem. Phys.*, 131(16), 2009.

[51] R. van Harrevelt, G. Nyman, and U. Manthe. *J. Chem. Phys.*, 126, 2007.

[52] T. Wu, H.-J. Werner, and U. Manthe. *Science*, 306(5705), 2004.

[53] R. Landauer. *IBM J. of Research and Develop.*, 1(3), 1957.

[54] S. Datta. Cambridge University Press, 2005.

[55] S. Datta, volume 40. Cambridge University Press, 1997.

[56] R. Kim, S. Datta, and M. S. Lundstrom. *J. of Appl. Phys.*, 105(3), 2009.

[57] E. Pollak and W. H. Miller. *Phys. Rev. Lett.*, 53(2), 1984.

[58] B. Poirier. *Chem. Phys.*, 370(1), 2010.

[59] J. Schiff and B. Poirier. *J. Chem. Phys.*, 136(3), 2012.

[60] D. C. S. Althorpe. *Ann. Rew. of Phys. Chem.*, 54(1), 2003.

[61] B. R. Johnson. *J. Chem. Phys.*, 67, 1977.

[62] D. L. Yeager and W. H. Miller. *J. Phys. Chem.*, 95(21), 1991.

[63] B. Noumerov. *Monthly Notices of the Royal Astronomical Society*, 84, 1924.

[64] J. Butcher. Wiley-Interscience, 1987.

[65] D. T. Colbert and W. H. Miller. *J. Chem. Phys.*, 96, 1992.

[66] H. Jeffreys. In *Proc. Cambridge Phil. Soc*, volume 49, pages 601–611. Cambridge Univ Press, 1953.

[67] G. Wentzel. *Zeits. für Phys. A*, 38(6), 1926.

[68] H. A. Kramers. *Zeits. für Phys. A*, 39(10), 1926.

[69] L. Brillouin. *Zeits. der Phys.*, 39, 1926.

[70] L. Wittenberg, E. N. Cameron, G. L. Kulcinski, S. H. Ott, J. F. Santarius, G. I. Sviatoslavsky, I. N. Sviatoslavsky, and H. Thompson. *Fusion Technol.*, 21, 1991.

[71] Technical Report GAO-11-472, U. S. Government Accountability Office, Washington, D.C., May 2011.

[72] D. A. Shea and D. Morgan. Technical Report R41419, Congressional Research Service, Washington, D.C., December 2010.

[73] P. Bernardo, E. Drioli, and G. Golemme. *Ind. Eng. Chem. Res.*, 48, 2009.

[74] J. Schrier. *J. Phys. Chem. Lett.*, 1, 2010.

[75] S. Blankenburg, M. Bieri, R. Fasel, K. Müllen, C. A. Pignedoli, and D. Passerone. *Small*, 6, 2010.

[76] M. Bieri, M. Trier, J. Cai, K. Aït-Mansour, P. Ruffieux, O. Gröning, P. Gröning, M. Kastler, R. Rieger, X. Feng, K. Müllen, and R. Fasel. *Chem. Commun.*, 2009.

[77] Y. Li, Z. Zhou, P. Shen, and Z. Chen. *Chem. Commun.*, 46, 2010.

[78] J. Schrier and J. McClain. *Chem. Phys. Lett.*, 521, 2012.

[79] A. W. Hauser and P. Schwerdtfeger. *J. Phys. Chem. Lett.*, 3, 2012.

[80] J. M. Pereira, P. Vasilopoulos, and F. M. Peeters. *Appl. Phys. Lett.*, 90, 2007.

[81] M. O. Sinnokrot, E. F. Valeev, and C. D. Sherrill. 124, 2002.

[82] A. Du, Z. Zhu, and S. C. Smith. 132, 2010.

[83] P. Reunchan and S.-H. Jhi. *Appl. Phys. Lett.*, 98, 2011.

[84] J. M. Vollmer, A. K. Kandalam, and L. A. Curtiss. *J. Phys. Chem. A*, 106, 2002.

[85] T. Yasuike, A. Nakajima, S. Yabushita, and K. Kaya. *J. Phys. Chem. A*, 101, 1997.

[86] H. Liu, Q. Li, Y. Xie, R. B. King, and H. F. Schaefer. *J. Phys. Chem. A*, 114, 2010.

[87] J. J. P. Stewart. *J. Mol. Model.*, 13, 2007.

[88] M. Korth, M. Pitonák, J. Rezác, and P. Hobza. 6, 2010.

[89] J. J. P. Stewart. MOPAC2009, Version 11.053L. http://OpenMOPAC.net.

[90] T. A. Baker and M. Head-Gordon. *J. Phys. Chem. A*, 114, 2010.

[91] X. Gonze, B. Amadon, P.-M. Anglade, J.-M. Beuken, F. Bottin, P. Boulanger, F. Bruneval, D. Caliste, R. Caracas, M. Cote, T. Deutsch, L. Genovese, P. Ghosez, M. Giantomassi, S. Goedecker, D. Hamann, P. Hermet, F. Jollet, G. Jomard, S. Leroux, M. Mancini, S. Mazevet, M. Oliveira, G. Onida, Y. Pouillon, T. Rangel, G.-M. Rignanese, D. Sangalli, R. Shaltaf, M. Torrent, M. Verstraete, G. Zerah, and J. Zwanziger. *Computer Phys. Comm.*, 180, 2009.

[92] http://toc.uni-muenster.de/DFTD3/.

[93] S. Grimme. *J. Comput. Chem.*, 27, 2006.

[94] S. Grimme, J. Antony, S. Ehrlich, and H. Krieg. *J. Chem. Phys.*, 132, 2010.

[95] S. Grimme, S. Ehrlich, and L. Goerigk. *J. Comput. Chem.*, 32, 2011.

[96] R. P. Feynman. *Int. J. of Th. Phys.*, 21(6), 1982.

[97] S. Lloyd. *Science*, 273(5278), 1996.

[98] D. S. Abrams and S. Lloyd. *Phys. Rev. Lett.*, 79(13), 1997.

[99] G. Ortiz, J. Gubernatis, E. Knill, and R. Laflamme. *Phys. Rev. A*, 64(2), 2001.

[100] A. Aspuru-Guzik, A. D. Dutoi, P. J. Love, and M. Head-Gordon. *Science*, 309(5741), 2005.

[101] I. Kassal, S. P. Jordan, P. J. Love, M. Mohseni, and A. Aspuru-Guzik. *Proc. Natl. Acad. Sci. USA.*, 105(48), 2008.

[102] I. Kassal, J. Whitfield, A. Perdomo-Ortiz, M. Yung, and A. Aspuru-Guzik. *Ann. Rev. of Phys. Chem.*, 62, 2011.

[103] A. Perdomo-Ortiz, N. Dickson, M. Drew-Brook, G. Rose, and A. Aspuru-Guzik. *Sc. Rep.*, 2, 2012.

[104] S. P. Jordan, K. S. Lee, and J. Preskill. *Science*, 336(6085), 2012.

[105] I. Buluta and F. Nori. *Science*, 326(5949), 2009.

[106] B. P. Lanyon, J. D. Whitfield, G. Gillett, M. E. Goggin, M. P. Almeida, I. Kassal, J. D. Biamonte, M. Mohseni, B. J. Powell, M. Barbieri, et al. *Nature Chem.*, 2(2), 2010.

[107] A. Aspuru-Guzik and P. Walther. *Nature Phys.*, 8(4), 2012.

[108] J. Pan, Y. Cao, X. Yao, Z. Li, C. Ju, X. Peng, S. Kais, and J. Du. *arXiv:1302.1946*, 2013.

[109] D. Deutsch and D. Deutsch. *Proc. of the Royal Soc. of London A*, 425(1868), 1989.

[110] A. Barenco, D. Deutsch, A. Ekert, and R. Jozsa. *Phys. Rev. Lett.*, 74(20), 1995.

[111] T. Sleator and H. Weinfurter. *Phys. Rev. Lett.*, 74(20), 1995.

[112] S. Lloyd. *Phys. Rev. Lett.*, 75(2), 1995.

[113] D. Deutsch. *Proc. of the Royal Soc. of London A*, 400(1818), 1985.

[114] A. M. Childs. PhD thesis, Massachusetts Institute of Technology, 2004.

[115] M. A. Nielsen and I. L. Chuang. Cambridge university press, 2010.

[116] D. A. Lidar and H. Wang. 59(2), 1999.

[117] D. Tannor, chapter 11, pages 281–307. University Science Books, 2007.

[118] C. Zalka. *Proc. of the Royal Soc. of London A*, 454(1969), 1998.

[119] A. T. Sornborger. *Sc. Rep.*, 2, 2012.

[120] D. S. Abrams and S. Lloyd. *Phys. Rev. Lett.*, 83(24), 1999.

[121] P. Jaksch and A. Papageorgiou. *Phys. Rev. Lett.*, 91(25), 2003.

[122] A. W. Harrow, A. Hassidim, and S. Lloyd. *Phys. Rev. Lett.*, 103(15), 2009.

[123] D. W. Berry, G. Ahokas, R. Cleve, and B. C. Sanders. *Comm. in Math. Phys.*, 270(2), 2007.

[124] J. C. Light, I. P. Hamilton, and J. V. Light. *J. Chem. Phys.*, 82, 1985.

[125] D. T. Colbert and W. H. Miller. *J. Chem. Phys.*, 96, 1992.

[126] W. H. Miller. *J. Chem. Phys.*, 48, 1968.

[127] W. Miller. *Private Communication*.